



**HAL**  
open science

# Wetting of yield-stress fluids : capillary bridges and drop spreading

Loren Jørgensen

► **To cite this version:**

Loren Jørgensen. Wetting of yield-stress fluids : capillary bridges and drop spreading. Materials Science [cond-mat.mtrl-sci]. Université de Lyon, 2016. English. NNT : 2016LYSE1163 . tel-01424224

**HAL Id: tel-01424224**

**<https://theses.hal.science/tel-01424224>**

Submitted on 2 Jan 2017

**HAL** is a multi-disciplinary open access archive for the deposit and dissemination of scientific research documents, whether they are published or not. The documents may come from teaching and research institutions in France or abroad, or from public or private research centers.

L'archive ouverte pluridisciplinaire **HAL**, est destinée au dépôt et à la diffusion de documents scientifiques de niveau recherche, publiés ou non, émanant des établissements d'enseignement et de recherche français ou étrangers, des laboratoires publics ou privés.



N° d'ordre NNT : 2016LYSE1163

## THÈSE DE DOCTORAT DE L'UNIVERSITÉ DE LYON

opérée au sein de

**l'Université Claude Bernard Lyon 1**

**École Doctorale ED52**

**Physique et Astrophysique de Lyon**

**Spécialité de doctorat : Physique**

Soutenue publiquement le 15/09/2016, par :

**Loren Jørgensen**

---

# Wetting of yield-stress fluids: capillary bridges and drop spreading

---

Directrice de thèse : **Catherine Barentin**

Devant le jury composé de :

**Élisabeth Charlaix**, Professeur, Université Grenoble-Alpes

Présidente

**Élise Lorenceau**, Directrice de Recherche, Laboratoire Navier (UMR8205)

Rapporteuse

**Guillaume Ovarlez**, Directeur de Recherche, LOF (UMR5258)

Rapporteur

**Christophe Clanet**, Directeur de Recherche, LadHyX (UMR7646)

Examineur

**Laurence Talini**, Maître de Conférences, Université Pierre et Marie Curie  
Paris 6

Examinatrice

**Catherine Barentin**, Professeur, Université Claude Bernard Lyon 1

Directrice de thèse

**Hélène Delanoë-Ayari**, Maître de Conférences, Université Claude Bernard  
Lyon 1

Invitée





*Équipe Liquides aux Interfaces*

*Institut Lumière Matière – UMR5306 CNRS*

*Université Claude Bernard Lyon 1*

*Campus LyonTech La Doua*

*10 rue Ada Byron*

*69622 Villeurbanne Cedex*

## **Wetting of yield-stress fluids: capillary bridges and drop spreading**

Wetting phenomena and yield-stress fluids rheology are subfields of soft matter physics where big understanding steps have been made during the last centuries. In addition, these two fields have very important potential implications for industry, which contributes to their dynamism. But their combination, the wetting of yield-stress fluids, has received little interest until the very last years, although it is a situation that happens frequently. Indeed, yield-stress fluids gather nearly all the fluids encountered in food industry, cosmetics, building industry, oil and gas industry... and wetting properties are crucial, as many processes involve interfaces with air or a solid surface. The difficulty lies in the intrinsic out-of-equilibrium character of yield-stress fluids, while capillarity laws are valid for equilibrium states.

This work revisits seminal experiments with a model yield-stress fluid called carbopol. The first experiment consists in measuring the adhesion force of a capillary bridge and comparing it to the case of simple fluids. The main results show how the apparent surface tension is affected by yield stress. They also highlight the importance of the deformation history and of the fluid elasticity. The second main experiment concerns spreading of drops on a solid surface, classically described by Tanner's law. I study the short-time and long-time dynamics, as well as the final contact angle. The first regime is influenced by viscoelasticity, whereas the final state is determined by the yield stress and not only by Young-Dupré's theory.

**Keywords:** Wetting, Yield-stress fluids, Carbopol, Surface tension, Spreading, Rheology

## **Mouillage de fluides à seuil : ponts capillaires et étalement de gouttes**

Les phénomènes de mouillage et la rhéologie des fluides à seuil sont deux domaines de la physique des matériaux mous dans lesquels de grandes avancées ont été faites lors des derniers siècles. De plus ces questions sont d'une grande importance au niveau des applications industrielles, ce qui contribue à leur dynamisme. En revanche, le mouillage des fluides à seuil a été peu étudié, alors que c'est une situation fréquente. En effet, presque tous les fluides rencontrés dans l'industrie et la vie quotidienne sont des fluides à seuil. D'autre part, la connaissance des propriétés de mouillage est cruciale car la plupart des processus font intervenir des interfaces. La difficulté réside dans le caractère fondamentalement hors-équilibre des fluides à seuil, alors que les lois de la capillarité sont valables à l'équilibre.

Ce travail propose de revisiter des expériences classiques sur un fluide à seuil modèle appelé carbopol. La première expérience a consisté à mesurer la force d'adhésion d'un pont capillaire, qui a été comparée au cas des fluides simples. Les résultats ont montré comment la tension de surface apparente est affectée par le seuil. Ils ont aussi souligné l'importance de l'histoire de la déformation et de l'élasticité du fluide. La seconde expérience a porté sur l'étalement de gouttes sur une surface solide, classiquement décrit par la loi de Tanner. J'ai étudié la dynamique d'étalement, ainsi que l'angle de contact final. Alors que la dynamique est influencée par la viscoélasticité, l'état final est déterminé par le seuil plus que par la loi d'Young-Dupré.

**Mots-clés :** Mouillage, Fluides à seuil, Carbopol, Tension de surface, Étalement, Rhéologie

# Remerciements

*Les lecteurs de ce court chapitre peuvent être classés en deux catégories. Il y a ceux qui se lancent courageusement dans la lecture extensive du manuscrit. Et il y a ceux qui ne liront que les premières pages. Je vais donc commencer par ce qui intéresse le plus grand nombre : les remerciements.*

*Plus sérieusement, ce manuscrit qui relate en apparence mon travail de trois ans, peut être vu en réalité comme le résultat de nombreuses interactions et collaborations. Il a en effet été souligné que j'avais fait le choix d'orienter le discours sur mon cheminement intellectuel lors de la thèse plutôt que sur une description détaillée des expériences et résultats. Or ce cheminement n'a pu se faire que grâce aux discussions, aux rencontres, à l'aide fournie, bref, à tous les autres. Ainsi, ces quelques pages rendent modestement hommage à ces « autres » indispensables.*

*En premier lieu, je tiens à exprimer ma reconnaissance à Catherine, ma directrice de thèse. Elle a su me transmettre son enthousiasme et sa curiosité pour la science des fluides complexes. Je me suis passionnée à ses côtés pour le mouillage du carbopol, mais je pense que j'aurais pu travailler sur bien d'autres sujets, guidée par une encadrante si agréable. Non seulement j'ai pu profiter de sa grande expérience, mais j'ai aussi énormément apprécié sa gentillesse, sa disponibilité, son écoute patiente, ses encouragements et son humour. Quand je dis que je serais bien restée travailler avec elle trois ans de plus, ce n'est pas seulement pour plaisanter.*

*J'adresse aussi de chaleureux remerciements à Marie et Hélène pour leur collaboration privilégiée, surtout lors du travail sur le tensiomètre, et pour leur présence sympathique et attentive.*

*Je remercie tous les membres du jury d'avoir accepté de participer à ma soutenance, en particulier la présidente du jury, Élisabeth Charlaix, et les rapporteurs, Élise Lorenceau et Guillaume Ovarlez. Merci également à tous ceux qui sont venus m'écouter, ainsi qu'à ceux qui ont aidé aux détails pratiques (en particulier pour le pot).*

*Un élément qui mérite d'être souligné est l'ambiance très agréable au laboratoire. Je remercie donc la direction du laboratoire (Marie-France Joubert puis Philippe Dugourd) de m'y avoir accueillie, de même que les responsables de l'équipe Liquides et Interfaces (Christophe Ybert et Cécile Cottin-Bizonne). Je pense aussi aux membres de l'équipe Liquides, en particulier à Christophe P., Stella, Agnès, Rémy, Mathieu, Anne-Laure, en plus de ceux que j'ai déjà cités, ainsi qu'à Charlotte, pour des conseils, de l'aide et/ou des prêts de matériel. Merci à Gilles pour sa participation à la conception des expériences. Merci au service administratif et au service informatique pour leur contribution au bon fonctionnement de notre travail. Enfin, merci à Oriane pour les déjeuners « reboost ».*

*Je n'oublie pas les doctorants et post-docs ! Je me suis sentie très heureuse parmi eux et je leur adresse à tous une pensée émue, en espérant les revoir souvent par la suite. Merci donc à Baud, Alex, Ronan, Quentin, Tess, Teresa, Cora, Pauline, Angélique, Marie-Émeline, Manu, Félix, Sébastien, Alexis, Catherine, Joseph, Florence, Menka, Simon, Antoine et Andrea. Je remercie mes stagiaires Quentin et Antoine et les étudiants de TP Jérémy et Aurélien pour leur contribution. J'espère que cette expérience de recherche leur a plu.*

*Je m'éloigne maintenant de l'ILM, car je souhaite aussi remercier les personnes extérieures qui ont mis à ma disposition des dispositifs expérimentaux de leur laboratoire : Laurence Talini à l'ESPCI et Éric Freyssingeas, Stéphane Santucci et Valérie Vidal à l'ENS de Lyon.*

*Les copains de l'ENS m'ont également apporté un soutien très apprécié. Mention spéciale à Sylvie pour le footing du jeudi !*

*Je remonte aussi le temps pour saluer tous les professeurs qui ont contribué au succès de ma reconversion, de luthière à physicienne.*

*Bien évidemment, le soutien inconditionnel de ma famille a été capital lors de ce parcours atypique. Enfin, je remercie David pour sa confiance, sa patience et ses conseils sages.*

# Résumé

## Mouillage de fluides à seuil : ponts capillaires et étalements de gouttes

Cette thèse porte sur le mouillage de fluides à seuil, mariage de deux thèmes de recherche dynamiques. Les phénomènes de mouillage sont étudiés depuis des siècles, et sont maintenant en grande partie bien connus. Actuellement, l'intérêt des chercheurs se porte beaucoup sur les surfaces non-mouillantes et sur les effets de l'imperfection des surfaces (défauts chimiques, rugosité, déformabilité). Les fluides complexes, dont font partie les fluides à seuil, sont également l'objet de nombreuses études. Leurs caractéristiques rhéologiques ont été en partie expliquées par des modèles phénoménologiques. Parmi les sujets de recherche actuels figurent les effets de confinement, les effets transitoires, le vieillissement, ainsi que de nombreux sujets en rapport avec les applications industrielles (par exemple, le comportement des bulles piégées ou la simulation d'écoulements complexes).

Les fluides à seuil sont en effet omniprésents dans plusieurs industries : agroalimentaire (émulsions, mousses, crèmes, pâtes...), cosmétiques (crèmes, gels), pétrole, bâtiment (enduits, ciments). Pourtant, bien que la manipulation et la mise en forme de ces matériaux mettent en jeu des problèmes d'interfaces avec l'air ou des surfaces solides, les études impliquant à la fois mouillage et rhéologie sont encore rares. Parmi les travaux récents, on peut citer, entre autres, ceux de Coussot [1], Bertola [2, 3, 4] ou Willenbacher [5].

La difficulté de ce mariage, pourtant si intéressant, tient en fait à un problème plus général que la rhéologie : le seuil, contrainte critique à partir de laquelle le fluide peut couler, est la manifestation du piégeage hors d'équilibre du fluide. Plus précisément, le système fluide ne peut pas atteindre un minimum global d'énergie et reste piégé dans un état métastable à cause d'interactions à l'échelle de ses constituants. Or les lois de la capillarité et du mouillage ont été énoncées pour des systèmes à l'équilibre.

Ainsi, ma thèse s'intéresse à la problématique suivante : « qu'est-ce qui rend le mouillage des fluides à seuil si spécial ? » En chemin, je réponds à plusieurs questions : peut-on mesurer la tension de surface d'un fluide à seuil ? On peut penser qu'il suffit de calculer une correction proportionnelle au seuil, mais la solution est-elle si simple ? Les lois de la capillarité peuvent-elles être toujours être adaptées au cas des fluides à seuil ?

Ces questions trouvent leur origine dans le travail de Baudouin Géraud, lors de sa thèse [6], également sous la direction de Catherine Barentin. Ses expériences de montée capillaire de fluides à seuil permettent de remonter à la fois à la rhéologie du fluide et à la « force capillaire »  $\Gamma \cos \theta$ .

Mais dans la littérature, les valeurs de la tension de surface  $\Gamma$  du carbopol, le fluide à seuil en question, étaient rares et souvent en désaccord. De plus l'angle de contact  $\theta$ , qui aurait pu être supposé nul, car les canaux utilisés pour les expériences étaient traités pour être très mouillants, était peut-être plus grand que prévu, mais n'était pas connu.

La première série d'expériences montre, grâce aux mesures d'adhésion de ponts capillaires, qu'il est difficile (mais possible, sous certaines conditions) de s'affranchir des effets dus au seuil lors d'une mesure de tension de surface sur un fluide à seuil. Cela explique pourquoi les valeurs de la littérature sont aussi incertaines, à l'exception de celles qui prennent en compte explicitement cet effet [1]. Dans la seconde série d'expériences, je mesure la dynamique d'étalement de gouttes de fluide à seuil, à des échelles de temps allant du dixième de milliseconde à quelques minutes. Aux temps courts, jusqu'à quelques millisecondes, le rayon de contact de la goutte augmente moins vite que prévu pour des fluides viscoélastiques, ce qui montre que l'élasticité joue un rôle sur la vitesse d'étalement initiale. Aux temps longs, les fluides viscoélastiques sans seuil s'étalent complètement, alors que les fluides à seuil s'arrêtent pour un angle de contact non nul, qui augmente avec le seuil. J'ai construit des modèles dimensionnels qui reproduisent bien les résultats expérimentaux. En outre, j'ai constaté que la rugosité de la surface solide a tendance à faire augmenter l'angle de contact, contrairement à ce que prédit la loi de Wenzel pour les fluides simples.

En plus de ces deux séries d'expériences, j'ai participé à des travaux sur la microstructure du fluide que nous utilisons, le carbopol. Je me suis aussi intéressée à des expériences de rhéologie en régime transitoire, qui apportent un éclairage intéressant sur la notion de seuil dans ces fluides.

**Propriétés du carbopol.** Le carbopol est un fluide à seuil typique et facile à préparer. C'est un gel transparent formé de pelotes de polymère (acide polyacrylique) réticulé, dissoutes dans l'eau. La concentration massique en polymère est très faible, de l'ordre de 1%, mais les pelotes sont fortement gonflées par la répulsion électrostatique entre les chaînes, qui sont chargées négativement à pH neutre.

En cisaillement stationnaire, la rhéologie du carbopol obéit à la loi empirique de Herschel-Bulkley (HB) : la contrainte visqueuse  $\sigma$  dépend du taux de cisaillement  $\dot{\gamma}$  selon  $\sigma = \sigma_y + K\dot{\gamma}^n$ . Les trois paramètres rhéologiques qui caractérisent le fluide en régime stationnaire sont  $\sigma_y$ , le seuil, en Pa,  $n$ , l'exposant, et  $K$ , la consistance, en  $\text{Pa}\cdot\text{s}^n$ . Pour mes expériences, ces paramètres sont déterminés par ajustement de la loi de HB sur des points expérimentaux obtenus au rhéomètre (figure 1, gauche).

Une autre caractéristique du fluide est son module viscoélastique, quantité complexe qui quantifie les réponses linéaires élastique et visqueuse du matériau à une faible sollicitation sinusoïdale. Cette quantité dépend de la fréquence de la sollicitation (figure 1, droite). On verra dans la suite que le module élastique  $G$  du carbopol a une influence notable sur les expériences.

Plusieurs groupes se sont déjà intéressés à la microstructure du carbopol [7, 8], et il ressort de ces études qu'elle dépend beaucoup de la façon dont le gel est préparé. J'ai participé à un travail initié par Baudouin Géraud, qui s'est inspiré d'un article de Gutowski [9] pour mesurer une taille caractéristique de structure dans nos échantillons de carbopol, et la mettre en relation avec une

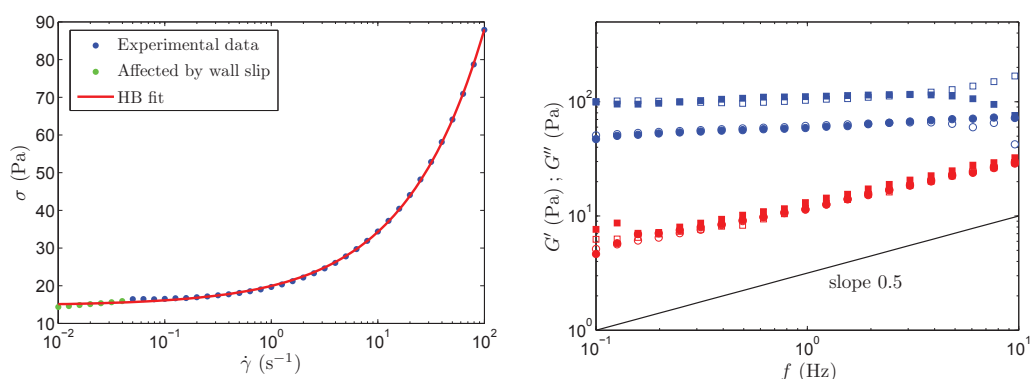


FIGURE 1 – À gauche : courbe d'écoulement pour du carbopol 1% (le gel glisse à la paroi pour les points verts). À droite : modules élastique (en bleu) et visqueux (en rouge) pour du carbopol 1% mixé (cercles) et non-mixé (carrés).

longueur de coopérativité mesurée dans d'autres expériences.

Des images de nos gels sont réalisées au microscope confocal, après marquage du polymère en solution par un fluorophore. Les images obtenues laissent voir une structure assez floue mais régulière (figure 2). Elles sont analysées soit par spectroscopie par corrélation d'image, soit par transformée de Fourier. Ces deux méthodes permettent d'extraire une taille caractéristique interprétée comme la taille moyenne des pelotes gonflées. On montre que les éléments de la structure sont d'autant plus petits que le gel est concentré en polymère. On montre aussi que la structure des gels non mixés, simplement mélangés à la main, est très hétérogène et assez différente de celle des gels mixés.

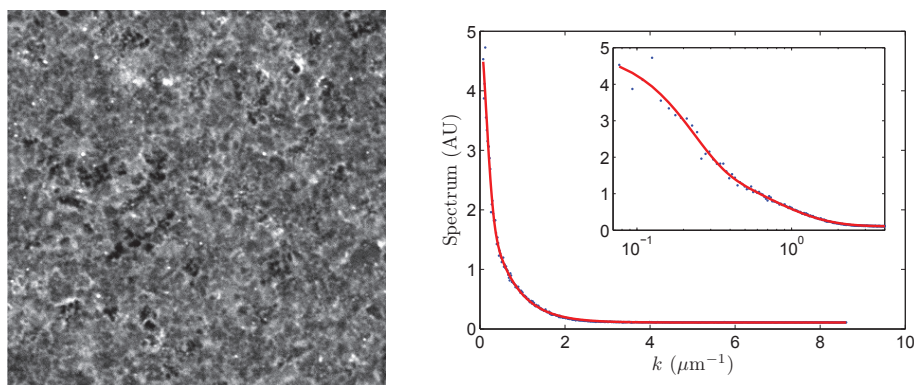


FIGURE 2 – À gauche : image de carbopol 0.5% mixé, marqué à la rhodamine, de  $59 \mu\text{m}$  de côté. À droite : spectre de Fourier radial d'une image de carbopol 1% mixé. Insert : la même courbe avec des abscisses logarithmiques. Taille caractéristique extraite :  $1.66 \mu\text{m}$ .

**Adhésion de ponts capillaires.** Une des expériences principales de ma thèse a été l'étude de l'influence du seuil sur la force d'adhésion d'un pont capillaire, et par extension, sur la mesure de la tension de surface. Ces mesures ont été réalisées grâce au tensiomètre à pont capillaire construit au laboratoire par Hélène Delanoë-Ayari, à l'origine pour mesurer une tension de surface effective d'agrégats cellulaires. L'avantage de cette technique est qu'elle permet une mesure précise de la

tension de surface avec une seule goutte, de petite taille, de matériau. L'idée était donc d'amplifier les effets capillaires par rapport au seuil en réduisant la taille du système, car plus un système est petit, plus les effets de surface deviennent importants par rapport aux effets de volume.

Le principe de l'expérience est le suivant : une goutte de fluide d'une dizaine de microlitres est déposée entre deux lames de verre horizontales, rendues très hydrophiles par un traitement au plasma d'ozone ou au mélange piranha. La goutte mouille les deux surfaces de verre et forme un pont capillaire. La courbure de la surface provoque une dépression dans le liquide (loi de Laplace) qui génère une force attractive  $F$  entre les deux lames de verre. Cette force, de l'ordre de quelques centaines de  $\mu\text{N}$ , est mesurée grâce à la mesure de déflexion d'un levier métallique solidaire d'une des lames de verre.

On montre, pour un fluide sans seuil, que la force d'adhésion est exactement le produit de la tension de surface du fluide  $\Gamma$  par  $L$ , un facteur purement géométrique qui peut être mesuré à partir du profil du ménisque. Cette relation a été vérifiée par des mesures sur de l'eau pure et de l'huile silicone. Le rapport d'aspect du pont capillaire peut être ajusté par un micromanipulateur, ce qui permet d'enregistrer, pour une même goutte, une trentaine de couples  $F$ - $L$ . Les points sont rassemblés dans un graphe et ajustés par une loi linéaire dont la pente est  $\Gamma$ . Les tensions de surface tabulées sont retrouvées avec une incertitude maximale de  $1 \text{ mN/m}$ .

En ce qui concerne le carbopol, on constate que la pente de  $F(L)$  n'est pas la même si le pont a été étiré ou bien comprimé pendant l'expérience. Il ne s'agit pas d'un effet dynamique car le pont est déformé par échelons et les couples  $F$ - $L$  ne sont relevés que quand la force atteint un plateau. Une expérience typique consiste en une dizaine d'échelons d'étirement suivie d'une dizaine d'échelons de compression, puis de quelques nouveaux échelons d'étirement. Le graphe  $F(L)$  qui en résulte a l'allure de la figure 3, avec des points alignés selon deux droites de pentes différentes. L'écart des deux pentes augmente clairement avec le seuil du fluide.

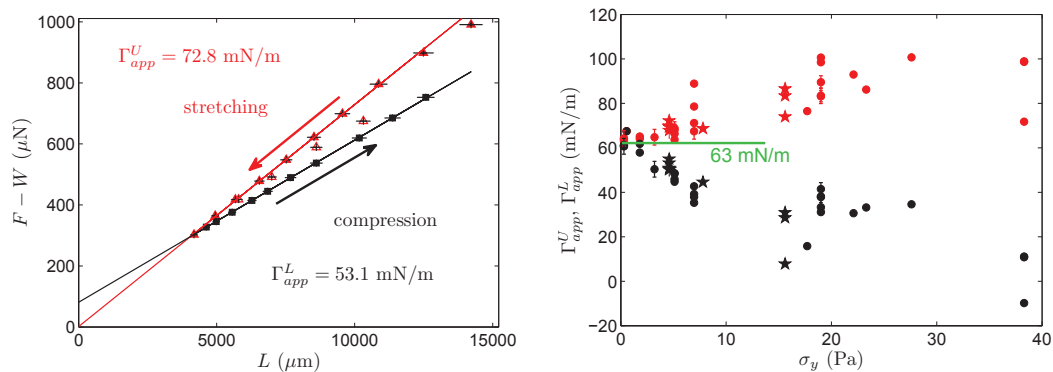


FIGURE 3 – À gauche : graphe  $F(L)$  pour une goutte de carbopol 0.25 % non mixé, de seuil  $\sigma_y = 5 \text{ Pa}$ . À droite : résumé des pentes mesurées (tensions de surface apparentes) en extension (rouge) et en compression (noir) en fonction du seuil.

Comme la pente des droites peut être interprétée comme une tension de surface, on voit que la tension de surface apparente du carbopol dépend du seuil et de la façon dont le fluide a été déformé *avant* la mesure.

Un modèle élasto-plastique en géométrie simplifiée a été développé pour expliquer l'aspect

de ces graphes. Deux géométries extrêmes sont considérées : un pont très étiré, avec une géométrie de filament quasi-cylindrique, et un pont très comprimé, en forme de galette. Dans chaque géométrie, la répartition des contraintes internes est simple. Ces contraintes sont intégrées sur la surface de contact du fluide avec la surface solide, ce qui fait apparaître une force élasto-plastique qui s'ajoute algébriquement à la force d'adhésion capillaire. Si le pont a été étiré, la force élasto-plastique est positive, et s'il a été comprimé, elle est négative. On arrive ainsi à reproduire très fidèlement l'allure des graphes  $F(L)$ .

On montre aussi, grâce au modèle, l'importance cruciale de l'élasticité  $G$  du fluide à seuil. En effet, si la déformation cumulée est plus faible que  $\gamma_c = \sigma_y/G$ , les contraintes internes sont déterminées par la réponse élastique du gel, alors que si elle est supérieure à cette valeur, les contraintes internes sont contrôlées par le seuil  $\sigma_y$ .

Cette expérience apporte donc des conclusions intéressantes. Premièrement, elle explique la disparité des valeurs de tension de surface trouvées dans la littérature. En particulier, on trouve parfois des valeurs nettement plus élevées que 75 mN/m, ce qui pourrait s'expliquer par la méthode de mesure, souvent une méthode d'arrachement qui implique une force élasto-plastique positive. Ensuite, les mesures réalisées permettent de dire que la tension de surface du carbopol diminue légèrement quand la concentration en polymère augmente (par exemple pour une concentration de 0.75%, elle n'est que de 59 mN/m). Troisièmement, si on calcule une correction à la tension de surface apparente, il faut tenir compte du rapport entre la déformation du fluide et la quantité  $\sigma_y/G$ . Plus fondamentalement, contrairement à ce que nous pensions au départ, l'effet du seuil ne devient pas négligeable par rapport aux effets capillaires même quand le système est « petit » (c'est-à-dire plus petit que  $\Gamma/\sigma_y \sim 6$  mm).

**Étalement de gouttes.** La deuxième partie majeure de ma thèse porte sur la dynamique d'étalement de gouttes de fluides complexes, sans vitesse initiale. Elle se subdivise en plusieurs questions :

1. Le rayon de contact des gouttes augmente-t-il en loi de puissance du temps comme pour les fluides simples ?
2. Les différences avec les fluides simples sont-elles dues au seuil ou à l'élasticité ?
3. Retrouve-t-on la loi de Tanner ou son adaptation aux fluides rhéofluidifiants aux temps longs ?
4. Quelles sont les influences respectives des énergies de surface et du seuil sur l'angle de contact final après l'étalement d'une goutte de fluide à seuil ?

Pour répondre aux deux premières questions, un premier dispositif a été utilisé : une visualisation de profil à la caméra rapide, jusqu'à 50000 images par seconde. Plusieurs fluides ont été testés : des fluides simples (eau, mélange eau-glycérol, solution de tensioactifs), des fluides complexes sans seuil, mais rhéofluidifiants et viscoélastiques (solutions d'acide polyacrylique ou PAA à différentes concentrations) et des fluides à seuil (carbopol mixé et non mixé).

Comme le prédit la théorie, le rayon des gouttes de fluides simples croît en puissance du temps, avec un exposant  $p = 0.5$ , quelles que soient la viscosité ou la tension de surface du fluide. Pour les solutions de PAA, le rayon croît également en puissance du temps, mais avec un exposant plus faible, qui décroît quand la concentration en polymère augmente (figure 4). Enfin, pour le carbopol, l'exposant est encore plus faible que pour le PAA, à concentration de polymère identique, et il semble décroître quand le seuil et l'élasticité augmentent. Un modèle qui fait intervenir la variation d'énergie potentielle (gravitationnelle) de la goutte et la dissipation visqueuse près de la ligne triple permet de retrouver les bons exposants pour les fluides simples et les fluides complexes peu concentrés. La dépendance manifeste avec la concentration des fluides en polymères n'est pas prédite par le modèle développé ici.

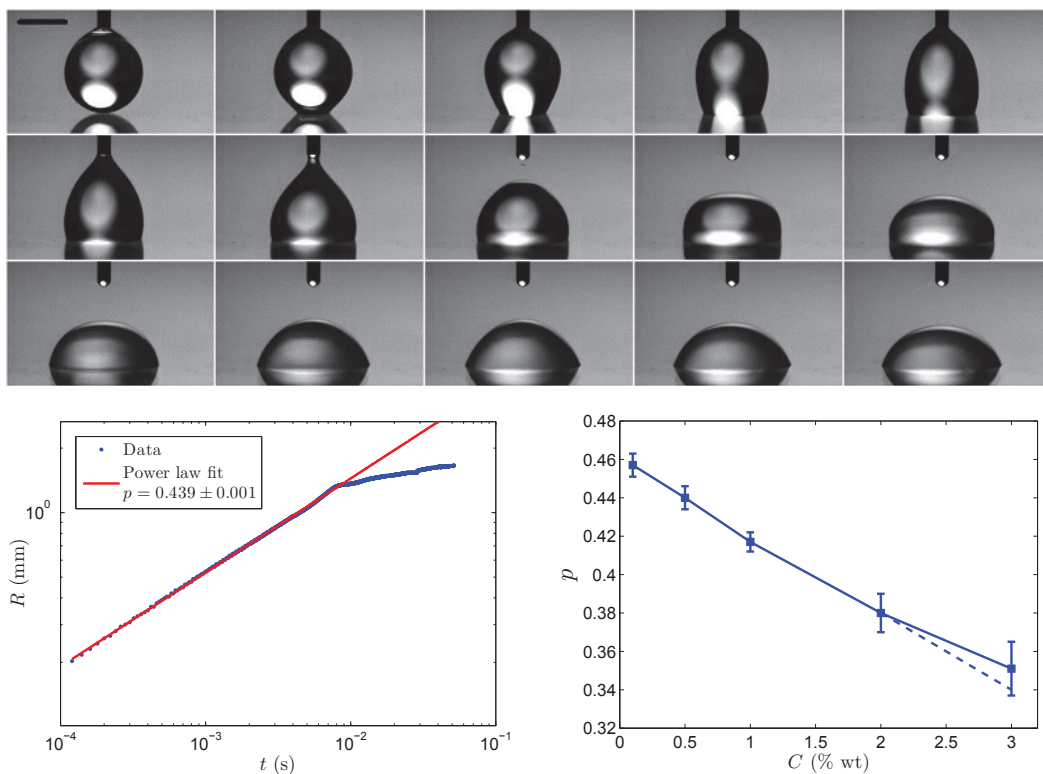


FIGURE 4 – En haut : suite d’images extraites d’un film d’étalement. Le fluide est un mélange eau-glycérol. L’intervalle de temps entre chaque image est de 1 ms. La barre noire représente 1 mm. En bas à gauche : évolution du rayon de contact d’une goutte de solution de PAA à 1%, en échelle logarithmique. La droite rouge est un ajustement en loi de puissance. L’exposant est indiqué dans la légende. En bas à droite : exposant moyen mesuré pour la dynamique d’étalement en fonction de la concentration en PAA.

Les deux dernières questions sont abordées grâce à un deuxième dispositif dans lequel la goutte est filmée par en dessous à 100 images par secondes pendant 3 minutes puis photographiée de profil dans son état final. les fluides sont soit des solutions de PAA soit des carbopols de différents seuils.

Les solutions de PAA, rhéofluidifiantes, vérifient la loi de Tanner modifiée [10] et s’étalent complètement, sous réserve que la ligne de contact ne soit pas piégée par des défaut de surface. En revanche on voit que pour les fluides à seuil, l’étalement s’arrête après quelques dizaines de

secondes (figure 5). L'angle de contact final est non nul, alors que les énergies interfaciales n'ont aucune raison d'être différentes de celles des solutions de PAA, la composition chimique étant la même. L'angle final est donc uniquement dû au seuil. Un modèle dimensionnel permet de retrouver l'évolution de l'angle avec le seuil.

Une autre constatation très intéressante est que pour un même seuil, l'angle de contact final est plus élevé sur une surface rugueuse que sur une surface lisse (à matériau et traitement de surface identique). La loi de Wenzel prédit pourtant le comportement inverse, mais pour des fluides sans seuil. Cet effet est interprété comme dû au glissement du gel contre la surface lisse.

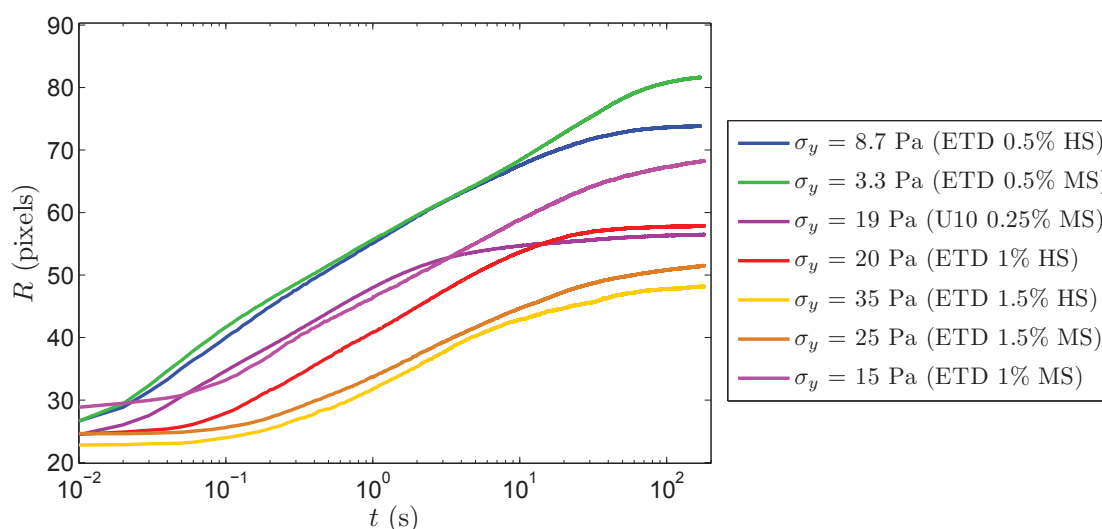


FIGURE 5 – Évolution temporelle du rayon de contact  $R(t)$  pour des carbopols de différents types, concentrations et mixages.

**Conclusion.** Lors de cette thèse, j'ai réalisé plusieurs expériences sur des fluides complexes, plus particulièrement à seuil. Les résultats ont permis de mettre en évidence la façon dont la capillarité et la rhéologie des fluides complexes, souvent étudiés séparément, se combinent dans des situations classiques : adhésion capillaire, étalement de gouttes. Notamment, l'effet de la contrainte seuil et de l'élasticité a été étudié en détail, pendant la dynamique transitoire comme dans l'état final statique. Des phénomènes d'hystérésis liés à la présence du seuil ont fait émerger l'idée d'une analogie entre la friction de la ligne triple et le seuil en rhéologie.

Ainsi, j'ai montré que la tension de surface des fluides à seuil pouvait être déduite de la mesure de la force d'adhésion d'un pont capillaire, à la condition que la géométrie du champ de contrainte soit connue. Pour cela un écoulement contrôlé doit être d'abord imposé au système, et l'élasticité du fluide doit être grande devant le seuil, de telle façon que la déformation critique nécessaire pour atteindre la contrainte seuil soit petite. Le rôle de l'élasticité ne doit pas être négligé dès lors que l'on ne considère pas un écoulement permanent. J'ai également commencé à explorer l'état final de gouttes posées de fluides à seuil. Je montre que l'existence du seuil empêche la goutte d'atteindre l'état prévu par la loi d'Young-Dupré. De plus, la rugosité de la surface solide intervient aussi sur l'angle final, car le glissement est à l'origine d'une réduction de

la contrainte à la paroi.

Ce travail m'a permis de développer de nombreuses compétences nouvelles et d'affiner mes connaissances. Mais au-delà de la perspective personnelle, je pense que les expériences et les réflexions menées durant cette thèse permettront de mieux appréhender le mouillage de fluides à seuil, et de le considérer comme une situation complexe et hors-équilibre plutôt que comme une simple compétition énergétique.

# Contents

<b>Introduction</b>	<b>17</b>
<b>1 Preliminary concepts on rheology and wetting</b>	<b>25</b>
1.1 Rheology . . . . .	26
1.1.1 Definitions . . . . .	26
1.1.2 Standard measurements . . . . .	27
1.1.3 Specific features of yield-stress fluids . . . . .	28
1.2 Capillarity, static laws . . . . .	31
1.2.1 Definition of interfacial tension . . . . .	31
1.2.2 Static wetting and Young's law . . . . .	32
1.2.3 Laplace's law and the shape of drops . . . . .	33
1.2.4 Jurin's law and capillary rise . . . . .	34
1.3 Capillary dynamics . . . . .	35
1.3.1 Moving contact lines and drop spreading . . . . .	35
1.3.2 A few words on impacts . . . . .	36
1.3.3 Surface waves and fluctuations . . . . .	37
1.3.4 Instabilities due to surface tension . . . . .	38
<b>2 Wetting with friction: contact angle hysteresis and yield-stress fluids</b>	<b>41</b>
2.1 The friction family . . . . .	42
2.1.1 What characterizes friction? . . . . .	42
2.1.2 Friction of the triple line . . . . .	43
2.1.3 Yield stress . . . . .	45
2.2 Contact angle hysteresis consequences . . . . .	45
2.2.1 Sliding drops . . . . .	45
2.2.2 Evaporation . . . . .	46
2.2.3 Tubes and pores . . . . .	46
2.3 Yield stress and capillarity . . . . .	47
2.3.1 Laplace's law and the shape of drops . . . . .	47
2.3.2 Filament breakup and dripping . . . . .	48
2.3.3 Coating and films . . . . .	48
2.3.4 Capillary rise . . . . .	48

2.3.5	Measurement of surface tension . . . . .	49
2.4	Conclusion . . . . .	51
<b>3</b>	<b>Carbopol: rheology and structure</b>	<b>53</b>
3.1	Preparation . . . . .	54
3.2	Rheology . . . . .	54
3.2.1	Characterization of the samples . . . . .	54
3.2.2	Dynamics around the yielding . . . . .	56
3.3	Microstructure . . . . .	60
3.3.1	Measurement protocol . . . . .	60
3.3.2	Results . . . . .	65
3.3.3	Perspectives . . . . .	67
<b>4</b>	<b>Adhesion of a capillary bridge of yield-stress fluid</b>	<b>69</b>
4.1	Setup and protocol . . . . .	70
4.2	Simple fluids . . . . .	74
4.2.1	Expectations . . . . .	74
4.2.2	Experimental results . . . . .	76
4.3	Observations with carbopol . . . . .	78
4.4	Elastoplastic model . . . . .	80
4.4.1	General expression of the elastoplastic force . . . . .	81
4.4.2	Filament approximation . . . . .	81
4.4.3	Pancake approximation . . . . .	82
4.4.4	Resulting curves and comparison with experiments . . . . .	83
4.5	Discussion . . . . .	86
4.5.1	Influence of yield stress and volume . . . . .	86
4.5.2	Influence of elasticity . . . . .	86
4.5.3	Effect of the initial stress . . . . .	88
4.5.4	Surface tension . . . . .	89
4.6	Conclusion . . . . .	91
4.7	Perspectives . . . . .	92
<b>5</b>	<b>Spreading of yield-stress fluid drops</b>	<b>95</b>
5.1	Experiments at short timescales . . . . .	96
5.1.1	Setup and protocol . . . . .	96
5.1.2	Observations . . . . .	99
5.1.3	Model and discussion . . . . .	104
5.1.4	Conclusions . . . . .	106
5.2	Experiments at long timescales . . . . .	108
5.2.1	Setup and protocol . . . . .	108
5.2.2	Radius evolution in time . . . . .	110
5.2.3	Final contact angle . . . . .	114

	17
5.2.4 Conclusions . . . . .	118
<b>General conclusion</b>	<b>119</b>
Conclusions . . . . .	119
Perspectives . . . . .	120
<b>Annexes</b>	<b>121</b>
A Rheological parameters of the carbopols used . . . . .	124
B Effect of CAH on the adhesion of capillary bridges . . . . .	126
B.1 Experiments . . . . .	126
B.2 Friction-based model . . . . .	127
B.3 Perspectives . . . . .	129
C SFSR spectroscopy measurements . . . . .	130
C.1 Setup and protocol . . . . .	130
C.2 Results . . . . .	130
C.3 Comments . . . . .	131
D Spreading dynamics calculations . . . . .	132



# Introduction

Yield-stress fluids are widely used complex fluids, and they have the specificity not to flow when submitted to a stress under a critical value called yield stress ( $\sigma_y$ ). This category gathers many usual fluids such as gels, pastes, creams, emulsions, cements. . . To give an idea of the difference between yield-stress fluids and simple fluids, one can imagine trying to pour mayonnaise or hair gel and see the obvious difference with water, or even liquid honey. Mayonnaise and hair gel are not just very viscous. If they are not forced to flow, by a shake or with a tool, they won't move under their own weight. This specific feature gives yield-stress fluids very useful and fascinating properties.

When I came to the lab for the first time and met Catherine, I was immediately excited by what she told me about yield-stress fluids. At this time I understood that our goal was to measure the surface tension of a yield-stress fluid from the adhesion of a small enough capillary bridge. This might sound naive of me to have believed that research could be so trivial. After three years of experiments, deep thinking, questioning, failure to understand and instants of sudden inspiration, I now feel much more mature about the physics of complex fluids and wetting.

Indeed, the actual question is much more interesting and has very deep implications, both practical and conceptual: **why is wetting of yield-stress fluids so special?** Wetting is an ancient and well-known subfield of soft matter physics. Some of the most famous scientists have contributed to this established knowledge. Today, the research interest is focused on non-wetting surfaces and on the effect of the surface imperfection (chemical defects, roughness, softness). On the other hand, yield-stress fluids have been studied a lot in the last decades because of their practical use. Their rheology was partly explained by phenomenological models. Among the present research topics, we see transient effects, confinement, ageing and many questions related to industrial issues (for example, the behavior of bubbles trapped in the material or complex flows simulation).

However, the combination of the two has not drawn the attention it deserves. Despite the frequent occurrence of situations where a yield-stress fluid is in contact with a solid surface or with air, thus involving wetting, few publications can be found on the interaction of yield stress with wetting [1, 2, 3, 4, 5]. Yield-stress fluids seem to be mostly considered as complex fluids among others. Yet they are special, in the sense that the yield stress is the macroscopic manifestation of the trapping of the system in a metastable state. They are thus fundamentally out-of-equilibrium systems, whereas capillarity is based on equilibrium quantities. The marriage of capillarity and yield stress is not so easy.

Apart from the practical consequences of studying the interaction of yield stress with capillarity, which are already crucial, the problem raises interesting physical questions. In particular, can we define the surface tension of a yield-stress fluid in the same way as the other fluids? Can we find conditions in which the yield stress is negligible compared to surface tension? Can we always adapt the classical laws of capillarity, developed for equilibrium situations, to yield-stress fluids? Is it even possible to predict the final state of a yield-stress fluid system in contact with other phases?

This thesis proposes to open a way towards these questions, by revisiting experimentally two extremely classical wetting situations, using a yield-stress fluid. The first situation is the adhesion of a capillary bridge, often used to illustrate the power of capillary forces for a general audience. The second situation is the spreading of a drop on a perfectly wetting surface, which is one of the simplest wetting experiments one can think of. I will show that even these apparently very simple cases contain the beginning of an answer to the questions above. This will hopefully improve the global understanding of the effect of yield stress on wetting.

\* \* \*

Our initial idea was to reduce the size of the yield-stress fluid system, so that the surface effects would dominate the bulk yield stress effects. It was based on several recent papers where it was shown that the yield stress effects on capillary experiments were proportional to the system dimension. It also followed the work of my predecessor Baudouin Géraud who performed capillary rises of carbopol<sup>1</sup>, our model yield-stress fluid [11]. With channels of different widths Baudouin could measure the yield stress  $\sigma_y$  of the gel and the “capillary force”  $\Gamma \cos \theta$  (where  $\Gamma$  is the surface tension and  $\theta$  is the contact angle) simultaneously. It was somewhat difficult to compare his value for this capillary force with the literature, because on the one hand no one had really addressed the issue of the contact angle of carbopol on glass, and on the other hand the value of the surface tension  $\Gamma$  of carbopol was still debated. Some assumed that it was the same value as the water surface tension, relying on measurements by Hartnett’s group in the 1990’s [12, 13], and maybe because carbopol is composed nearly exclusively of water. Yet it is reasonable to think that even the little amount of polymer in the gel lowers its surface tension. However the available measurements did not agree with one another [14], and sometimes the measurement method was not very detailed [2, 15].

At the same period Boujlel and Coussot were working on measurements of the surface tension of carbopol by a plate withdrawal method [16, 1]. Because the yield stress creates a supplementary resisting force on the plate, proportional to  $E$ , the thickness of the plate, and to  $\sigma_y$ , the yield stress of the fluid, they made several measurements, varying both  $E$  and  $\sigma_y$ . They obtained  $\Gamma = 66 \text{ mN/m}$ , that is 10% less than pure water surface tension, by extrapolating the apparent surface tension to vanishing  $\sigma_y E$ . This value is consistent with the one of a dilute polymer solution in water. However, to vary  $\sigma_y$ , Boujlel and Coussot had to change the polymer concentration between 0.1% and 0.5%, and this can *a priori* induce surface tension variations.

---

<sup>1</sup>Strictly speaking, Carbopol is a commercial name for a water-soluble crosslinked polymer, but in this thesis the microgel obtained from Carbopol dissolution in water will always be called simply carbopol.

The idea of a dimensionless number quantifying the effects of the yield stress on situations initially developed for simple fluids is often found in the work of Bertola. He addresses a lot of capillary problems with polymer solutions and in particular with yield-stress fluids: capillary rise [17], filament breakup [2], spreading [3], impacts [4]. In many of these works he introduces a dimensionless number called the Bingham-Capillary number and defined as  $\mathcal{B} = \frac{\sigma_y a}{\Gamma}$  with  $a$  the relevant system size. This number compares capillary effects and yield-stress effects. Basically, if  $\mathcal{B} > 1$  the system's state will be controlled mainly by the fluid's yield stress, and reversely if  $\mathcal{B} < 1$  the capillary effects will be dominant. This is intuitive if we think of a drop of yield-stress fluid: if its volume  $V < (\Gamma/\sigma_y)^3$  then the drop will be spherical, like a drop of simple fluid. But if it is bigger and  $V > (\Gamma/\sigma_y)^3$  it will rather look like a small mound.



However, during the project, the more I thought about dimensionless numbers involving the yield stress, the more troubled I felt. During my studies I learned that dimensionless numbers compare energies. Moreover I remember that when these dimensionless numbers were of the order of 1 both energies played a role and the equations could not be simplified. But here, even if the surface energy was something concrete in my mind, I could not figure out what a “yield stress energy” could mean physically. I understood that there was a kind of competition between the capillary energy and the yield stress, which prevented the system from deforming to its thermodynamical equilibrium state. I also knew that when the size of a liquid system is reduced, surface effects become predominant. But something remained unclear. Making experiments and manipulating complex fluids helped me to understand the real meaning of  $\mathcal{B}$ .

During the first part of the project, I investigated the adhesion force of a capillary bridge of carbopol. I could notice that the yield stress was not negligible even if I made “small” capillary bridges. I could also observe the characteristic hourglass shape of the bridge, and it was obviously not an equilibrium profile.

Progressively I understood that  $\mathcal{B}$  does not compare energies, but stresses. It compares the yield stress with the Laplace pressure resulting from the surface curvature. If this pressure exceeds the yield stress then the fluid has to flow and the surface can relax towards an equilibrium shape. But this means that  $a$  is not just a typical size of the system.  $a$  is the inverse of the mean curvature  $C$  of the surface. In particular, for capillary bridges whose mean curvature can be very close to zero,  $a$  can be really big, which explains why these bridges seem never to relax to an equilibrium shape.

Finally, in collaboration with Marie Le Merrer and H el ene Delano -Ayari, we could find a model explaining why and how the adhesion of a capillary bridge of yield-stress fluid is modified with respect to a simple fluid. The model takes into account the history of deformation and also the

role of the fluid elasticity below the yield stress. The qualitative agreement with the experimental data is excellent.

The second part of the project focused on the spreading of drops. Several issues were addressed: first, the influence of the complex viscosity and of elasticity on the initial dynamics; secondly, the influence of the yield stress on the later dynamics and on the final state. The effect of the surface roughness was also investigated.

This part allowed me to fully realize that the final state of a spreading yield-stress fluid drop does not simply depend on a potential minimization. Of course at the scale of the fluid components everything is at mechanical equilibrium but it is not possible to write an energy from the internal stress in the fluid or from the wall roughness. On this subject, I quote an extract from a review on drop impacts by Yarin [18]:

“Range & Feuillebois (1998) argued that their experimental data on splashing threshold for normal drop impact on a dry surface, like those of Stow & Hadfield, can be described in terms of the critical Weber number  $We_S$  as a function of the surface roughness. Rioboo et al. (2001) claimed that the thresholds between the various scenarios [i.e. the different impact regimes] cannot be quantified in terms of the dimensionless groups  $We$ ,  $Re$ ,  $Oh$ , and  $\mathcal{K}$  [ $Oh$  and  $\mathcal{K}$  are combinations of  $We$ , the Weber number, and  $Re$ , the Reynolds number] — a clear manifestation that **these dimensionless groups are insensitive to the wettability and roughness effects**, which are of the utmost importance in drop impacts on a dry surface.”

The emphasized part is very interesting. It says that no dimensionless number can capture the effects of specific interactions, like those causing wetting hysteresis. This can be understood if we realize that a dimensionless number compares well-defined energies, and that wetting hysteresis is not expressed in terms of an energy, because it is an out-of-equilibrium effect.

Finally, the main message of this work is that yield-stress fluids cannot reach a global energy minimum because of the trapping of the system in a metastable state. Moreover this state results from disordered microscopic interactions and it cannot be calculated. Therefore, the usual laws of capillarity, valid at equilibrium, cannot be used without the addition of empirical terms accounting for the trapping. This situation is very similar to solid friction in mechanics, or even to contact angle hysteresis problems, to stay in the wetting field. For this reason, I will refer to these three phenomena (solid friction, yield stress and contact angle hysteresis) as **frictional situations**.

\* \* \*

**Global outline.** The manuscript is divided into 5 chapters.

The first chapter introduces useful notions about rheology and wetting. The reader already familiar with these two fields can jump directly to the second chapter, where I discuss a certain number of frictional cases in the broad field of capillarity.

Then I will switch to more experimental details. The third chapter is dedicated to the main material I used for my experiments: carbopol. Finally, in the fourth and fifth chapters I will detail

my two main experiments: respectively the adhesion of a capillary bridge and the spreading of drops.

These chapters are followed by a conclusion and a few annexes.



# Chapter 1

## Preliminary concepts on rheology and wetting

### Contents

---

<b>1.1 Rheology</b>	<b>26</b>
1.1.1 Definitions	26
1.1.2 Standard measurements	27
1.1.3 Specific features of yield-stress fluids	28
Models for the flow curve	28
Determining the yield stress	29
Choice of a geometry	29
Wall slip	30
Transient response	30
<b>1.2 Capillarity, static laws</b>	<b>31</b>
1.2.1 Definition of interfacial tension	31
1.2.2 Static wetting and Young's law	32
1.2.3 Laplace's law and the shape of drops	33
1.2.4 Jurin's law and capillary rise	34
<b>1.3 Capillary dynamics</b>	<b>35</b>
1.3.1 Moving contact lines and drop spreading	35
1.3.2 A few words on impacts	36
1.3.3 Surface waves and fluctuations	37
1.3.4 Instabilities due to surface tension	38

---

In this first chapter, I will present a few basic concepts on rheology and capillarity, so that the reader who does not have background on these subjects can understand the following parts of the thesis. The explanations are intentionally very concise, but most of the time I mention one or two main references (generally textbooks or reviews) to which one can refer for more information.

## 1.1 Rheology

As the present thesis deals with complex fluids and in particular yield-stress fluids, I will start with some notions of rheology. First, I will define usual quantities used in the field. Then, I will talk about measurement techniques, and finally elaborate more on the specificities of yield-stress fluids.

### 1.1.1 Definitions

Most of the time in rheology, fluids are considered incompressible, so that the only relevant deformation mode is shear. In the general case, deformation is described by a second-order tensor, but rheometry tools are very often designed in such a way that this tensor can be reduced to a scalar.

In this case of a simple one-dimensional shear, a layer of fluid of thickness  $h$  is deformed on a length  $\delta X$  (figure 1.1).

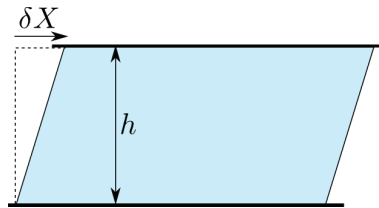


Figure 1.1 – Schematic drawing of the simple shear geometry.

We define the following quantities:

**Shear deformation**  $\gamma$  is defined as  $\delta X/h$ . It is dimensionless.

**Shear rate**  $\dot{\gamma}$  is the time derivative of shear deformation. It quantifies the deformation speed.

**Shear stress**  $\sigma$  is the tangential force per unit surface exerted by an operator on the liquid layer to cause a shear deformation, or alternatively exerted by the sheared material on the operator.

**Viscosity**  $\eta$  is the ratio of the shear stress to the shear rate. It is expressed in Pa s.

**Complex elastic modulus**  $G^* = G' + iG''$  is a complex quantity representing the linear response to a small oscillatory shear  $\gamma^*(\omega)$ . It is defined as  $G^*(\omega) = \sigma^*(\omega)/\gamma^*(\omega)$ .  $G'$  is called the **elastic modulus** and it is a measure of the elastic response of the material at pulsation  $\omega$ .  $G''$  is the **loss modulus** and it quantifies the viscous response of the material as a function of  $\omega$ .  $G'$  and  $G''$  are expressed in Pa.

**A flow curve** is the (stationary, see 1.1.2) stress plotted versus the shear rate.

A **Newtonian fluid** has a unique viscosity for all shear rates. In other words the stress is proportional to the shear rate. These fluids have no elastic response. Water is a Newtonian fluid, for example.

A **shear-thinning fluid** has a viscosity that decreases when the shear rate increases. This category includes many dilute polymer solutions for example.

A **shear-thickening fluid** is the reverse case. Its viscosity increases when the shear rate increases. A popular example of shear-thickening fluid is a cornstarch suspension.

A **viscoelastic fluid** has a dominating elastic response at high shear frequency and a more viscous response at low frequency. A typical example is the paste "silly-putty" which bounces when launched against a surface but spreads slowly when at rest. These materials are characterized by one or several relaxation times coming from a microscopic origin.

A **yield-stress fluid** is shear-thinning above a critical stress, the **yield stress**  $\sigma_y$ , and behaves as a soft elastic solid below  $\sigma_y$ . Therefore, yield-stress fluids are sometimes defined as "visco-elastoplastic". More specificities of yield-stress fluids will be discussed in section 1.1.3.

The typical flow curves of the fluids introduced above are presented in figure 1.2.

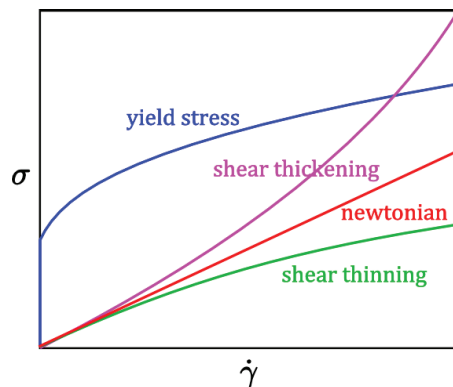


Figure 1.2 – Schematic flow curves of the fluids presented in the text.

### 1.1.2 Standard measurements

Several techniques give access to the different properties of complex fluids. I will mostly approach those used with a rotative rheometer. For other measurement techniques see for example reference [19, Chap. 1].

**Principle of a rotative rheometer.** A rotative rheometer consists in a rotor equipped with a tool, and in a stator. The geometry of the rotative tool and the stator can vary, and the space between the two is called the gap (generally of the order of the millimeter). The device imposes either a rotation or a torque to the liquid sample placed in the gap, and the response (torque or rotation, respectively) is recorded. The shear deformation, the shear rate and the stress are then

computed from the knowledge of the gap geometry. The most common geometries are the parallel plates, the cone-plate and the Couette cell (figure 1.3).

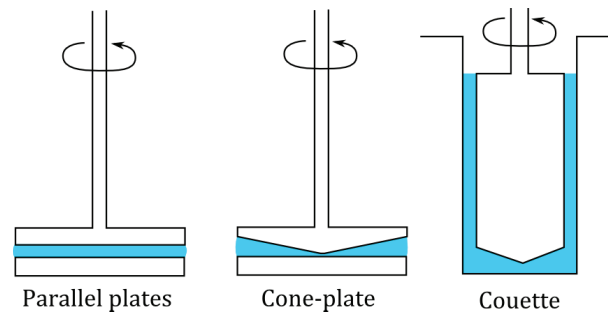


Figure 1.3 – Most common gap geometries for a rotative rheometer.

**Constant shear rate, stationary regime.** The standard procedure to measure a single viscosity or a full flow curve is to shear the material at a constant shear rate until a constant stress value is reached.

**Linear oscillatory shear.** To determine the complex elastic modulus  $G^*(\omega)$  the material is submitted to a small oscillatory shear and the linear stress response is measured simultaneously. The amplitude of the deformation must be small enough for the material to respond linearly. Its maximum value depends on the material: for a polymer microgel  $\gamma_{\max} \approx 1\%$  but it can be as small as  $0.01\%$  for a concentrated cement paste.

**Transient responses.** Sometimes the characteristics of a fluid can be explored through its transient response to a step of shear deformation (relaxation experiment), of shear rate (startup experiment), or of stress (creep experiment). These methods are mostly used for industrial purposes or, from a fundamental point of view, to test microscopic models.

### 1.1.3 Specific features of yield-stress fluids

Main reference: [19, Chap. 5]

#### Models for the flow curve

To account for the specific flow curve of yield-stress fluids, several empirical models have been proposed.

- The simplest is the Bingham model: the stress grows linearly with the shear rate above  $\sigma_y$  ( $\sigma = \sigma_y + \eta\dot{\gamma}$ ).
- The most widespread is the Herschel-Bulkley (HB) model: above  $\sigma_y$ ,  $\sigma = \sigma_y + K\dot{\gamma}^n$ , where  $K$  is the consistency and  $n$  the HB exponent of the fluid.
- The last one is the Casson model:  $\sqrt{\sigma} = \sqrt{\sigma_y} + \sqrt{\eta\dot{\gamma}}$ .

Each of these models describes different fluids. For example, the Casson model is often used to describe the flow of blood in narrow arteries, while the Herschel-Bulkley model is more suitable for flows of microgels or emulsions. However the Bingham model is a simpler approximation for theoretical calculations.

### Determining the yield stress

The easiest method to measure the yield stress value is to acquire a flow curve and to fit the points with a HB model (figure 1.4). A few precautions must be taken (see the next paragraphs) but it gives rather reproducible results, provided that the volume of the sample is precisely the one of the rheometer cell.

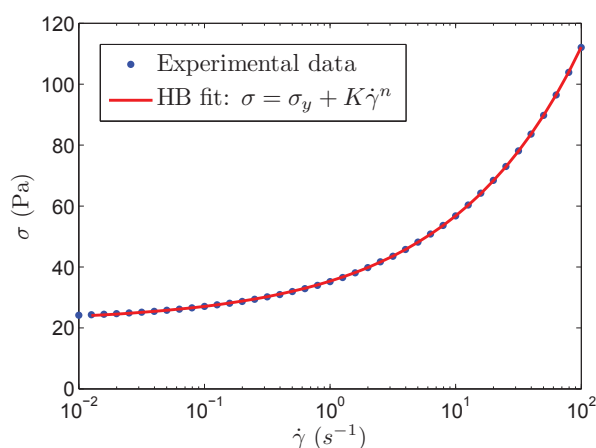


Figure 1.4 – Example of a real flow curve for 0.25% Ultrez10 Carbopol, with the Herschel-Bulkley fit. Here  $\sigma_y = 22$  Pa,  $K = 13.5$  Pa s<sup>n</sup> and  $n = 0.41$ .

Other methods are sometimes seen in the literature. One of them requires patience but is very precise: a constant stress is applied on the sample and the deformation is recorded through time. If this stress is above the yield stress the fluid will first creep (Andrade law), which means that the material deforms slower and slower. Then it will start to fluidize and flow after a time  $\tau$  proportional to  $(\sigma - \sigma_y)^{-\beta}$  (shown for polymer microgels [20]). Fitting  $\tau$  as a function of the applied stress gives a reliable value of the yield stress.

### Choice of a geometry

As the stress dependency on the shear rate is non-linear for complex fluids, great care must be taken when using a parallel plates geometry. Because the gap is constant through the plates radius, the local shear rate is not homogeneous in the fluid sample. Yet the rheometer measures an integrated stress via the torque and returns an averaged stress, assuming a uniform viscosity. It is hence compulsory to rectify the stress values with a function taking into account the expected flow curve form. In particular the raw yield stress returned by the rheometer equipped with parallel plates is  $\frac{4}{3}\sigma_y$  [21].

Other possible geometry choices are the cylindrical Couette cell or the cone-plate geometry.

The Couette cell has however a few drawbacks when dealing with a yield-stress fluid. First, the gap must be narrow with respect to the cylinder radius to ensure a fine definition of the shear rate, but large with respect to the material components size to avoid confinement effects. Secondly, it is more difficult to reduce boundary effects at the ends of the cylinders.

The cone-plate geometry is a good choice for yield-stress fluids. The shear rate is unique in the whole sample for a given rotation speed ensuring a reliable stress measurement. If necessary a closed humidity chamber can be put around the cell to reduce evaporation at the sample edge.

### Wall slip

Contrary to simple fluids [22], yield-stress fluids are known to exhibit a large slip velocity when flowing near a solid surface [23, 24]. This causes artifacts when rheological measurements are performed with smooth surfaces. It is especially clear at low shear rate, which is the source of large measurement errors on the yield stress value (figure 1.5). The amplitude of wall slip depends on the fluid and especially on short-range interactions between microscopic elements [25].

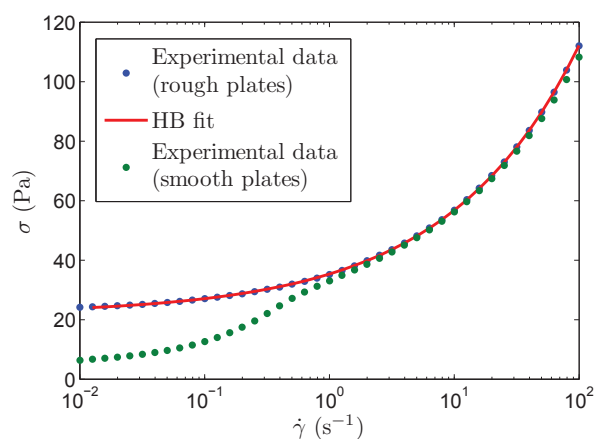


Figure 1.5 – Two flow curves illustrating the effect of wall slip: blue points are experimental data of 0.25% Ultrez10 Carbopol measured with rough plates (covered with sandpaper); green points are experimental data of the same Carbopol measured with smooth glass plates. It is obvious that the flow curve is not accurate when measured with smooth plates, especially under  $\dot{\gamma} < 1 \text{ s}^{-1}$ .

To solve this problem it is necessary to use rough walls for the rheometer measuring cell. The roughness size that best stops wall slip is of the same order as the typical size of the constitutive elements of the fluid (polymer balls, droplets...) [26].

### Transient response

When performing a startup experiment with some yield-stress fluids, the stress first grows quasi elastically with the deformation, then reaches a maximum and finally decreases towards its stationary value [27]. This phenomenon is called a stress overshoot. It is due to the finite time necessary for the material to fluidize after rest.

The final decrease follows a power law but the rheometer averages the stress values even

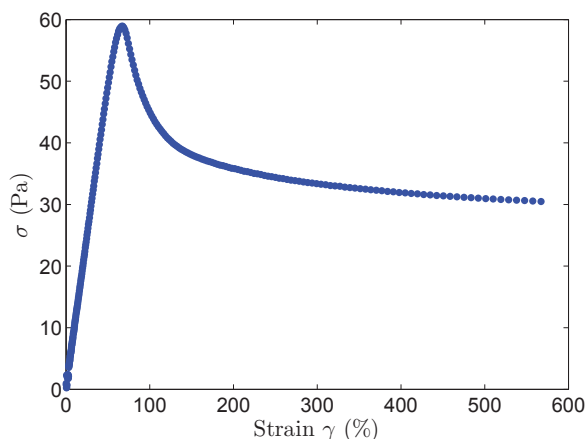


Figure 1.6 – Example of a stress overshoot during a startup experiment with 1 % ETD2050 Carbopol, at a constant shear rate of  $0.1 \text{ s}^{-1}$ .

though they always lie above the stationary value. Stress measurements obtained during an increasing succession of shear rate steps are therefore often overestimated. However, the relaxation to the stationary value is much faster after a decreasing step because the material is already fluidized. The flow curve is hence more reliable for a decreasing step succession.

## 1.2 Capillarity, static laws

Main reference: [28]

My thesis deals a lot with capillary experiments. I will thus present briefly the main elements of the theory of capillarity. Note that all the following definitions and laws apply to stable equilibrium states.

### 1.2.1 Definition of interfacial tension

Interfacial tension appears each time a fluid A (gas or liquid) comes in contact with a solid or a non-miscible fluid B. At the molecular level, contact between the particles of A and B is energetically more expensive than A-A or B-B contact. At the interface this contact cannot be avoided but it costs energy. This energy (per unit surface) is denoted  $\Gamma$  and is simply called interfacial tension or surface tension. It can be defined as the free energy increase for an infinitesimal surface area ( $A$ ) increase:

$$\Gamma = \left. \frac{\partial F}{\partial A} \right|_{T, V, \dots} \quad (1.1)$$

The word *tension* suggests a force. In fact this interfacial energy is at the origin of a tangential resisting force when an operator increases the area of the interface, which recalls an elastic surface. One can imagine a rectangular frame into which an operator creates and stretches a liquid film (see figure 1.7). Because of the surface energy, the system will resist this stretching with a force  $f = \frac{\partial F}{\partial x} = \frac{\partial F}{\partial A} \frac{\partial A}{\partial x} = \Gamma L$ . This is why surface tension is also often defined as a force per unit length.

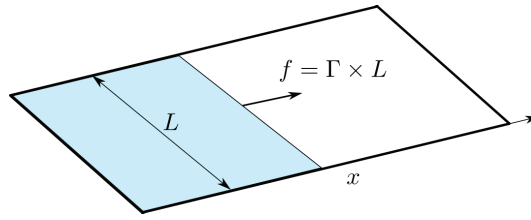


Figure 1.7 – Illustration of surface tension as a force per unit length. An operator extends the area of the liquid film and must apply the force  $f$  to keep the film at equilibrium.

However, the force  $f$  does not depend on the area increase  $\Delta A = L\Delta x$  but only on the frame width  $L$ , so it is not an elastic force, even if the comparison is tempting and sometimes helpful.

Liquid-air interfacial tension is responsible for the spheric shape of an isolated liquid drop or of a bubble. The volume of the liquid in the drop is fixed (it is considered incompressible) and the total surface energy must be minimum for the system to reach a thermodynamical equilibrium. The shape minimizing the surface at a fixed volume is a sphere.

## 1.2.2 Static wetting and Young's law

Generally  $\Gamma$  or the "surface tension" without any precision refers to the liquid-gas interfacial tension. Of course there also exist interfacial tensions between a solid and a gas (denoted  $\Gamma_{SG}$ ) and between a solid and a liquid ( $\Gamma_{SL}$ ).

When the system is composed of three different phases, as it is when a liquid drop comes in contact with a solid surface, all three kinds of interfaces exist. The spreading parameter  $S = \Gamma_{SG} - (\Gamma_{SL} + \Gamma)$  tells us if a thin uniform layer of liquid on the solid has a lower energy than a dry solid. If  $S \geq 0$  wetting will be total, and only partial if  $-2\Gamma < S < 0$ . If  $S < -2\Gamma$  no wetting is possible at all: the solid surface is superhydrophobic.

In the case of partial wetting, the three interfaces meet along a line called the "contact line" or "triple line". At this line the contact angle  $\theta_0$  between the liquid-air and the solid-liquid interfaces is given by Young's law (Figure 1.8a):

$$\Gamma \cos \theta_0 = \Gamma_{SG} - \Gamma_{SL} \quad (1.2)$$

This law is obtained by minimizing the total interfacial energy with the constraint of a fixed liquid volume. It is also possible to find it in a very simple way by a force balance (per unit length) between the horizontal components of the surface tension forces at the triple line. However the force formulation is of much more complexity and is still the subject of investigations. Concerning the vertical components of these forces, after years of debate, a consensus seems to rise: they are balanced by an imperceptible deformation of the rigid substrate. This is confirmed by experiments with soft elastic substrates [29].

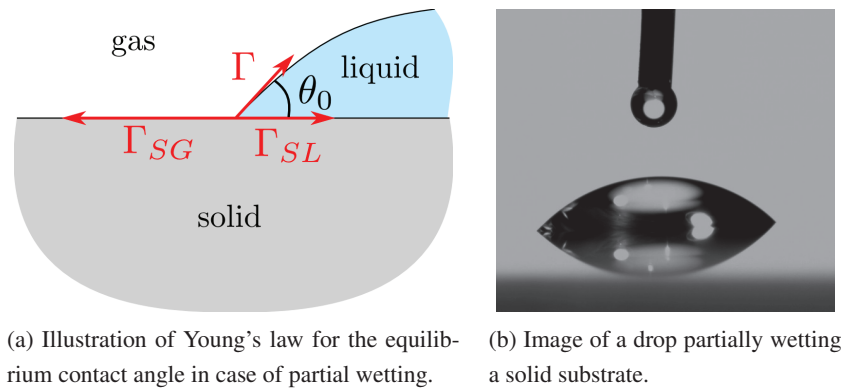


Figure 1.8 – Partial wetting.

### 1.2.3 Laplace's law and the shape of drops

Laplace's law states that when an interface is curved, a pressure difference  $\Delta p$  appears between the two phases:

$$\Delta p = \Gamma \left( \frac{1}{R} + \frac{1}{R'} \right) = \Gamma C \quad (1.3)$$

where  $R$  and  $R'$  are the (algebraic) curvature radii of the interface and  $C$  is its mean curvature.

An interesting consequence is that when gravity effects are not negligible, the curvature of the surface results from a balance between the Laplace pressure and the hydrostatic pressure. Thus the system curvature is not uniform but varies linearly with altitude. The local radius of the drop  $r(z)$  obeys Laplace's equation:

$$\frac{1/r}{(1+r'^2)^{1/2}} - \frac{r''}{(1+r'^2)^{3/2}} = C_0 - \frac{\rho g z}{\Gamma} \quad (1.4)$$

with  $C_0$  the mean curvature at  $z = 0$ .

This allows for surface tension measurements using the curvature variation with  $z$ : the pendent drop or the rising bubble methods (Figure 1.9).



Figure 1.9 – Picture of a pendent drop used to measure the surface tension of a liquid, after fitting the drop outline with a Laplacian profile.

### 1.2.4 Jurin's law and capillary rise

Jurin's law predicts the rise height of a liquid in a thin tube (a capillary) of radius  $R$ . If  $\Gamma_{SG} > \Gamma_{SL}$  wet walls cost less energy than dry walls, so the liquid rises in a vertical capillary. This energy gain is balanced by the gravitational potential energy of the liquid column, so that the liquid surface stabilizes at a height  $H$  given by:

$$H = \frac{\Gamma \cos \theta_0}{\rho g R / 2} \quad (1.5)$$

This equation is derived either from a free energy minimization, or from a pressure balance at the interface (hydrostatic pressure and Laplace pressure, given the curvature of the free meniscus), or even from a force balance (surface tension forces and gravity).

This is another method to measure  $\Gamma$ , provided  $\cos \theta_0$  is already known.

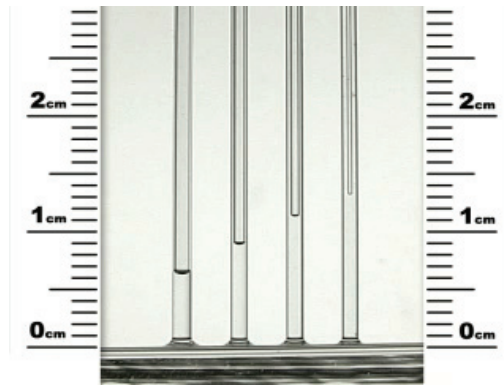


Figure 1.10 – Capillary rise in capillary tubes of different radii.

Jurin's law also holds for capillary cells of other shapes, such as thin rectangular cells. A nice experiment initially performed by B. Taylor in 1712 consists in a capillary rise in a cell made of two nearly parallel plates forming a wedge, so that the liquid surface follows a hyperbola (figure 1.11).

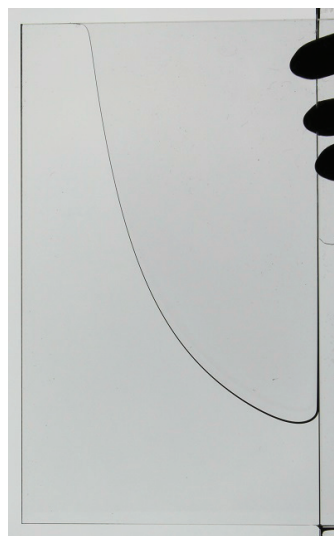


Figure 1.11 – Taylor experiment (capillary rise in a thin wedge) with a dilute NaOH solution.

## 1.3 Capillary dynamics

Now that the main equilibrium laws of capillarity have been recalled, I will present a few dynamic situations, still involving liquid interfaces and capillarity.

### 1.3.1 Moving contact lines and drop spreading

Main references: [30, Sec. 4.8][31, Sec. 1.4]

It happens that a contact line is forced to move, either because the system is not at equilibrium yet or because the liquid moves. Typical examples are a drop in which volume is injected continuously or a drop sliding on an inclined plane.

On a perfectly smooth and homogeneous surface, the speed of a contact line  $V$  is determined by a balance between the capillary force power (per unit length of line)  $P_c = \Gamma(\cos \theta_0 - \cos \theta)V$  and the viscous dissipation in the liquid wedge. To ensure this balance, the dynamic contact angle  $\theta$  can no longer be equal to the Young equilibrium value  $\theta_0$  (see 1.2.2). If the line is advancing,  $\theta > \theta_0$ , and if the line is receding,  $\theta < \theta_0$ .

Depending on the model used for the viscous dissipation in the wedge, there exist several relations between the line velocity  $V$  and the dynamic contact angle  $\theta$ . In all cases, the theory has to introduce cutoffs to avoid a flow singularity in the corner tip. For example, the Cox-Voinov relation states, if the angle remains small (i.e.  $\tan \theta \approx \theta$ ):

$$\theta^3 - \theta_0^3 = 9 \frac{\eta V}{\Gamma} \ln(L/a) \quad (1.6)$$

where  $L$  is a macroscopic cutoff (generally the size of the system) and  $a$  a microscopic cutoff (a few molecular radii).

A similar balance, combined with the geometric relation between  $\theta$  and the base radius  $R$  of a spherical cap shaped drop gives the so-called Tanner's law for spreading of small (to avoid gravity effects) completely wetting (so that  $\theta_0 = 0$ ) drops:

$$R(t) = (At)^{1/10} \quad (1.7)$$

with  $A \propto \frac{\gamma}{\eta \ln(L/a)} \left(\frac{4\Omega}{\pi}\right)^3$  [30].

This relation is valid at "long" time scales when the contact angle is small and there must be no inertial or gravity contribution.

In case of a large drop with a small contact angle but a strong contribution of gravity, the viscous dissipation balances the variation of potential energy. Given the geometrical constraints for a spherical cap, this regime is characterized by  $R(t) \sim t^{1/8}$ .

**First moments after contact.** At short time scales, that is of the order of a millisecond after contact, the contact line dynamics is mainly inertial [32]. The contact radius then evolves like the square root of time, with small variations when the fluid is very viscous [33]. This regime is supposed to be valid until the contact radius  $R$  becomes of the order of the initial drop radius  $R_0$ .

**Case of a shear-thinning fluid.** Tanner's law 1.7 was derived for simple fluids. There also exists a similar formula for shear-thinning fluids with a power law flow curve  $\sigma = K\dot{\gamma}^n$ . It is obtained either by a resolution of Navier-Stokes equations [10] or by a balance between the work of the spreading surface and the viscous dissipation near the line. For an axisymmetric drop, the calculation predicts that the radius grows as a power law of time, with an exponent  $p = \frac{n}{3n+7}$ . For a Newtonian liquid,  $n = 1$  and  $p = 1/10$  is recovered. For  $n = 0.5$  for example,  $p \approx 0.06$ .

The gravitational regime was also investigated in [10]. The exponent for this regime is  $p = \frac{n}{3n+5}$  instead of  $p = 1/8$  for simple fluids.

### 1.3.2 A few words on impacts

Main references: [34, 18]

A lot of work has been published on impacts of fluid drops onto a solid surface, in different cases: different fluid viscosities, different kinetic energies, different substrates (wetting, hydrophobic, hot, moving,...) [35], no substrate except a small target [36], non-Newtonian fluids [4, 37]...

In the most basic case of a simple fluid on a hard flat substrate, in the inertial limit, different behaviors were identified [38] depending on the kinetic energy of the drop, on the fluid nature and on the surface features (wettability, roughness). After a kinematic stage during which  $R \sim t^{1/2}$  the drop can for example simply spread, or splash, or even bounce.

The control parameters for these regimes are the Weber number  $We = \frac{\rho DV_0^2}{\Gamma}$  and the Reynolds number  $Re = \frac{\rho DV_0}{\eta}$ . When a combination of these dimensionless numbers,  $\mathcal{K} = We^{4/5} Re^{2/5}$ , is small, the drop spreads, possibly recedes a little before stabilizing at its final shape. When  $\mathcal{K}$  increases above a value close to 650, the drop starts to splash, i.e. to expel little satellite droplets. Bouncing is observed at high kinetic energy especially on non-wetting surfaces (hydrophobic).



Figure 1.12 – A water drop splashing on a hard surface.

**Impacts of yield-stress fluids.** The case of yield-stress fluids has been studied by Luu and Forterre [37, 39]. One of the specific properties of yield stress fluids is a nearly constant elasticity, both under and above the yield stress. Luu has shown that a drop of carbopol can retract strongly or bounce even after an extreme deformation under impact, because of this elasticity. She has built a model based on the elasto-visco-plastic rheology of carbopol to reproduce the experimental results. The principal physical ingredient of the model is a dimensionless number comparing the viscous relaxation time  $(K/G)^{1/n}$  (reminder:  $K$  is the consistency of the fluid,  $G$  the elastic modulus and  $n$  the HB exponent) to the period of the fundamental elastic vibration mode of the drop.

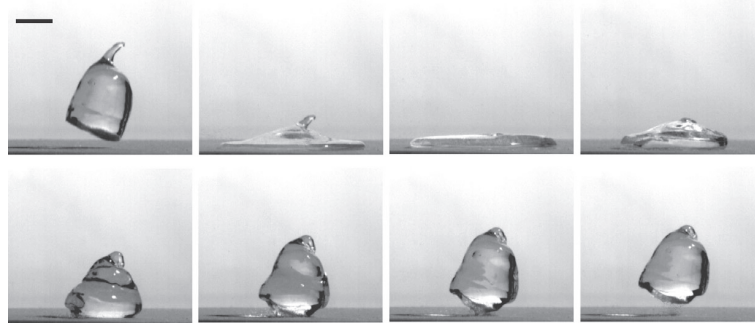


Figure 1.13 – From Luu’s thesis: bouncing of a 2 % carbopol drop on a super-hydrophobic surface (speed  $V_0 = 2.4 \text{ m s}^{-1}$ ). Time interval between the pictures is 8 ms. Scale bar is 10 mm.

### 1.3.3 Surface waves and fluctuations

Main reference: [30, Sec. 6.4]

When a free liquid surface fluctuates, two elements tend to oppose the level variation. First, gravitational energy increases where the surface level is above the average. Secondly, because of surface tension, a pressure difference appears when the interface is curved (see Laplace’s law in section 1.2.3). It can be seen also as an area increase (unfavorable) when the interface undulates.

When the perturbation is small, which means that the local slope of the surface is much less than 1 and that the non-linear terms in Navier-Stokes equation remain negligible, one can write a dispersion relation for surface waves:

$$\omega^2 = \left( gk + \frac{\Gamma k^3}{\rho} \right) \tanh(kh) \quad (1.8)$$

where  $g$  is the gravity amplitude,  $\rho$  the liquid density, and  $h$  the total height of the liquid layer. One can introduce the capillary length  $l_c = \sqrt{\Gamma/\rho g}$  (of the order of 3 mm for pure water) and write

$$c^2 = \frac{g}{k} \tanh(kh) (1 + k^2 l_c^2) \quad (1.9)$$

In a very thin layer of liquid or at very low frequency ( $kh \ll 1$ ) the hyperbolic tangent cannot be neglected, but as soon as  $h$  is greater than the wavelength  $\lambda$  this factor is close to 1. This limit is called the deep liquid limit.

From this equation, two limiting regimes (in a "deep" liquid bath) can be distinguished. When the frequency is low and  $\lambda \gg 2\pi l_c$  the phase velocity of the waves is  $c = \sqrt{\frac{g}{k}}$ . In this regime the major flattening ingredient is gravity. In a high frequency regime with  $\lambda \ll 2\pi l_c$ ,  $c = \sqrt{\frac{\Gamma k}{g}}$  and this major ingredient is surface tension. These waves are called gravito-capillary waves.

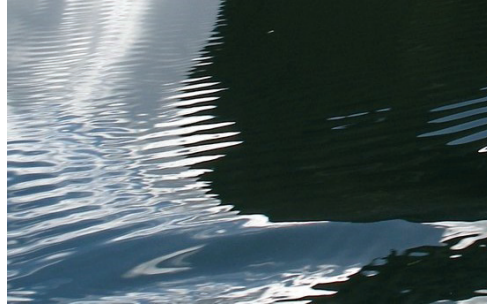


Figure 1.14 – Surface waves on water. Depending on the image scale, the small ripples could be capillary waves, and the large undulation at the bottom a gravity wave.

This model does not take into account viscous dissipation, but other more refined (although approximate) models exist and compute the wave amplitude attenuation from viscosity, especially when dissipation is linear with wave energy [40, 41].

In the case of a thermally excited surface, small fluctuations can be observed at the micron scale [42]. Analysis of the frequency spectrum of these fluctuations can give information on the viscoelasticity of the fluid [43]. In the 1980's the surface fluctuations were measured by a light scattering method. More recently, a new technique using specular reflection of a laser beam on the surface was developed [44]. It gives access to the viscoelastic moduli of complex fluids and soft solids on a very wide range of frequencies (up to 5 decades) [45]. The main limitation of this technique is that the surface tension must be measured separately.

### 1.3.4 Instabilities due to surface tension

Main reference: [28, Chap. 5]

Because a liquid layer of given volume has a smaller interface when splitting in multiple spherical droplets, surface tension can give rise to instabilities. One of the best known instabilities is the Plateau-Rayleigh instability, causing the destabilization of a liquid cylinder in drops. This is often encountered on wet fibers, such as spider webs in the morning dew for example.

The Rayleigh-Taylor instability is another kind of capillary instability, and it is seen when a sheet of liquid lying under a horizontal surface breaks in a lattice of pending drops. This instability is an example of a competition between gravity and surface tension which have contrary effects.

Such instabilities are also observed in beams of very soft elastic solids [46].

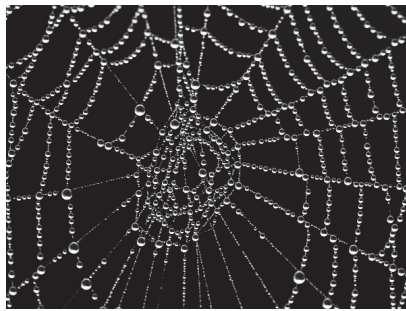


Figure 1.15 – Spider web covered with droplets of morning dew.



## Chapter 2

# Wetting with friction: contact angle hysteresis and yield-stress fluids

### Contents

---

<b>2.1</b>	<b>The friction family</b> . . . . .	<b>42</b>
2.1.1	What characterizes friction? . . . . .	42
2.1.2	Friction of the triple line . . . . .	43
	Contact angle hysteresis . . . . .	43
	Origin and relation with friction . . . . .	44
2.1.3	Yield stress . . . . .	45
<b>2.2</b>	<b>Contact angle hysteresis consequences</b> . . . . .	<b>45</b>
2.2.1	Sliding drops . . . . .	45
2.2.2	Evaporation . . . . .	46
2.2.3	Tubes and pores . . . . .	46
<b>2.3</b>	<b>Yield stress and capillarity</b> . . . . .	<b>47</b>
2.3.1	Laplace's law and the shape of drops . . . . .	47
2.3.2	Filament breakup and dripping . . . . .	48
2.3.3	Coating and films . . . . .	48
2.3.4	Capillary rise . . . . .	48
2.3.5	Measurement of surface tension . . . . .	49
<b>2.4</b>	<b>Conclusion</b> . . . . .	<b>51</b>

---

This chapter has two main goals: first, to explain the similitude between different frictional systems; secondly, to describe a number of experiments where friction has a sensible influence on capillary phenomena. This way I want to explain and develop the problematic I presented in the introduction: why is wetting of yield-stress fluids so special? Indeed, the fact that a kind of friction traps a system in a metastable state and prevents it to reach the global equilibrium is the central issue in wetting problems, because the laws of capillarity are valid at equilibrium.

## 2.1 The friction family

### 2.1.1 What characterizes friction?

First it seems necessary to clarify the concept of friction. Let us start with a general definition:

“Whenever one body moves tangentially against another, there is resistance to that motion. The resistance is called friction and the resisting force is the friction force.” (F. E. Kennedy, Jr., *Friction* in R. G. Lerner & G. L. Trigg, *Encyclopedia of Physics* [47])

Following this definition, friction exists each time some force resists a tangential motion. Of course this includes the motion of a solid on another one, but also for example of a fluid on a solid. Generally dry friction (typically between non lubricated solids) is distinguished from fluid friction (resulting from the fluid viscosity).

The first and most intuitive case of friction is dry solid friction. In solid mechanics, phenomenological models on friction appeared early, probably because nearly no realistic situation could be predicted without it. Indeed, without friction, it would be impossible to walk, to put a vehicle in motion, to assemble an object with screws, to keep an object still on a slightly tilted plane. . . Coulomb’s laws for friction are now widely used to faithfully reproduce these behaviors with equations. In brief, they state that [48]:

- the normal reaction force  $N$  between the two solid bodies is repulsive (it resists penetration),
- if the solids have no relative motion at the place of contact, the tangential force value is below a quantity equal to  $\mu_s N$  where  $\mu_s$  (the static friction coefficient) depends only on the material’s nature and surface,
- if there is a tangential motion between the solids, the tangential force value is equal to  $\mu_d N$ , where  $\mu_d$  (the dynamic friction coefficient) also depends only on the materials nature and surface, but is always less than  $\mu_s$ .

The microscopic condition of friction is a rough energy landscape, defined along an effective abscissa corresponding to the relative position of the two bodies. The roughness amplitude must be larger than thermal energy. The system can therefore be trapped in one of the many possible metastable states. Only an external driving force larger than a critical value can move the system out of the trap.

Fluid friction is a bit different. A tangential force resisting motion also arises from the fluid viscosity, for example when a body moves inside a simple fluid bath, but in contrast with dry friction, this force vanishes when the motion stops. Therefore I will not dwell on this case.

However, if we consider fluid systems (possibly composed of liquid and gas if there is an interface) sliding along a solid surface, we can think of other cases very similar to dry friction:

1. a triple contact line moving tangentially to a solid surface experiences a non-conservative force (in addition to viscous dissipation) at the origin of contact angle hysteresis,
2. a yield-stress fluid partly slips against a smooth wall, probably because the stress at the wall is above a critical value comparable to  $\mu_s N$  in Coulomb's laws,
3. in the same spirit, two layers of a sheared yield-stress fluid move with respect to each other if the shear stress is above a critical value.

In all these cases, described in more details below, one can argue that the tangential stress at the wall depends on the motion velocity, although in Coulomb's law, the friction force does not. This feature could be due to the fluid viscosity. But the important point here is that for dry friction between solids as well as for the three situations enumerated above, there is no motion under a critical value of the force, depending on the properties of the surfaces in contact.

### 2.1.2 Friction of the triple line

#### Contact angle hysteresis

We have seen in section 1.2.2 that one can compute the theoretical equilibrium contact angle from the knowledge of the three interfacial tensions at play at the level of a triple line. It means that, given a liquid and a solid surface in a given atmosphere, this angle can take only one value,  $\theta_0$  (called Young angle or equilibrium angle).

But the reality is, as usual, more complicated. Even if the triple line does not move, the contact angle rarely takes its equilibrium value. It lies somewhere between two extreme values: the receding contact angle  $\theta_r$ , below which the line is forced to recede, and the advancing contact angle  $\theta_a$ , above which the line is forced to advance. Actually, in most cases, we do not even know how to measure  $\theta_0$  because it is not possible to distinguish it from all other possible contact angle values.

A typical situation is this of a drop on an inclined plane (such as a car front glass under the rain). Based on Young's law, there is no reason for the drop not to slide downwards. But generally, if one progressively tilts the plane, at first the drop contact line will be stuck, the drop's shape will change (see figure 2.1) and the contact angle will take continuous values between two extrema situated respectively at the front and at the back of the drop. For a precise tilt value, the line will start to move. The contact angle at this moment is the advancing one (at the front) or the receding one (at the back).

Another simple way to illustrate this phenomenon consists in injecting liquid in a drop lying on a solid surface. Let us suppose that at the beginning of the experiment the contact angle is

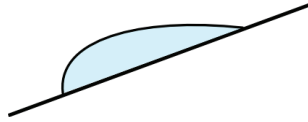


Figure 2.1 – Schematic profile of a drop sliding on an inclined plane.

intermediate between  $\theta_r$  and  $\theta_a$ . At first the line is pinned, the contact radius is constant, and the contact angle grows. When  $\theta$  reaches  $\theta_a$ , the line starts to advance and the radius increases. Then the flow in the syringe is reversed and the liquid is sucked up from the drop. The radius stays constant and the angle decreases until  $\theta = \theta_r$  where the line starts to recede. If we plot the contact angle as a function of the drop volume, we get an hysteresis cycle (figure 2.2). This is why this phenomenon is called **contact angle hysteresis (CAH)**.

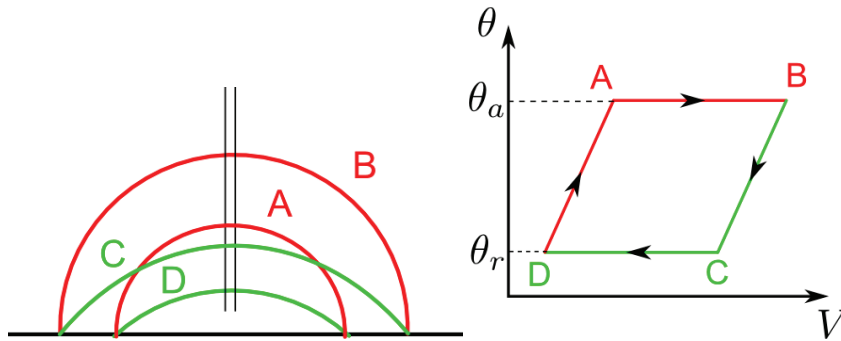


Figure 2.2 – Illustration of contact angle hysteresis: experiment and resulting hysteresis cycle.

### Origin and relation with friction

Physicists have long been very interested in CAH, because it happens everywhere as soon as a liquid wets a solid and it has crucial practical consequences. Several issues need to be clarified: how can we measure the equilibrium contact angle  $\theta_0$  if it cannot be observed? Which parameters can control CAH? What are its effects on wetting dynamics, on adhesion? All these questions are still debated. Nevertheless, everybody seems to agree on the fact that the origin of CAH is the surface heterogeneity (chemical defects) or roughness (physical defects).

The first models on CAH were developed simultaneously by Joanny and de Gennes [49] and Pomeau and Vannimendus [50]. They based their theories on the idea, already quite widespread at this time, that microscopic heterogeneities of the solid interfacial tensions were the source of small energy barriers for the triple line. Indeed the deformation of the liquid-gas interface close to the line is at the origin of an effective elasticity. The deformation of the line is thus energetically unfavorable. The line is then trapped in metastable states which do not obey directly Young's equation. In the case of rare defects, the relation between the advancing angle  $\theta_a$  and the receding angle  $\theta_r$  is linked to the density of defects  $n$  and to the energy  $W_d$  dissipated per defect during a whole hysteresis cycle, following the equation [51]:

$$\Gamma(\cos \theta_r - \cos \theta_a) = nW_d \quad (2.1)$$

where  $\Gamma$  is the surface tension of the fluid.

Since then, a lot of work has been published on experiments [52, 53, 54, 55, 56, 57] and more refined models [58, 59, 60, 61]. There is also some debate on whether the contact angle (and its hysteresis) depends on the whole contact surface energy or only on the part of the surface in contact with the line [62, 63].

Some models include a new ingredient: the line tension [64, 65, 66] initially proposed by Gibbs. It is thought as an excess free energy per unit length of contact line, and is supposed to have an influence on the contact angle of small sessile drops. However, even if this concept is found in several papers dealing with wetting, the value of the line tension itself is very uncertain and discussed [67, 68]. It is predicted to be very small, of the order of  $10^{-11}$  J/m, but much higher values have been measured experimentally, and many also report negative values (see the review by Amirfazli and Neumann [67]).

But whatever the cause of the line energy (effective elasticity or line tension), the surface defects cause the pinning of the line below a critical tangential force (per unit line length) and a friction force related to depinning avalanches above the critical force [54].

### 2.1.3 Yield stress

As explained in chapter 1, yield-stress fluids are able to flow only if the stress is above a critical value  $\sigma_y$ , called yield stress. Under that stress, they behave as an elastic solid, with some plasticity. Above that stress, their viscosity decreases as the strain rate increases. Moreover, at rest, yield-stress fluids include internal stress with a magnitude comprised between 0 and  $\sigma_y$ , governed by the flow history. This behavior is strongly reminiscent of solid friction, and also of line pinning in contact angle hysteresis. In particular, while the yield-stress fluid system is at rest, the exact stress field is unknown, and we can only tell that it is below  $\sigma_y$ .

The comparison between the yielding transition and the depinning transition has already been made in the past [69]. It has been shown that even if they share some similarities, they are slightly different [70]. In particular, the interaction kernel connecting the plastic or depinning events near the threshold is different in terms of range and geometry. Nevertheless, the macroscopic effects of yield stress, line pinning and solid friction are very similar.

## 2.2 Contact angle hysteresis consequences

Contact angle hysteresis is hardly avoided in real life and it is still difficult to control. It can be either desired or unwanted. Let us mention a few of the many consequences of CAH.

### 2.2.1 Sliding drops

In everyday life we are surrounded by problems implying sliding drops with hysteresis. In particular, the high CAH of water on most surfaces ( $\sim 30^\circ$  on normal untreated glass) makes them difficult to dry by simply expelling the drops. If there was no CAH, it would be enough to tilt a surface to see the water drops slide quickly and go. Actually, the only surfaces where CAH is

negligible are completely wetting surfaces (which are rare in real life because highly clean) or superhydrophobic surfaces (which are also rare because they are nano- or micro-patterned). Note that since recently, commercial chemical coatings, available in sprays, allow to make textiles superhydrophobic (for example: Ultra-Ever Dry, NeverWet).

This is an important concern in the textile industry, to create modern waterproof clothes for example. The problem is that it is also difficult to wash a superhydrophobic surface, because it precisely cannot be wet. CAH issues can also be interesting for surfaces that must remain transparent: glasses, car glass. . . More specifically, in surface sciences, CAH is an obstacle to the measurement of surface interactions through contact angle measurements. We can also imagine that in agriculture, for example, CAH can help to keep water or crop protection products on the plants and avoid chemicals to fall into the ground.

### 2.2.2 Evaporation

We just have talked about the problem of drying a surface by pushing the water out. Evaporating the liquid is not always a better solution, because CAH causes the “coffee stain effect”. This phenomenon happens when a drop containing ions or solid particles evaporates [71]. Due to CAH, the line is pinned until the contact angle reaches  $\theta_r$ . The particles concentrate along the contact line, so they tend to settle at the periphery of the drop, which creates a ring of particles.

Because of the coffee stain effect, evaporating water drops leave residual rings of minerals on surfaces (this is why you wipe plates and glasses with a towel when you want them to be shiny). It is also a nuisance when trying to deposit an homogeneous layer of particles on a substrate from a suspension.

### 2.2.3 Tubes and pores

When a liquid flows in a tube with diameter comparable to the liquid capillary length ( $l_c = \sqrt{\rho g / \Gamma}$ ) or smaller, capillary effects become predominant. Because of CAH, isolated portions of fluid can be stuck in the tube because they are not heavy enough to overcome asymmetric capillary forces (see figure 2.3):

$$W < 2\pi R\Gamma(\cos\theta_r - \cos\theta_a) \quad (2.2)$$

where  $W$  is the weight of the liquid column and  $R$  the radius of the tube.

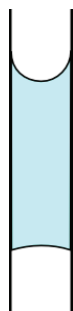


Figure 2.3 – Drop stuck in a thin tube because of CAH.

The same reasoning is valid if the operator applies a pressure difference  $\Delta p$  on the tube, if  $\pi R^2 \Delta p$  is smaller than the capillary force written above. This is why it can be difficult to empty a tube full of liquid when there are too many air bubbles. This effect is particularly important if  $R$  is small. For a given surface-liquid pair, the pressure difference necessary to put the liquid in motion scales as  $1/R$ . It can cost a huge energy loss, for example when pushing liquid into a porous material.

## 2.3 Yield stress and capillarity

The yield stress, comparable to a friction threshold, has important consequences on capillary phenomena, because the shape of the system cannot reach the state predicted by classical capillary laws, due to the residual internal stress.

### 2.3.1 Laplace's law and the shape of drops

The shape of a drop of fluid in a gravity field is usually governed by Laplace's equation (equation 1.4 of chapter 1). This equation is true if the fluid has no yield stress, because in this case the internal shear stress relaxes to zero everywhere and the remaining stress is pure hydrostatic pressure. But in a drop of yield-stress fluid, non-zero stress always remain, even at rest, with a non-trivial geometry resulting from previous deformation, and it never relaxes. However the magnitude of the residual stress is always less than the yield stress  $\sigma_y$ .

This explains why yield-stress fluid systems often have complex shapes and can be easily distinguished from other fluid systems even in absence of flow. An example is shown in figure 2.4.

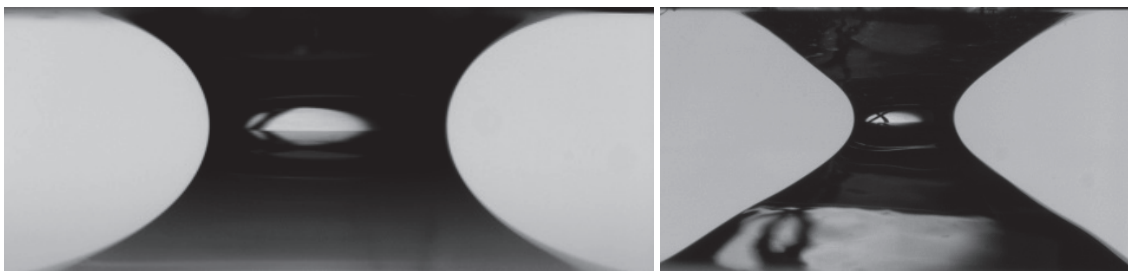


Figure 2.4 – Two pictures of capillary bridges with comparable dimensions ( $\sim 1$  mm), after axial stretching: on the left, the fluid is silicone oil (simple fluid) and on the right it is carbopol with a yield stress  $\sigma_y \approx 17$  Pa. The shapes are visually very different. In particular the carbopol bridge has a characteristic hourglass shape.

An extended version of Laplace's law still applies, replacing  $\Delta p \vec{n}$  with the total stress at the surface. However the stress field is generally unknown in the system. For this reason, the curvature cannot be compared to any known physical quantity (such as gravity, in the case of simple fluids), which prevents the experimentalist from drawing conclusions on the surface tension from a pendent drop (or rising bubble) measurement. Likewise, it is very difficult to predict the shape of a bubble in a bath of yield-stress fluid [72], except in very specific geometries where the shear stress can be computed at any time and any point.

### 2.3.2 Filament breakup and dripping

In the most simple case, the breakup of liquid jets of simple fluids is the result of an equilibrium between inertia and surface tension. A liquid cylinder of radius  $r$  is destabilized by a Plateau-Rayleigh instability and breaks in drops on a timescale  $t = \sqrt{r^3 \rho / \Gamma}$  [73]. However this is a result from a linear analysis, and it cannot explain the formation of small satellite drops, described for example in [74]. This issue was tackled theoretically for inviscid and viscous fluids [75]. The outer medium viscosity can also play a role and damp the instability dynamics [76].

On the other hand, viscoelastic fluids are known to resist capillary breakup and form long filaments because of non-linear elastic effects [77, 78]. This allowed the design of filament-stretching rheometers [79, 80].

The case of yield-stress fluids has been considered for about a decade. Coussot and Gaulard [81] first studied the size of drops when varying the flow rate, after having noticed that even if surface tension is expected to be negligible with respect to viscous effects, poured yield-stress fluids tend to form large drops. Then the dripping of yield-stress fluids drops was also studied by several groups. In particular, Balmforth *et al.* [82, 83] developed a model for the dynamics of a filament of a Herschel-Bulkley fluid. German and Bertola [2, 84] performed experiments with falling drops and noticed a transition between a capillary breakup at low yield stress and a plastic breakup at high yield stress. Niedzwiedz *et al.* [15] studied the extensional rheology of emulsions.

These works highlight that the yield stress can strongly modify the behavior of free-surface flows, generally governed by surface tension.

### 2.3.3 Coating and films

When a solid is withdrawn from a liquid bath, a thin layer of fluid remains on the surface. The thickness of this layer is usually described by the Landau-Levich-Derjaguin theory [28, 85]. The main ingredients are the capillary length  $l_c = \sqrt{\rho g / \Gamma}$  and the capillary number  $Ca = \eta V / \Gamma$  (with  $\eta$  the fluid viscosity).

This problem is really interesting for industry, where many objects are coated by dipping into a bath of fluid (dip-coating). However, the fluids used are very often complex (paint or liquid chocolate for example). Maillard worked with Coussot on the coating of surfaces with yield-stress fluids, either by dip-coating or by spreading with a blade [86]. They showed that the thickness of the fluid layer depends on the yield stress instead of the capillary number [87].

### 2.3.4 Capillary rise

For simple fluids, or complex fluids without a yield stress, the height reached by the liquid in a vertical tube is predicted by Jurin's law, introduced in chapter 1. The physical ingredients that come into play here are surface tension and gravity.

With a yield-stress fluid, the yield stress also has an influence, as shown by Bertola [17] and Géraud [6, 11]. Indeed, the fluid is sheared during its ascension. When it stops progressively, the stress decreases but remains just above the yield stress in the sheared regions. At the end, the

stress at the channel walls is equal to  $\sigma_y$ . This is at the origin of a supplementary force opposing the capillary force  $\Gamma \cos \theta$ . Then, the modified Jurin's law can be written as:

$$H = \frac{\Gamma \cos \theta}{\sigma_y + \rho g e / 2} \quad (2.3)$$

with  $H$  the final height of the liquid column and  $e$  the channel width.

Thus, a yield stress fluid always rises lower than a fluid without yield stress, for the same surface tension. Moreover, the final height decreases when the yield stress increases.

Interestingly, Géraud *et al.* [11] emphasized the importance of the fluid history: the final height varies slightly, on a scale corresponding to the gap  $e$ . This induces an uncertainty on the capillary force  $\Gamma \cos \theta$  of the order of  $\sigma_y e$ . They explained that this was due to the random stress distribution in the reservoir at the bottom of the channel, resulting from the way the reservoir was filled. Thus both the top meniscus and the bottom reservoir are important.

### 2.3.5 Measurement of surface tension

As explained above, yield stress effects and frozen elastic stress contribute in a complex manner in surface effects, otherwise ruled by the only surface tension. As a side effect, it gets very difficult to estimate this quantity of interest, useful either for industrial applications (coating, droplets) or to check models where capillarity plays a role (filament breakup or bubble shape for example).

Several teams have studied the dependence of the surface tension of polymer solutions (among which carbopol) with concentration, with very variable methods and results [12, 13, 14], and other teams use values with few details on the measurement procedure [17, 2, 15]. The carbopol solutions are sometimes neutralized, which means that they have a yield stress (see chapter 3).

Hartnett's group have measured the surface tension of different polymer solutions and in particular of carbopol. In the paper by Hu *et al.* [12], they report measurements by the maximum pressure difference method. Their carbopol solutions are neutralized and the flow curves (viscosity versus shear rate) seem to show a yield stress. However the  $\sigma_y$  values are not given. They do not take into account the yield stress in their theory, and find surprisingly high surface tension values for the most viscous gel (sensibly higher than pure water surface tension). They also find that carbopol surface tension is equal to the one of pure water. In a second article, by Ishiguro and Hartnett [13], the authors use a capillary rise method with the original Jurin's law, and still obtain surprising results. For example, the surface tension of carbopol is perfectly constant with concentration and equal to pure water surface tension, although it was shown later [17, 11] that yield stress has a strong effect on capillary rise. An hypothesis could be that the concentrations were too low to get a yield stress high enough to influence the results.

Manglik *et al.* [14] have also measured the surface tension of polymer solutions, including carbopol, by a maximum bubble pressure difference method, and they have found that  $\Gamma$  decreases as the concentration increases (figure 2.5), which seems more natural, but no mention is made of the existence of a yield stress or of neutralization of carbopol solutions in their paper.

In the absence of a reliable method to measure the surface tension of yield-stress fluids, most people have then assumed a rough value for their models, or they have measured it anyway,

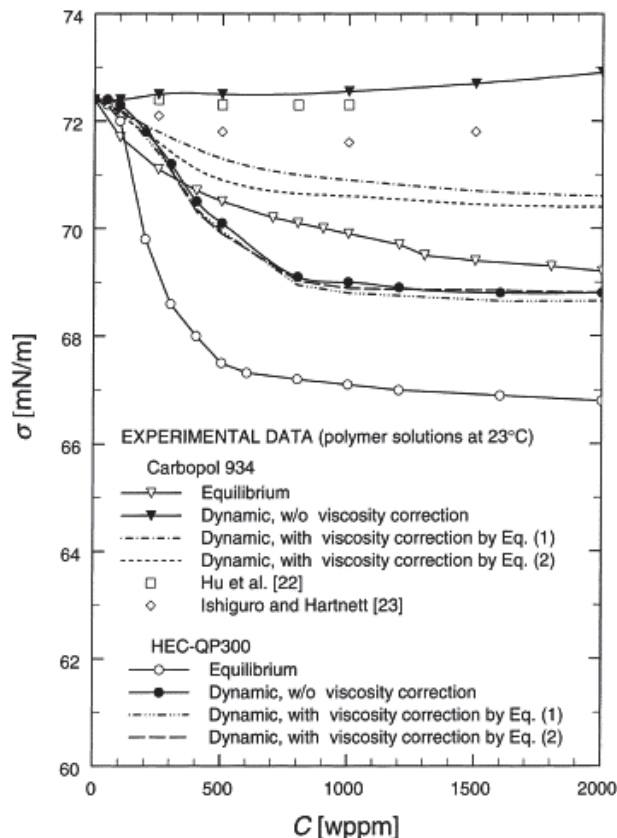


Figure 2.5 – Figure taken from Manglik *et al.* [14]. The empty inverted triangles are equilibrium surface tension measurements on Carbopol 934 solutions. The solutions are not neutralized so they have no or very little yield stress. The surface tension (denoted  $\sigma$ ) decreases with polymer concentration  $C$ .

generally with a Du Nouÿ ring method. Contrary to what is sometimes claimed, this method has no reason to give more reliable values of surface tension with yield-stress fluids.

Recently, Boujlel and Coussot have tackled seriously the problem of measuring the surface tension of yield-stress fluids where the viscous stress never vanishes, however slow can the experiment be performed [1]. They have used a plate withdrawal method on carbopol microgels and computed a theoretical correction for the viscous stress. The correction agrees qualitatively with the experimental results for many carbopol concentrations and plate thicknesses. More precisely, the model predicts an apparent surface tension  $f = \Gamma + (1 + Gr)E\sigma_y$  with  $\Gamma$  the true surface tension,  $Gr$  a number to account for gravity effects,  $E$  the thickness of the blade and  $\sigma_y$  the yield stress of the fluid. The experimental results best correspond to  $f = \Gamma + (3 + Gr)E\sigma_y$ , but the difference could not be explained.

From this literature we see that measuring the surface tension of yield-stress fluids is not trivial. No method seems to be able to give a reliable value of  $\Gamma$ , except at vanishing yield stress, ironically. We might as well say that we still do not know how to measure the surface tension of yield-stress fluids in the general case. However, in some precise geometries, simple enough for the stress field to be known everywhere, we expect to be able to compute a correction to the apparent surface tension. Here we propose an experimental method to measure the surface tension

of yield-stress fluids, where we do not even need to compute an exact correction (chapter 4).

## 2.4 Conclusion

In this chapter, I have explained why yield stress and contact angle hysteresis are similar to solid friction. I have used the characteristic features of solid friction to define a “friction family”: within that family, an effective tangential force resists motion, and it has a finite and unknown value when the system is at rest. The friction family gathers out-of-equilibrium systems trapped in a metastable state by microscopic mechanical interactions. For this reason, capillary experiments and measurements are delicate when dealing with friction, because the usual laws assume an equilibrium state.

It is difficult to formulate general rules to account for the competition between surface tension and friction forces, such as the yield stress. I believe that a dimensionless number is a too naive rule. It just gives a raw idea of the importance of friction effects with respect to capillary effects. It is more accurate to estimate the force magnitude and direction at the interface, keeping in mind that the motion history matters a lot.



# Chapter 3

## Carbopol: rheology and structure

### Contents

---

<b>3.1</b>	<b>Preparation . . . . .</b>	<b>54</b>
<b>3.2</b>	<b>Rheology . . . . .</b>	<b>54</b>
3.2.1	Characterization of the samples . . . . .	54
3.2.2	Dynamics around the yielding . . . . .	56
	Startup experiments . . . . .	56
	Response to strain steps . . . . .	57
<b>3.3</b>	<b>Microstructure . . . . .</b>	<b>60</b>
3.3.1	Measurement protocol . . . . .	60
3.3.2	Results . . . . .	65
3.3.3	Perspectives . . . . .	67

---

As a model yield-stress fluid, I used a water-based polymer microgel, composed of a commercial polymer swelled in water. The polymer is Carbopol from Lubrizol, made of crosslinked polyacrylic acid (or PAA). Different types of Carbopol are available. They differ by some additives or chemical functionalization used to modify the interactions. I used two types: ETD 2050 (“easy-to-disperse”) and Ultrez 10. They are denoted ETD and U10 in the following. Although Carbopol is the commercial name of the polymer itself, in the text I will often write “carbopol” to refer to the microgel.

### 3.1 Preparation

The microgel is prepared as follows: a small amount (of the order of 1% in weight) of polymer powder is weighted and slowly dissolved in deionized water heated at 50 °C and stirred. The hot solution is stirred for 30 minutes, then it is let to cool down to room temperature. Evaporation is hindered by covering the container with Parafilm. The solution is acid after complete dissolution. Then sodium hydroxyde (10 M) is added to the solution until its pH is raised to  $7 \pm 0.5$ . The adequate quantity of NaOH is about 1  $\mu$ L for each mg of carbopol powder. The pH neutralization causes the polymer chains to charge negatively. The charged chains thus repel each other, the polymer blobs swell and jam, and the solution becomes a microgel. Finally the microgel is either stirred gently by hand or stirred for 24 hours at 2100 rpm with a mechanic stirrer. It was indeed shown in previous works [88] that stirring changes the rheology of carbopol. In my work the carbopol concentrations range from 0.25% (in weight) to 2%. Hand stirred (respectively machine stirred) carbopol is denoted HS (respectively MS) in the following.

### 3.2 Rheology

#### 3.2.1 Characterization of the samples

Carbopol microgels are generally considered as model, non thixotropic, yield-stress fluids. As long as slip [24], transient shear banding [20] and confinement [21] are avoided, their flow curve is well fitted with a Herschel-Bulkley (HB) law:

$$\begin{cases} \dot{\gamma} = 0 & \text{if } \sigma < \sigma_y \\ \sigma = \sigma_y + K \dot{\gamma}^n & \text{if } \sigma \geq \sigma_y \end{cases}$$

with  $\sigma_y$  the yield stress,  $K$  the consistency and  $n$  the HB exponent.

Our rheometer is a controlled-stress Anton Paar MCR 301. Unless stated otherwise the flow curves are measured with a homemade rough cone and plate geometry of radius 25 mm and angle 4°. Both the cone and the plate are made of PMMA sandblasted to obtain a surface roughness of about 20  $\mu$ m. A parallel plates geometry is easier to made rough, with sandpaper, but it has the considerable drawback of imposing an inhomogeneous shear to the sample. We have checked that the flow curves are the same as the ones obtained with a rougher parallel plates geometry (sandpaper of roughness 50  $\mu$ m).

The flow curve is obtained with decreasing steps of constant shear rate, ranging from  $100 \text{ s}^{-1}$  to  $0.01 \text{ s}^{-1}$  (10 points per decade). The duration of each step is set automatically by the rheometer (between 15 s and 30 s per step) and the measurement is made when the steady state is reached. With our rough geometry, wall slip only occurs at very low shear rate ( $\dot{\gamma} < 0.1 \text{ s}^{-1}$ ). The points where wall slip can be seen are removed from the data before the fit. Figure 3.1 shows an example of an experimental flow curve fitted with a HB law. The green points are supposed to be affected by wall slip and have not been taken into account for the fit. Only the points where wall slip is visually obvious, thanks to a kink in the flow curve, are removed. If we remove too many points at low shear rate, the precision on the yield stress is affected, hence the importance of a rough geometry to reduce wall slip. Nevertheless, the uncertainty on the yield stress can reach 1 Pa even in the absence of wall slip. This is due to several causes, among which the variations of the excess of fluid at the edge of the cone or slow transient effects preventing the fluid to completely reach the steady state at low shear rate.

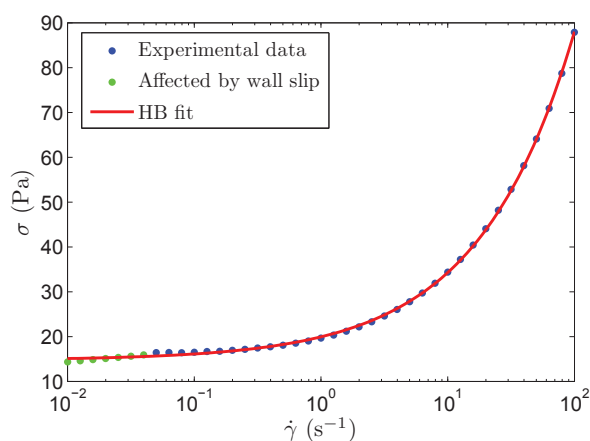


Figure 3.1 – Experimental flow curve of ETD 1% MS carbopol. The green points are not taken into account in the fit. From the fit  $\sigma_y = 15 \text{ Pa}$ ,  $K = 5.2 \text{ Pa s}^n$  and  $n = 0.57$ .

The viscoelastic moduli  $G'$  and  $G''$  are measured by oscillatory shear deformation of 1% or less with increasing, then decreasing frequencies, ranging from 0.1 Hz to 50 Hz. At low frequency (below a few Hz) the storage modulus  $G'$  is nearly constant and the loss modulus  $G''$  increases as the square root of frequency. Moreover  $G'$  is much greater than  $G''$ , which means that in this regime, carbopol is mainly an elastic solid. Above 10 Hz the data are not very reliable, both because our rheometer is not designed for high frequencies, and because high frequencies seem to modify the rheology of the microgel.

Interestingly the amplitude of  $G''$  at a given frequency varies with polymer concentration but not with stirring whereas  $G'$  strongly changes with concentration and stirring. An example of measurement of viscoelastic moduli for two carbopols of different stirrings is shown in figure 3.2. In the following, what I denote  $G$  is  $G'$  at 0.1 Hz.

The flow parameters (yield stress, consistency, viscoelastic moduli) vary from a batch to another whereas the HB exponent  $n$  is fairly reproducible for carbopols of same type and stirring. There can be many origins of this dispersion. For example, the atmospheric temperature

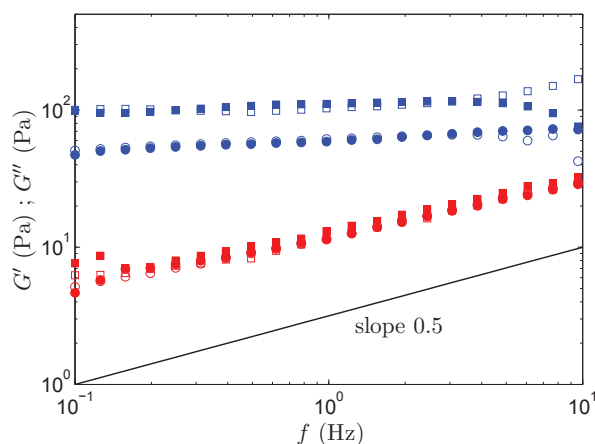


Figure 3.2 – Experimental viscoelastic moduli  $G'$  (blue symbols) and  $G''$  (red symbols) of two ETD 1% carbopols: MS (circles) and HS (squares). The solid symbols are for increasing frequencies and the empty symbols for decreasing frequencies. The black line represents a 0.5 power law.

seems to have an influence on all the parameters. It is therefore not possible to give a systematic correspondence between polymer concentration and yield stress, for example. However, for each experiment these parameters were noted down. Every time I present results with carbopol I mention at least the yield stress of the microgel used. Additionally, the reader can find in annex A the complete list of the carbopols used in the experiments and of their rheological parameters.

To give an idea of the orders of magnitude, the yield stress of all our samples ranges from 0.5 Pa to 40 Pa,  $K$  is between  $0.8 \text{ Pa s}^n$  and  $14 \text{ Pa s}^n$  and  $n$  varies between 0.4 and 0.6.  $G$  is of the order of 3 times the yield stress for ETD-MS carbopol samples and up to 9 times the yield stress for ETD-HS or U10 carbopol samples.

### 3.2.2 Dynamics around the yielding

The Herschel-Bulkley model only describes the flow in a steady state. At the other extreme, the viscoelastic moduli are measured by small (linear) oscillatory deformation. None of these methods gives us information on what happens near the yielding point (in time or in strain). To characterize the carbopol more thoroughly, I also made startup experiments and successive strain steps with a rheometer.

#### Startup experiments

After loading the sample in the rheometer cell, it is prepared with a preshear at  $100 \text{ s}^{-1}$  in both direction and a few minutes at imposed zero stress. Then rotation at a fixed shear rate, either  $0.1 \text{ s}^{-1}$  or  $1 \text{ s}^{-1}$ , starts at  $t_0$  and the stress is recorded directly from  $t_0$ . Three regimes can be seen on the stress response in time (figure 3.3):

- the linear regime, where  $\sigma = G\gamma$
- a partially plastic regime, where the stress still rises, but slower than linear,

- finally the stress reaches a maximum and starts to decrease towards a finite stationary value.

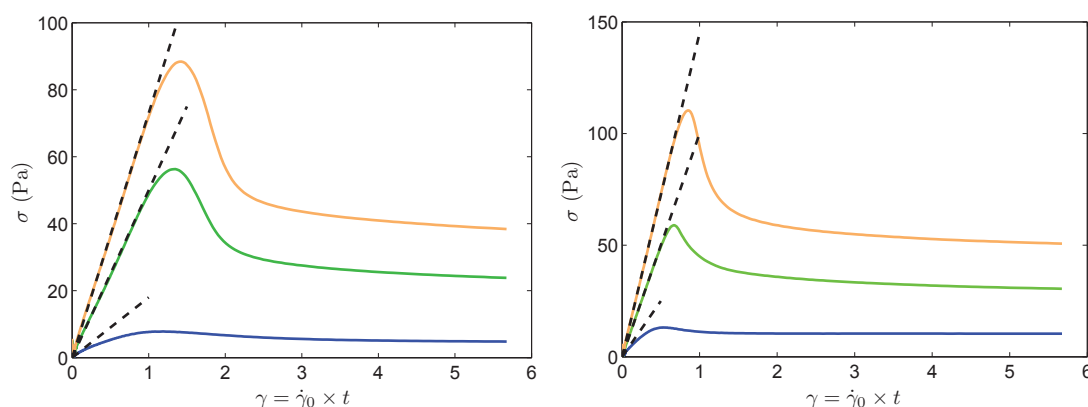


Figure 3.3 – Stress responses to startup experiments on ETD carbopol at  $\dot{\gamma} = 0.1 \text{ s}^{-1}$ . Left: machine-stirred microgels. Right: hand-stirred microgels. Blue curves:  $c = 0.5\%$ . Green curves:  $c = 1\%$ . Orange curves:  $c = 1.5\%$ . The dashed black lines represent  $G \times \gamma$  with  $G$  from independent measurements in linear oscillatory shear.

The strain at which the stress is maximum is denoted  $\gamma_M$ . It varies very little with the shear rate but mostly with the type of carbopol (ETD or U10) and with the stirring. The maximum stress value itself increases strongly with concentration and is also higher when  $G$  is higher (for different stirrings for example, see figure 3.3).

An interesting fact is that the difference between the maximum stress value and  $G\gamma_M$  is always of the order of 10 Pa, whatever the concentration, the shear rate, the carbopol type or the stirring. I do not have an explanation but I think this deserves further investigation in order to understand yielding. An intuition is that it is related to the interaction strength between the elements, which could explain why some yield-stress materials do not exhibit such stress overshoots.

### Response to strain steps

This experiment was motivated by the temporal evolution of the force response in the capillary bridge tensiometer setup, described in details in chapter 4.

After a preliminary preshear at  $100 \text{ s}^{-1}$  in both directions, followed by a few minutes at imposed zero stress, the material is submitted to successive strain steps of amplitude 5% and duration 2, 10 or 60 minutes, and the stress response is measured. The rise between each step lasts 0.5 s, which corresponds to  $\dot{\gamma} = 0.1 \text{ s}^{-1}$ . There are 5 rising steps, up to 25% deformation, and then 5 falling steps, back to no deformation.

Figure 3.4 shows the raw results of one of the experiments. To analyze the relaxation, the total stress response is divided in separate files for each step.

I tried to find a function that could fit all the curves. I based my reasoning on the idea that the stress decreases (resp. increases) after a rising (resp. falling) step because of plastic events (or rearrangements). The imposed deformation  $\gamma_{\text{imp}}$  generates a stress  $G\gamma_{\text{imp}}$ , but each plastic event of typical size  $\xi$  reduces the deformation really experienced by the sample. The stress  $\sigma(t)$  is thus

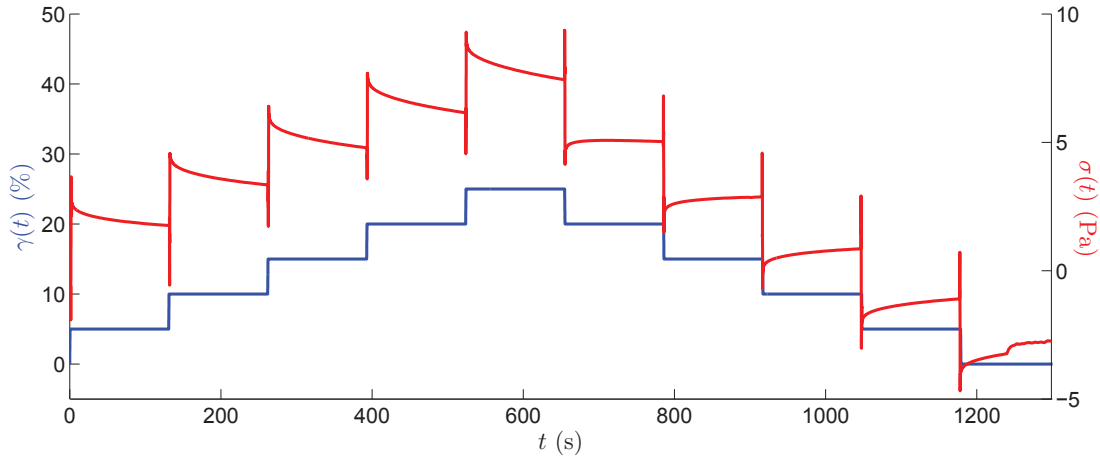


Figure 3.4 – Strain steps (blue) and stress response (red) for a ETD 1% MS carbopol ( $\sigma_y = 14$  Pa). The duration of each step is 2 minutes. The stress response to the last step has a kink: it is an artifact from the rheometer.

related to the rate of plastic events per unit gap length  $\lambda(\sigma, t)$  by:

$$\sigma(t) = G \left( \gamma_{\text{imp}} - \xi \int_0^t \lambda(\sigma(t'), t') dt' \right) \quad (3.1)$$

which gives, after differentiation with respect to time:

$$\dot{\sigma}(t) = -G\xi \lambda(\sigma(t), t) \quad (3.2)$$

An hypothesis can be made on  $\lambda(\sigma, t)$ , based on experiments on creep under the yield stress in carbopol microgels by Lidon *et al.* [89]. The shear strain, under a constant stress, is also due to plastic events, so that the creep strain rate  $\dot{\gamma}(t) \propto \lambda(\sigma_0, t)$ . Lidon *et al.* find a power law for  $\dot{\gamma}(t)$ , with an exponent  $m = -0.61 \pm 0.04$ . I then assume that  $\lambda$  is proportional to  $\sigma$ , which is the simplest possible dependency. Finally I have  $\lambda(\sigma, t) \propto \dot{\sigma}(t) \sim \sigma t^m$ . This relation is very well verified: the plot of  $\log(\dot{\sigma}/\sigma)$  versus  $\log(t)$  is a straight line of slope  $m = -0.6 \pm 0.1$  (figure 3.5, left). Finally:

$$\frac{\dot{\sigma}(t)}{\sigma(t)} = -At^m \quad (3.3)$$

$$\log(\sigma(t)) = \text{cst} - \frac{A}{1+m} t^{1+m} \quad (3.4)$$

$$\sigma(t) = C \exp\left(-\frac{A}{1+m} t^{1+m}\right) \quad (3.5)$$

where  $C$  is the stress at the beginning of the relaxation and  $A \propto G\xi$ .

The first stress curves are well fitted by this function (figure 3.5, right), but less and less as the total deformation increases. Moreover for the first decreasing steps, I observe a non monotonous evolution in time (figure 3.6) which is not described by function 3.5. The most probable explanation is that  $\dot{\sigma}$  is proportional to the actual stress minus a residual stress (and to a power of time). The residual stress must vary in time, but not proportionally to  $\sigma$ . Indeed the

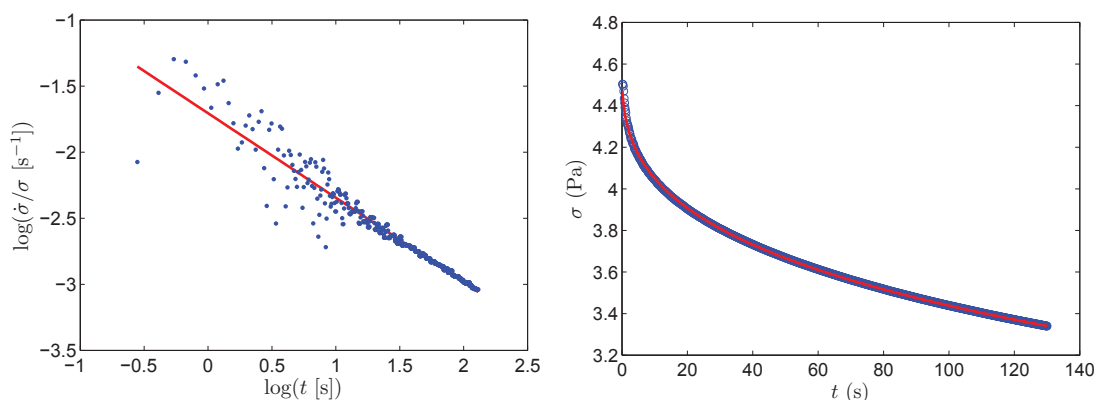


Figure 3.5 – Left: to check the assumption on  $\lambda(\sigma, t)$ ,  $\log(\dot{\sigma}/\sigma)$  is plotted versus  $\log(t)$ . The red line is a linear fit with a slope  $m = -0.64$ . Right: fit of the stress response after a rising 5% strain step. The fitting function is function 3.5.  $A$  and  $m$  are fixed to the values given by the linear fit of  $\log(\dot{\sigma}/\sigma)$ .  $C$  is a free parameter. Here  $C = 4.6$  Pa and  $R^2 = 0.9994$ .

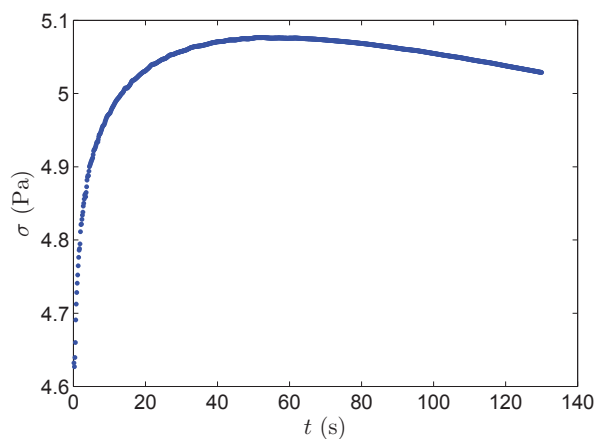


Figure 3.6 – Stress response to the first decreasing strain step after 5 increasing steps. The amplitude of each strain step is 5% and the step duration is about 2 minutes. The stress first increases, reaches a maximum value and finally decreases, which is not well described by the model.

moment where  $\dot{\sigma}$  changes sign does not coincide with the moment where  $\sigma$  changes sign. This will be investigated more in the future.

Figure 3.7 shows the stress response for other experiments comparing the behavior of U10 carbopol (0.25%,  $\sigma_y = 15$  Pa) and ETD carbopol (1.75%,  $\sigma_y = 18$  Pa) in a series of 20% deformation steps. The maximum deformation is 200%, which is more than the yielding deformation  $\gamma_M$  in startup experiments. The goal was to observe what happens when the stress exceeds the yield stress. As can be seen on figure 3.7, U10 and ETD carbopols have very different behaviors. After 2 steps, U10 response is always similar from one step to the following. On the contrary, ETD response seems to be always different, even after 10 steps.

I tried function 3.5 on these stress responses and it also fits well, but for U10 exponent  $m$  differs strongly from  $-0.6$ . It is closer to  $-1.3$ . This could be checked with creep experiments on U10 carbopol. I expect that U10 creep strain evolves as  $\gamma(t) = \gamma_0 - (t/\tau)^{-0.3}$ , where the

important point is the exponent sign more than the value itself.

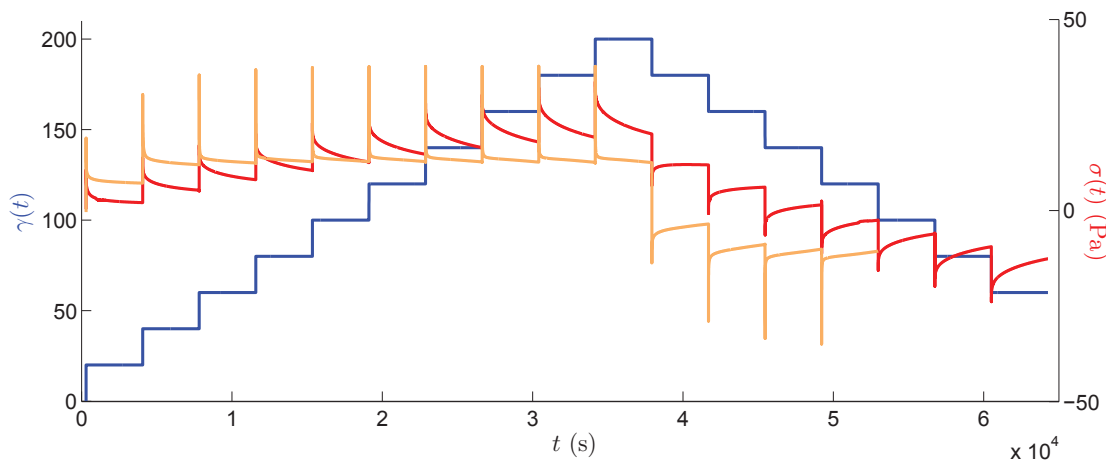


Figure 3.7 – Stress response of ETD (red curve) and U10 (orange curve) carbopols of similar yield stresses (respectively 18 Pa and 15 Pa) to strain steps of amplitude 20% (blue curve). There are 10 rising steps followed by 7 falling steps.

The physical conclusions I draw from this experiment are that even below the yield stress, plastic events happen and cause a relaxation of the stress to zero or at least a small value. This seems to be contradictory with the concept of yield stress. But the yield stress is only well defined in a situation of flow, when the strain increases, even slowly, to balance the plastic events.

### 3.3 Microstructure

I participated in a study on carbopol microstructure initiated by Baudouin Géraud when he worked in the team as a PhD student [90]. His idea was based on a paper by Gutowski *et al.* [9] and consisted in observing in a confocal fluorescence microscope drops of carbopol marked with a fluorescent dye. The motivation of this work was a study by Lee *et al.* [8], who measured a structure size in carbopol microgels by a small angle scattering method. They showed that this size depends sensibly on the preparation protocol. For this reason, we needed to characterize our samples in order to use the structure size in the interpretation of other experiments.

#### 3.3.1 Measurement protocol

**Preparation of the samples.** A fluorescent dye is added to a carbopol sample. The dye we chose is Rhodamine B, whose absorption and emission peaks are respectively 562 nm and 583 nm. Rhodamine B is positively charged and attaches preferentially to the negatively charged polymer. We tested several dye concentrations and the best contrast was obtained with 100  $\mu\text{g}$  of Rhodamine per gram of polymer in the microgel. Rhodamine 6G was also tested with similar results.

**Confocal imaging.** A few hours after addition of the dye, a droplet of colored microgel is deposited on a microscope slide and put on an inverted confocal fluorescence microscope (Leica

TCS SP5). The excitation wavelength is set to 543 nm with a He-Ne laser and emission is recorded from 550 nm to 700 nm.

The objective is a Leica 63x water immersion (NA 1.2), the size of the images is  $1024 \times 1024$  pixels, and the zoom can be adjusted, so that the visible field size ranges from  $25 \mu\text{m}$  to  $145 \mu\text{m}$ . The pixel size ranges from 24 nm to 141 nm. Acquisition is made in photon counting mode with a hybrid detector (Leica HyD). The raw signal-noise ratio is not very good, so the final images are obtained with successive averages and accumulations of raw images. It is important that the microgel does not move (due to unwanted drift of the stage or to evaporation) during the total acquisition time. The acquisition frequency is 1000 single lines per second, so that the acquisition time can reach several minutes for some images (for example 10 line averages and 50 frame accumulations).

Figure 3.8 shows examples of final images. The white zones are the most concentrated in Rhodamine. Besides, we are sure that Rhodamine attaches preferentially to the polymer, because we see a few very bright spots on the most zoomed confocal images (figure 3.9). These spots have a size of  $0.5 \mu\text{m}$  or less (because we reach the resolution limit) and this corresponds to the smallest size measured by Lee *et al.* [8]. They are non-dissolved polymer coils. Apart from these spots, we observe a structure where the elements outline is highlighted, certainly because the dye has not penetrated into the core of the polymer blobs.

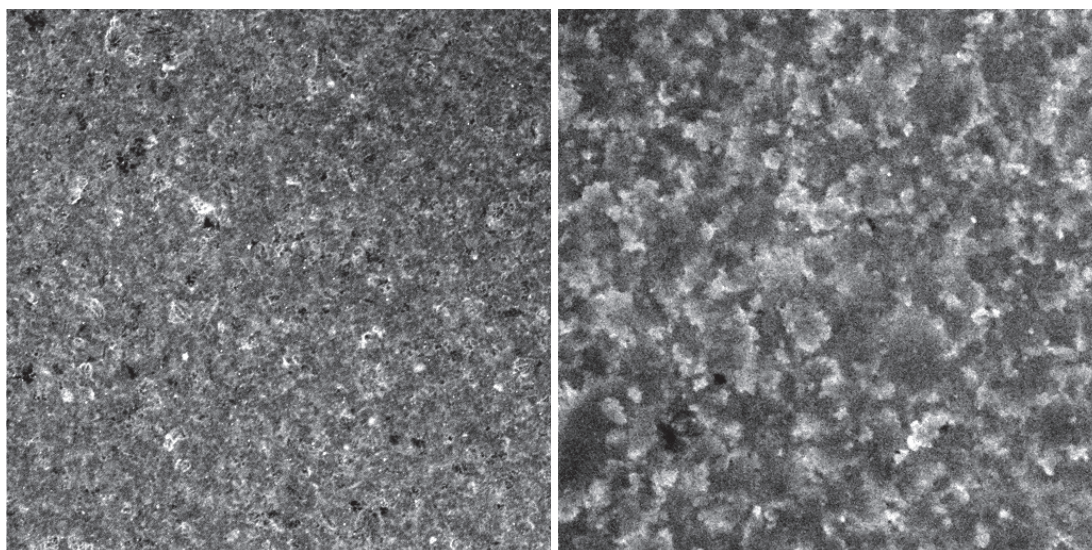


Figure 3.8 – Confocal images of dyed carbopol. The real size of both images is  $145 \mu\text{m}$ . Left: ETD 1% MS carbopol ( $\sigma_y = 9.5 \text{ Pa}$ ), sum of 50 images with 10 line accumulations. Right: U10 0.25% MS carbopol ( $\sigma_y = 17.7 \text{ Pa}$ ), 16 frame accumulations of images with 3 line averages.

The microgel seems to be composed of a dense, slightly heterogeneous and disordered assembly of elements. Elements are irregular, nearly flower-shaped in the case of U10. The size of elements is of the order of  $1 \mu\text{m}$  for ETD and of  $10 \mu\text{m}$  for U10. The difference between ETD and U10 carbopols is visually obvious.

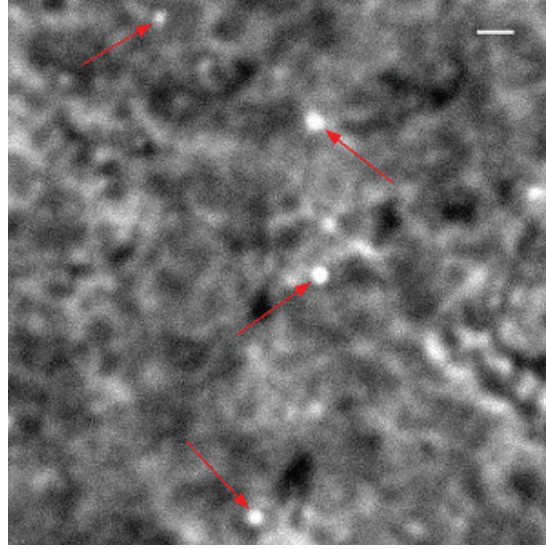


Figure 3.9 – Bright spots that can be seen on a zoomed confocal image of 1% MS carbopol. The total size of the image is  $15\ \mu\text{m}$  and the white bar indicates  $1\ \mu\text{m}$ .

**Analysis.** At the beginning I used the analysis developed by Baudouin Géraud. It is based on an Image Correlation Spectroscopy (ICS) analysis. The gray level (or intensity)  $I(x, y)$  is supposed to be spatially correlated on a scale  $R$ , corresponding to the radius of the single elements of the microgel.

If we decompose  $I(x, y)$  in its mean value  $\langle I \rangle$  and the intensity variations in space  $\delta I(x, y)$ , the normalized correlation function is defined as

$$g(x, y) = \frac{\langle \delta I(x', y') \delta I(x' + x, y' + y) \rangle}{\langle I \rangle^2} \quad (3.6)$$

$$= \frac{G(x, y)}{\langle I \rangle^2} - 1 \quad (3.7)$$

where  $G(x, y)$  is the autocorrelation function of  $I(x, y)$ .

$G(x, y)$  can be easily computed by Fast Fourier Transform (FFT). Finally, the normalized correlation function is computed using the following relationship:

$$g(x, y) = \frac{\mathcal{F}^{-1} [ |\mathcal{F}[I]|^2 ]}{N_p \langle I \rangle^2}(x, y) - 1 \quad (3.8)$$

where the operators  $\mathcal{F}[\cdot]$  and  $\mathcal{F}^{-1}[\cdot]$  respectively denote the FFT and the inverse FFT, and  $N_p$  is the total number of pixels of the pictures which is here  $1024^2$ .

Autocorrelation functions computed for samples of different concentrations are all similar and have the same features. They all present a peak which sharply decreases to a small residual value  $g_\infty$ . They have a circular symmetry which indicates isotropic correlations. This allows for an analysis of the functions in radial coordinates. The radial correlation functions  $g(r)$  are calculated by averaging  $g(x, y)$  on concentric circles of radii  $r$  centered on the position of the maximum.

The function that best fits the data is a decreasing exponential, which is consistent with the fact that the correlation function reported in semi-dilute polymer solutions conventionally decreases exponentially [91]:

$$g(r) = g_0 \exp\left(-\frac{r}{R}\right) + g_\infty \quad (3.9)$$

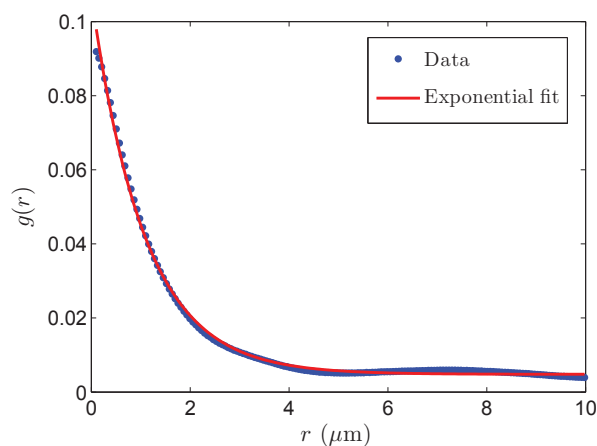


Figure 3.10 – Correlation function  $g(r)$  for a ETD 1% MS carbopol, and the corresponding exponential fit. The typical size is  $R = 1.1 \mu\text{m}$ .

$R$  is identified as the typical radius of the elements of the microgel.

However, Baudouin and I did not use the same amount of Rhodamine in our microgels, and the image aspect is slightly different. Baudouin’s images look more like nearly homogeneous patches, whereas my images look like a disordered honeycomb, the edges of each polymer blob being brighter than the core (figure 3.11). For this reason I tried a Fourier transform analysis on my images, to highlight a prominent frequency.

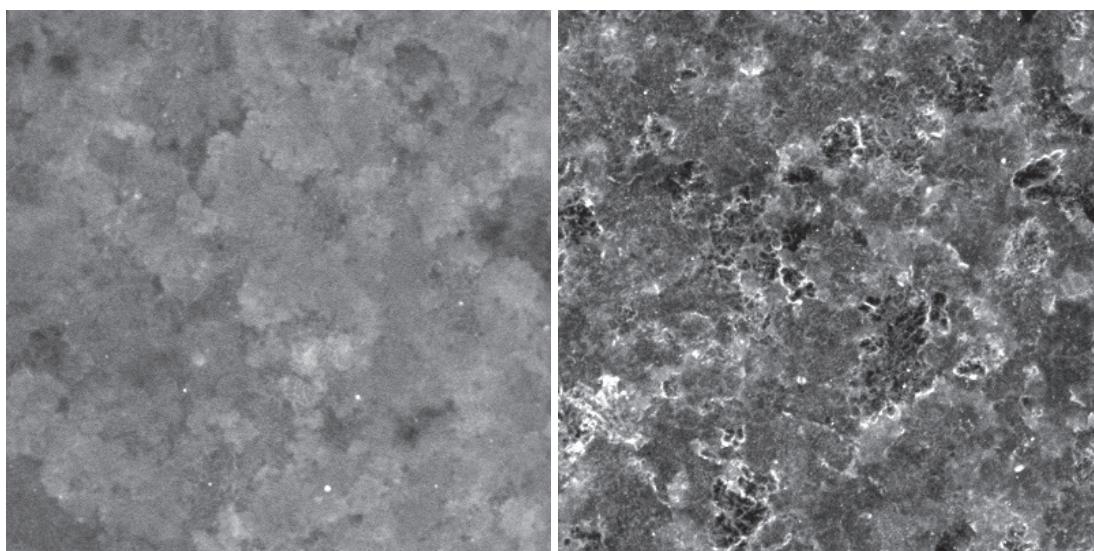


Figure 3.11 – Left: confocal image of a ETD 0.5% HS carbopol made by Baudouin. Right: confocal image of carbopol of the same concentration and stirring, made by me. Both images: size  $100 \mu\text{m}$ .

The principle of the analysis is to find a characteristic frequency in each image, which should

be the inverse of the characteristic size of the individual elements. To achieve this, I process each image with Matlab in the following way:

1. The very bright or dark spots (twice the standard deviation above or below the mean intensity) are removed and replaced by a patch with the mean intensity.
2. The intensity distribution is rescaled to be between 0 and 1 and the mean intensity is removed.
3. The 2D Fourier transform is computed with a Fast Fourier Transform algorithm.
4. The frequency spectrum of the image is computed. It shows a sharp peak with circular symmetry at zero frequency, rapidly decreasing to zero as the frequency increases.
5. The azimuthal average of the image spectrum is computed, plotted and fitted.

This procedure is represented schematically in figure 3.12.

The resulting averaged frequency spectrum also looks like a decreasing exponential function. However the data are not perfectly fitted by an exponential. A better fit is the sum of a very narrow gaussian and of a decreasing exponential:

$$I^*(k) = I_0 + Ae^{-\left(\frac{k}{W}\right)^2} + Be^{-kD_c} \quad (3.10)$$

$I_0$  is a small residual constant related to the noise in the initial image.  $W$  is the width of the narrow gaussian, of the order of  $0.1 \mu\text{m}^{-1}$ .  $1/D_c$  is the characteristic size of the decreasing exponential.

The narrow gaussian can be interpreted as a low frequency peak due to the global heterogeneity of the image. It would be appreciable to produce and analyze artificial images to check this.  $D_c$  is assumed to be the characteristic size of the carbopol microstructure.

The exact functional form of the fit is not totally justified, but it fits perfectly the experimental data (see figure 3.13), gives a reproducible characteristic length  $D_c$ , and moreover this length is very consistent with the size found by Baudouin with the correlation analysis on the same kind of carbopol (table 3.1).

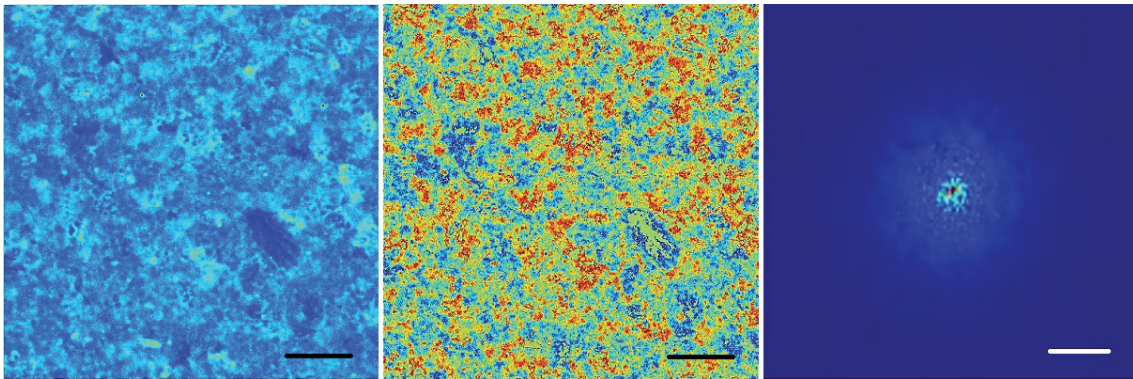


Figure 3.12 – Illustration of the image processing. Left: image before processing. Center: rescaled image after removing the intensity peaks. Right: frequency spectrum of the image. For the real-space images the black bar stands for  $10 \mu\text{m}$ . For the Fourier-space image, the white bar stands for  $1 \mu\text{m}^{-1}$ .

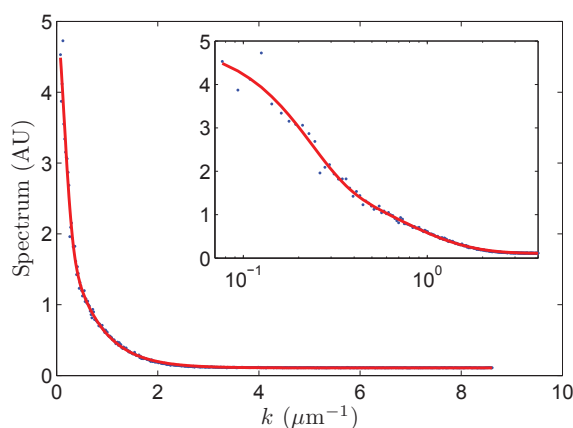


Figure 3.13 – Averaged frequency spectrum of an image of ETD 1% MS carbopol of real size  $59\ \mu\text{m}$ . The blue dots are the data and the red line is the fit (see text). Here  $W = 0.23\ \mu\text{m}^{-1}$  and  $D_c = 1.66\ \mu\text{m}$ .

### 3.3.2 Results

**Typical size and effect of concentration.** A typical element size  $D_c$  is extracted from the fit introduced above. The process is repeated on 10 images made with a same sample but at different places in the sample. Samples of different concentrations are measured the same way. The results are summarized in table 3.1. The size  $D = 2R$  obtained with the correlation method is also indicated for information, but it is less appropriate for my images.

Note that the size returned by the Fourier transform analysis varies slightly with the total image size, because the possible windowing effect is not perfectly taken into account in the fit. For this reason all the results of this analysis are given for images of size  $59\ \mu\text{m}$ .

Concentration	mean( $D_c$ ) ( $\mu\text{m}$ )	std( $D_c$ ) ( $\mu\text{m}$ )	mean( $D$ ) ( $\mu\text{m}$ )
0.25%	2.13	0.12	3.3
0.5%	1.94	0.08	2.8
0.75%	1.77	0.07	not done
1%	1.66	0.06	2.4
1.25%	1.62	0.05	2.2

Table 3.1 – Characteristic structure sizes for different concentrations of ETD MS carbopol, based on the analysis of images of size  $59\ \mu\text{m}$ . For each concentration, the mean and standard deviation of  $R_c$  are calculated on 10 images.  $D$  is the average size returned by the ICS analysis [90].

Two main elements are remarkable: a rather well defined size can be extracted with this procedure, of the order of  $2\ \mu\text{m}$ ; and this size clearly decreases when concentration increases, which is a logical evolution if a single element always contains roughly the same number of monomers. However the evolution of  $D_c$  with concentration  $C$  is slower than  $(1/C)^{1/3}$ . A similar evolution is observed with the correlation method, even if the values of  $D$  are slightly higher than  $D_c$ .

Concerning U10 carbopol, only few images were made. The typical size returned by the

analysis is around  $D_c = 5 \mu\text{m}$  for a concentration of 0.25%.

**Influence of stirring.** We also noticed a strong influence of stirring on the aspect of the structure and the size. The images of hand-stirred carbopol look much more heterogeneous than those of machine-stirred carbopol (see figure 3.14), and big ( $\sim 10 \mu\text{m}$  or even more) bright structures appear more often. This is also qualitatively visible in the Fourier transform analysis: the frequency spectrum is not well fitted by function 3.10, it contains much more low frequencies in proportion, compared to MS carbopol (figure 3.15).

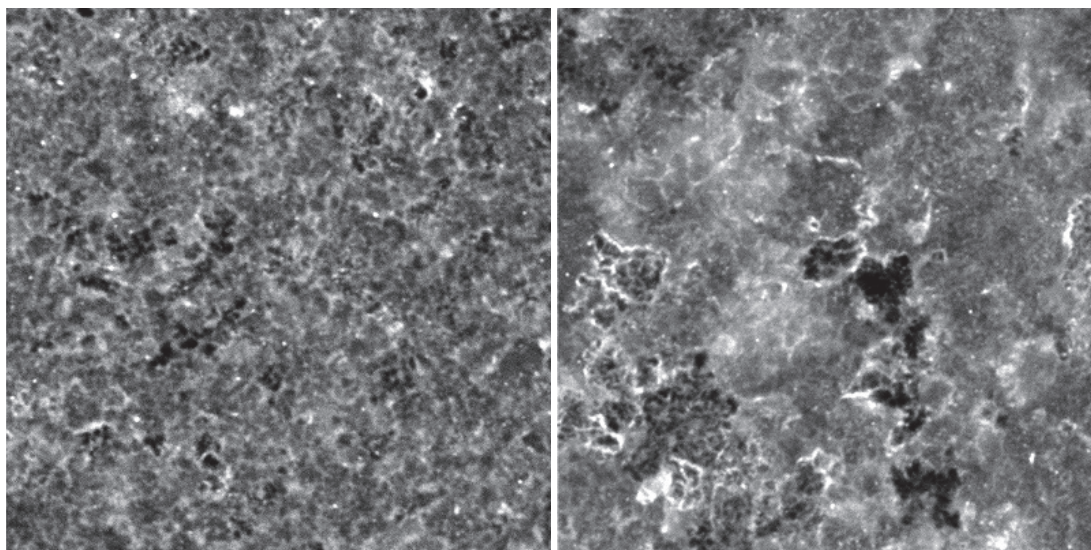


Figure 3.14 – ETD 0.5% carbopols imaged in the same conditions (image size  $59 \mu\text{m}$ ). Left: machine-stirred microgel. Right: hand-stirred microgel.

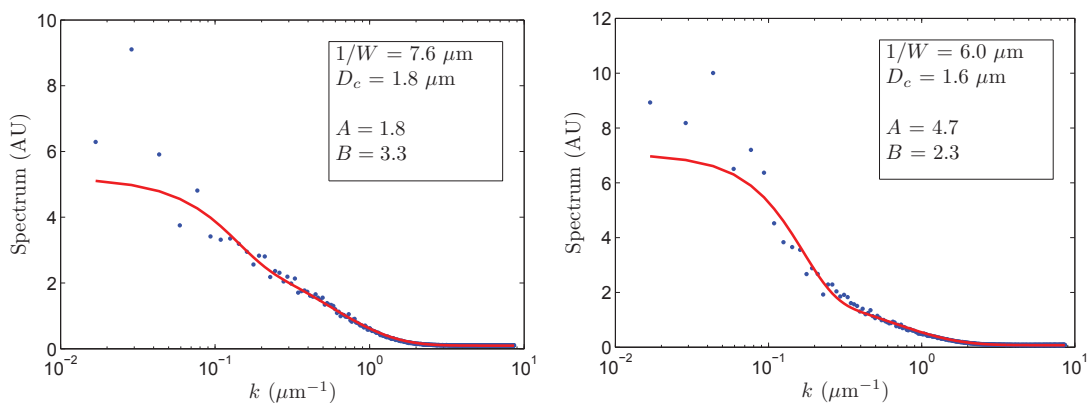


Figure 3.15 – Fourier Transform analysis of ETD 0.5% carbopols in the same conditions. The red line is the fit corresponding to function 3.10. Left: machine-stirred microgel. Right: hand-stirred microgel. The average ratio  $A/B$  (see equation 3.10) on 10 images is 0.44 for MS carbopol and 2.33 for HS carbopol.

These observations, combined with the higher yield stress and elastic modulus of HS carbopol, make us think that stirring breaks big clusters of polymer blobs, and possibly also changes the interactions by disentangling the polymer chains between the blobs.

### 3.3.3 Perspectives

The most important improvement that can be made on this experiment is the fitting function of the frequency spectrum of the images. A more physical function would hopefully give access to reliable values of  $D_c$ . However, the present analysis already provides the most important informations: a rough size ( $D_c \approx 2 \mu\text{m}$ ) and its evolution with concentration and carbopol type.

From a wider point of view, many interesting experiments could be lead in the future, based on this work. Firstly, the marking of polymers can be improved by chemically grafting fluorophores on the carbopol carboxylate groups. This would give images with a better contrast and probably provide a more precise control over the fluorophore density relative to the polymer density. Moreover, this would stop diffusion of the dye in the microgel and allow to mix marked and unmarked carbopols. Then, the inner structure and even the shape of the jammed blobs could be studied, again with confocal microscopy.

A better knowledge of the microstructure of the microgel will give access to the ingredients for models, explaining for example yield-stress fluids rheology, wall slip or the yielding mechanism. Our microstructure measurements have already allowed us to rationalize confinement effects in carbopol via a fluidity model developed by Goyon *et al.* [92] and the measurement of a cooperativity length [90].



## Chapter 4

# Adhesion of a capillary bridge of yield-stress fluid

### Contents

---

<b>4.1</b>	<b>Setup and protocol</b> . . . . .	<b>70</b>
<b>4.2</b>	<b>Simple fluids</b> . . . . .	<b>74</b>
4.2.1	Expectations . . . . .	74
4.2.2	Experimental results . . . . .	76
<b>4.3</b>	<b>Observations with carbopol</b> . . . . .	<b>78</b>
<b>4.4</b>	<b>Elastoplastic model</b> . . . . .	<b>80</b>
4.4.1	General expression of the elastoplastic force . . . . .	81
4.4.2	Filament approximation . . . . .	81
4.4.3	Pancake approximation . . . . .	82
4.4.4	Resulting curves and comparison with experiments . . . . .	83
<b>4.5</b>	<b>Discussion</b> . . . . .	<b>86</b>
4.5.1	Influence of yield stress and volume . . . . .	86
4.5.2	Influence of elasticity . . . . .	86
4.5.3	Effect of the initial stress . . . . .	88
4.5.4	Surface tension . . . . .	89
<b>4.6</b>	<b>Conclusion</b> . . . . .	<b>91</b>
<b>4.7</b>	<b>Perspectives</b> . . . . .	<b>92</b>

---

The first half of my thesis has focused on the interplay between surface tension and yield stress in capillary bridges. The aim of this study was to measure the surface tension of carbopol with a capillary bridge setup. This setup, built by H el ene Delano e-Ayari to study the deformation of cell aggregates, seemed particularly appropriate to yield-stress fluids because the fluid system can be smaller than the length  $\Gamma/\sigma_y$ , quantifying the strength of capillary effects with respect to yield stress effects. We thus expected to limit the influence of yield stress on the surface tension value (see section 2.3.5 of chapter 2). In addition, the method had proven to be precise and efficient to measure the surface tension of cell aggregates [93], of which rheology is similar to this of yield-stress fluids [94]. The cell aggregates setup is used here, with some adaptations.

## 4.1 Setup and protocol

**Setup.** The homemade bridge tensiometer (figure 4.1) is designed to measure the surface tension of a small amount of fluid. It consists in two horizontal solid surfaces, between which the liquid bridge is formed. The surfaces are made of glass. The bottom surface (a microscope glass slide) is fixed to a micromanipulator (Sutter Instrument MP285), so that its position can be adjusted by the operator. The adhesion force exerted by the bridge on the surfaces is measured through a flexible copper-beryllium cantilever attached to the top surface (a  $5 \times 5 \text{ mm}^2$  piece of microscopy cover glass). The cantilever size is  $100 \text{ mm} \times 10 \text{ mm} \times 0.3 \text{ mm}$  and it is clamped at its base with a slight angle to compensate for the deflection due to its own weight. It is equipped with an Eddy-current deflection sensor (MicroEpsilon eddyNCDT3700). The signal is recorded by a 16-bits data acquisition board (NI 4096). A high resolution camera (Pixelink PL-A686M, B&W,  $3000 \times 2200$  pixels) coupled to a horizontal microscope (Leica MZ16) and a 1x plan-apo objective (Leica) is used to take pictures of the bridge. The absence of optical distortions has been checked on the picture of a grid. To optimize the contrast and make the later outline detection easier, a LED panel is placed behind the bridge. An example of picture is shown in figure 4.1.

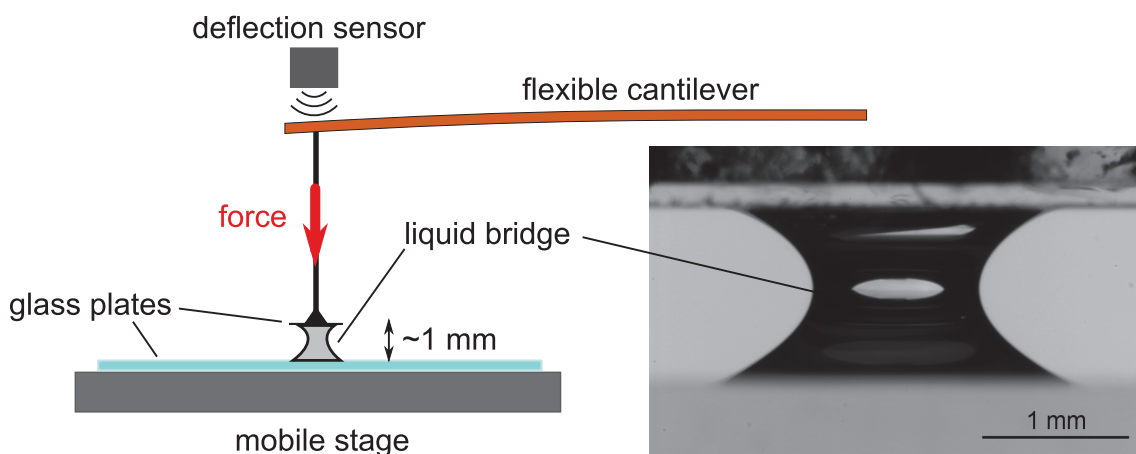


Figure 4.1 – Drawing of the bridge tensiometer setup. Inset: Example of picture of a carbopol bridge. The white stain in the middle is a deformed image of the LED panel situated in the back of the setup.

The main contribution to the uncertainty on the force is the Eddy-current sensor drift. This

sensor is very sensitive to any temperature change. The experiment is situated in the basement and the room temperature is kept roughly constant (within 1 °C in the worst case, depending on the room occupation) with an air conditioning system. This system creates air movements that induce unwanted vibrations of the cantilever. On the other hand, the LED panel heats the atmosphere. A compromise must be found between ventilation and protection against vibrations. So I place a polystyrene lid on the box containing the experiment. However, the drift cannot be totally avoided. Long measurements of the signal in absence of capillary bridge show a slow increase of the signal, evolving on several tens of minutes before reaching a steady value (figure 4.2). The drift amplitude can reach 100 mV in summer when the weather is hot, because the air conditioning system is less effective. To account for it, the initial base value of the signal (before loading the liquid) and its final base value (after having dried the surfaces) are measured and I assume a linear evolution of the baseline between these values during the experiment.

The cantilever has a resonance vibration frequency around 12 Hz. It is a problem each time an external jolt (slamming door, heavy footsteps) causes large oscillations of the cantilever, damped on about 1 minute. The electronics department of the lab made a digital filter to remove the resonance peak from the signal spectrum. This filter is a notch filter, with a tunable peak frequency and a narrow bandwidth of about 1 Hz. The effects of the filter on the signal at short timescales have no importance, as the signal is measured in a quasi steady state.

The temporal resolution is about 20 Hz and the noise on the signal is around 0.5 mV, to compare to the signal amplitude, of the order of 100 mV to 1 V .

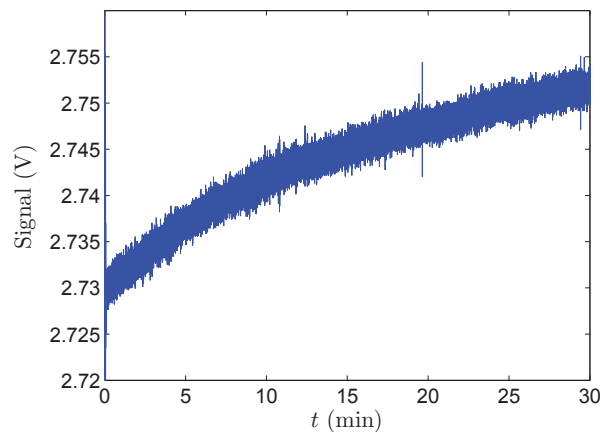


Figure 4.2 – Measurement of the sensor baseline drift on 30 minutes (January 2014). The drift is stronger in summer.

Both top and bottom plates must be perfectly cleaned to avoid line pinning which could deform the axisymmetrical bridge, and to avoid polluting the fluid with dust or surfactants. Before each series of measurements, the bottom plate is always thoroughly cleaned in a plasma cleaner. The small top plate is dipped in piranha solution (1 part of hydrogen peroxyde in 2 parts of concentrated sulfuric acid) and rinsed with deionized water.

The cantilever is calibrated each time it is unmounted to be cleaned. Small pieces of metallic wire, precisely weighted (mass ranging from 5 to 120 mg with a precision of 0.1 mg), are hanged

to the small rod holding the top surface and the corresponding deflection signal is measured. The signal is unfortunately not linear with the weight of the wires. The data are fitted with a polynomial of order 2 to 5 and the fitting parameters are stored for the later signal-to-force conversion (figure 4.3).

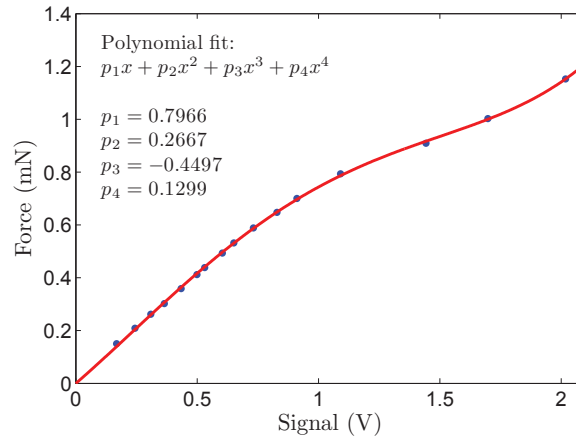


Figure 4.3 – Example of a calibration. The dots are the measurements and the red line is a polynomial fit of order 4 (the constant term is set to 0).

**Measurement protocol.** To form the bridge, a droplet is deposited with a pipette tip on the bottom plate which is then moved upwards until contact of the liquid with the top plate. Generally the liquid immediately spreads on the whole upper plate and the two plates are stuck together, so the bridge must always be strongly stretched before the beginning of the measurement. During the experiment, the bridge is stretched or compressed step by step by changing the position of the bottom plate and then let to equilibrate. A series of about 10 stretching steps is followed by a series of about 10 compression steps, and most of the time by a second series of a few stretching steps. Each step represents a deformation of 5% to 10% of the total height. The aspect ratio of the bridge is always kept of the order of 1 to avoid pinch off and breakup (figure 4.4).

Because of evaporation and maybe also creep (this is discussed later), the force is never completely steady, but the force value and the picture are saved when the force evolution is sufficiently slow (about  $1 \mu\text{N/s}$ ) compared to the total force step (of the order of  $100 \mu\text{N}$  in a few seconds). A typical example of force step is shown in figure 4.5.

**Data processing.** For each deformation step, the surface mean curvature is computed from the picture. The image is thresholded with a manually chosen grayscale value. A difficulty of the thresholding stage is that at the top and bottom of the bridge, because of optics artifacts, two outlines can be distinguished (figure 4.6). This makes an automatic edge detection nearly impossible, but the outline obtained from the manual threshold is very satisfactory.

The outline of the bridge profile is then stored as a function of the altitude  $z$ . Because no explicit function can describe the bridge profile, and because, as we will see later (see section 4.7), bridges of yield-stress fluids do not have a laplacian profile (ie. the profile is not a solution

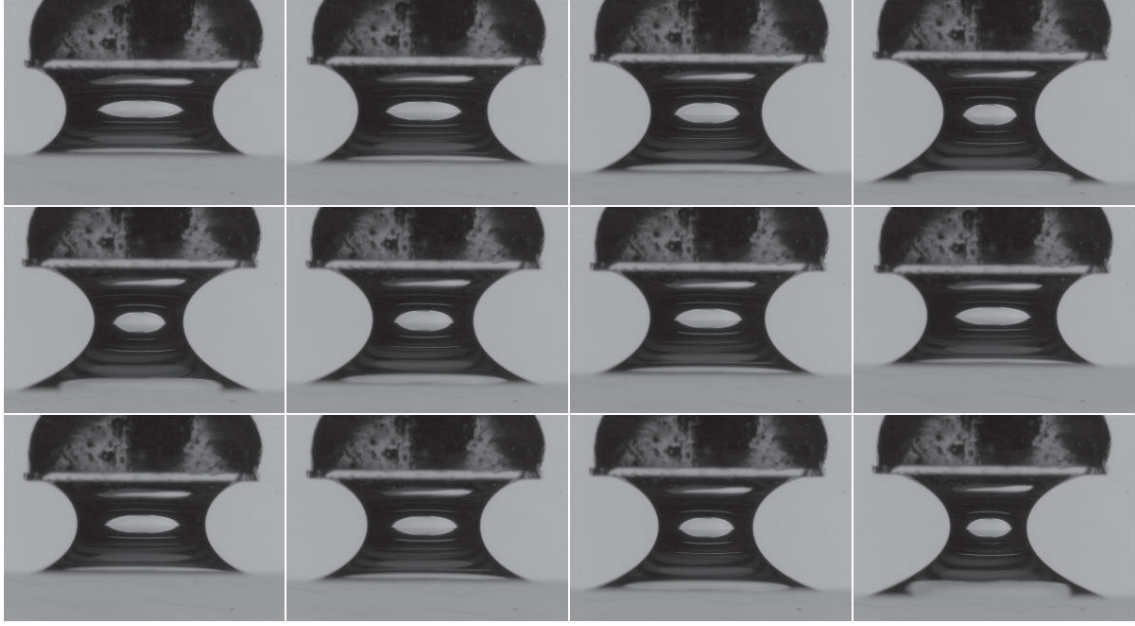


Figure 4.4 – Typical series of deformation steps (one image for each two steps). The first row represents stretching steps, the second row compression steps and the last row stretching steps again. The deformation is imposed through the bottom plate vertical translation.

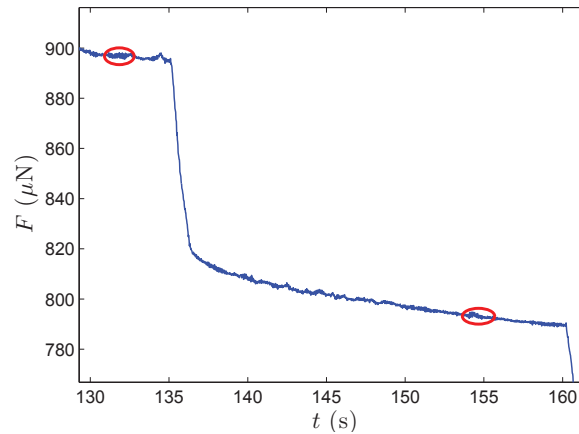


Figure 4.5 – Example of force evolution during a stretching step. The red ellipses represent the moments of the simultaneous force value and image recording.

of Laplace's equation 1.4), the outline is fitted with a high-order polynomial. Concerning the choice of the polynomial order, a compromise is necessary: a too low order does not allow to fit the profile well enough, although a too high order generates large oscillations in the function derivatives (needed for the curvature). After several tries an order 11 has been chosen. The curvature of the surface is computed as:

$$C(z) = \frac{1/R(z)}{(1 + R'(z)^2)^{1/2}} - \frac{R''(z)}{(1 + R'(z)^2)^{3/2}}$$

with  $R(z)$  the profile of the bridge. Figure 4.7 shows the oscillations around a linear evolution of the curvature  $C(z)$ .

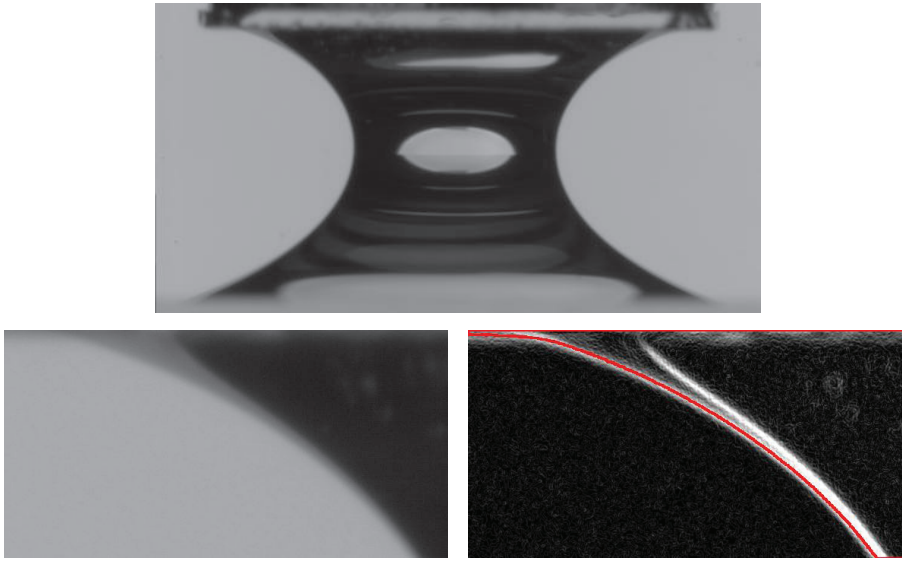


Figure 4.6 – Top: image of a capillary bridge of water. A gray zone can be seen along the edge at the top and the bottom. Bottom left: zoom on a gray zone. Bottom right: superposition of the image gradient intensity map and of the outline obtained from a manual thresholding of the image. Two gray level discontinuities appear neatly on the gradient intensity map.

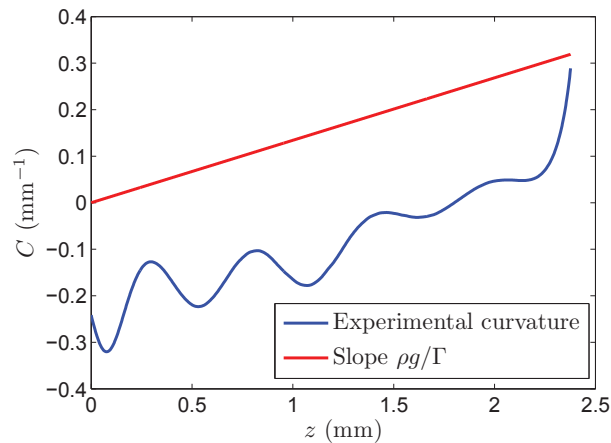


Figure 4.7 – Curvature of a bridge of water as a function of the vertical coordinate  $z$ . Theoretically  $C(z)$  should be linear with a slope  $\rho g / \Gamma$ . Here we see some non-physical oscillations due to differentiation. The red line gives the expected slope.

## 4.2 Simple fluids

### 4.2.1 Expectations

**Force balance.** At equilibrium the force on the cantilever ( $F$ ) and the geometry of the bridge are directly linked via the surface tension  $\Gamma$  of the fluid. More precisely the force measured by the cantilever is the sum of the pressure force at the liquid-plate interface and of the capillary force at the perimeter of this interface [95]:

$$F = -\pi R_0^2 \Delta p + 2\pi R_0 \Gamma \sin \theta_0$$

where  $R_0$  and  $\theta_0$  are the radius and the contact angle defined on figure 4.8, assuming cylindrical symmetry, and  $\Delta p$  is the pressure difference between the fluid and the atmosphere.

For simple fluids the same force balance can be done at each height  $z$  of the bridge, and especially at the neck ( $z_N$ ) where  $\sin \theta(z_N) = 1$ . In the following all geometrical parameters are measured at the neck, and they are denoted with a subscript  $N$ .

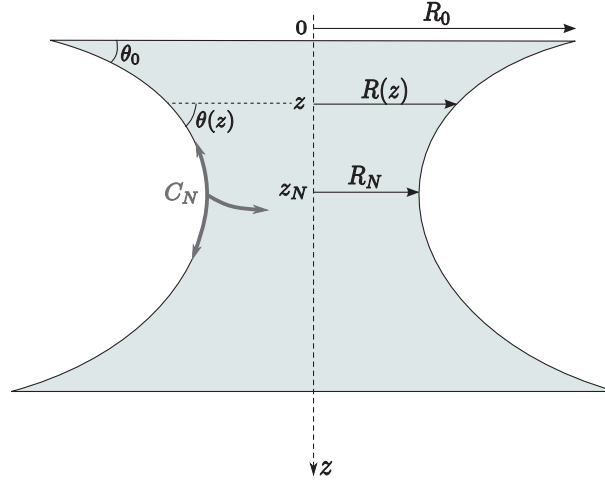


Figure 4.8 – Definition of the main geometrical parameters.

To account for gravity, it is necessary to add the weight of fluid above  $z_N$  (denoted  $W$ ) to the force balance:

$$F = W - \pi R_N^2 \Delta p + 2\pi R_N \Gamma \quad (4.1)$$

$R_N$  being the radius of the bridge at the neck.

Finally Laplace's law allows one to replace the pressure difference  $\Delta p$  with  $\Gamma C_N$ ,  $C_N$  being the mean curvature of the surface at the neck:

$$F - W = \Gamma(2\pi R_N - \pi R_N^2 C_N) \quad (4.2)$$

$$= \Gamma L \quad (4.3)$$

$L$  has the dimension of a length, although it cannot be measured directly on the system. It is defined as:

$$L = 2\pi R_N - \pi R_N^2 C_N \quad (4.4)$$

Thus, if  $F - W$  ( $W$  can be estimated multiplying the density by the integrated profile) is plotted as a function of  $L$ , a linear relation is expected, and the slope is the surface tension  $\Gamma$ .

Because of the oscillations in the curvature described above, the measurement of  $C_N$  is not very accurate. To reduce the uncertainty,  $C(z)$  for simple fluids is fitted with a straight line, and  $C_N$  is the value of the linear fit at  $z_N$ . For yield-stress fluids, it is not possible and the actual value  $C(z_N)$  is taken as  $C_N$ . An error bar  $\Delta C_N = 10^{-4} \text{ px}^{-1}$  is estimated from the global order of magnitude of the oscillations amplitude. The error bar on  $L$  is then computed as:

$$\Delta L = 2\pi \Delta R_N (1 + R_N C_N) + \pi R_N^2 \Delta C_N \quad (4.5)$$

with  $\Delta R_N = 1$  px.

The error bars are represented on a few force- $L$  plots to give an idea of their magnitude. Moreover they are taken into account for the linear fit. The uncertainty on the slopes is under 1 mN/m for simple fluids and about 2 mN/m for yield-stress fluids.

## 4.2.2 Experimental results

In order to validate the setup, the experiment has been first performed with simple fluids. As described in the paragraph ‘Measurement protocol’, in the previous section, stretching as well as compression are tested to check the influence of the dynamics history on the results.

With pure water and silicon oil, the force- $L$  plot indeed shows a proportional relation (see figure 4.9) and the slopes correspond to respective surface tensions of  $(74 \pm 1)$  mN/m and  $(21 \pm 1)$  mN/m. The expected surface tensions are 73.0 mN/m and 21.0 mN/m (at 18 °C). The agreement is very good, with precision comparable to usual surface tension measurement methods [96, 97, 98, 99].

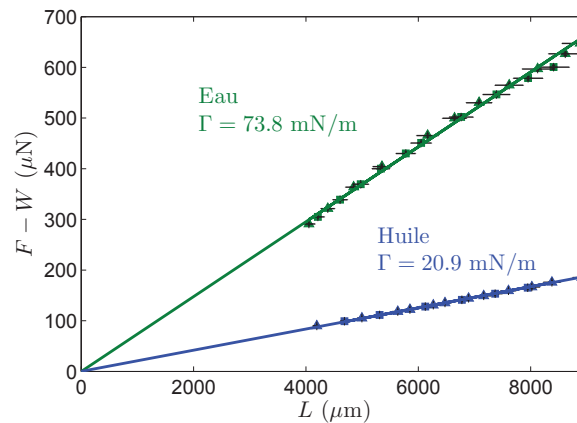


Figure 4.9 – Force- $L$  plots for deionized water (green) and silicone oil (blue). The lines are fits of the data. The force  $F - W$  is proportional to  $L$  and the slopes corresponds to the surface tension of the liquids. Triangles and squares respectively stand for stretching and compression steps.

**Effect of wetting hysteresis.** With simple fluids, especially water, I have encountered difficulties with contact angle hysteresis. The data points are not always aligned, in particular when the glass is not perfectly clean and hydrophilic. Although not many experiments have been performed on normal glass (not freshly cleaned in the piranha solution) there seems to be a correlation between the contact angle variation (reflecting contact angle hysteresis) and the force dispersion. This is illustrated in figure 4.10. In any case, the difference between the stretching branch and the compression branch slopes  $\Delta\Gamma$  is never more than 20 mN/m even when the contact angle hysteresis is strong ( $25^\circ$  or more). I proposed and supervised an internship on this issue. The results are detailed in annex B.

For this reason, a treatment is applied on the glass plates to minimize hysteresis when using water. This treatment is described in ref. [100].

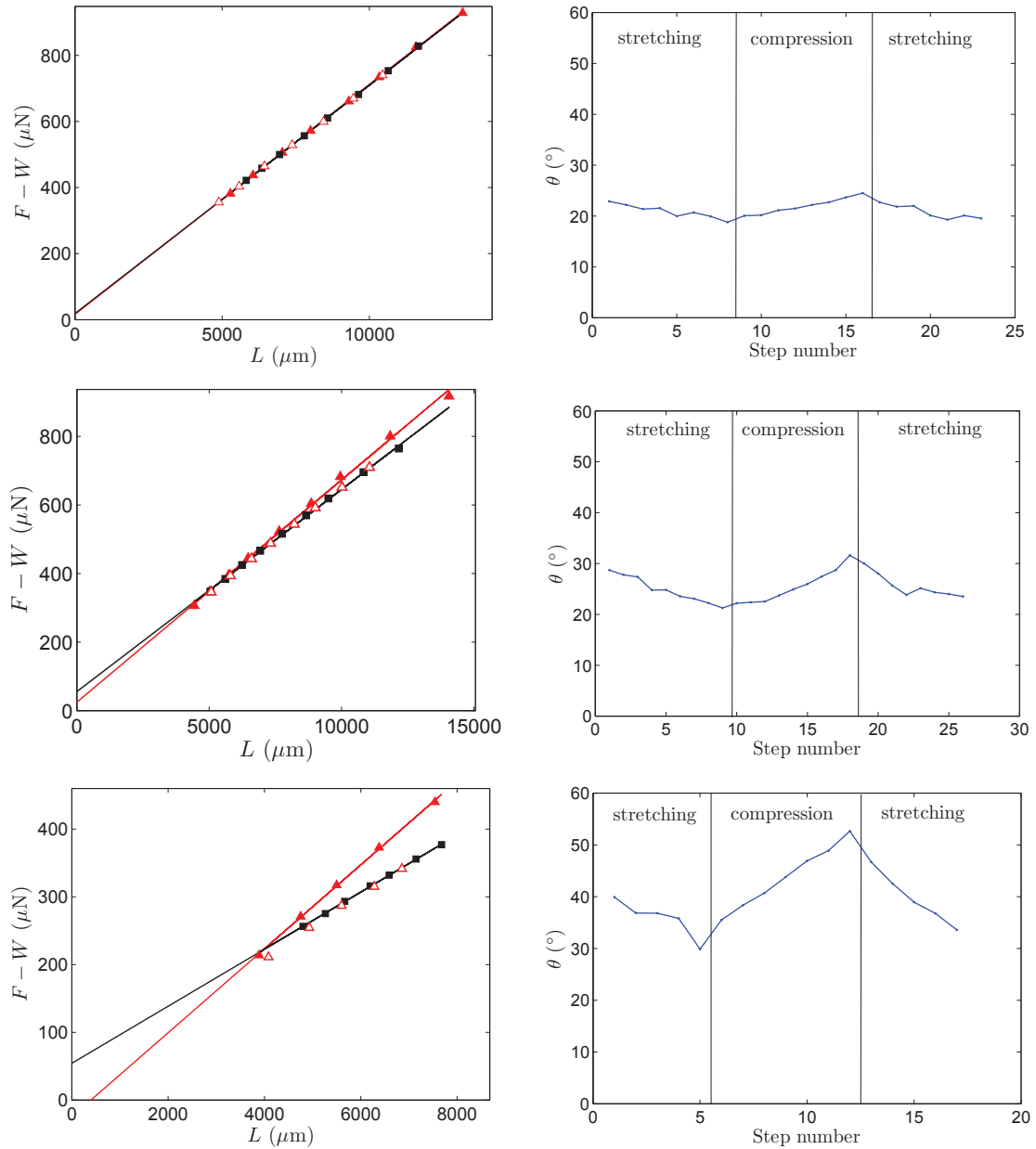


Figure 4.10 – Force-L plots for deionized water on glass, and plot of the contact angle for each step. Three different experiments are presented. The difference is the glass surface treatment: at the top, the glass is freshly cleaned with piranha; in the middle it is just cleaned with ethanol and water; at the bottom it is polluted with dried carbopol. A correlation clearly appears between the contact angle range and the misalignment of the points.

### 4.3 Observations with carbopol

As for simple fluids, I start with a series of stretching steps and then a series of compression steps. Most of the time these are followed by a second series of stretching steps. Given that  $L = 2\pi R_N - \pi R_N^2 C_N$ , and that  $C_N$  is often negative,  $L$  increases with  $R_N$ . Therefore the most compressed bridges have large values of  $L$  and a stretching corresponds to a decrease of  $L$  (see figure 4.11).

Typical force- $L$  plots for carbopol ETD 0.25% HS ( $\sigma_y = 5$  Pa) and carbopol ETD 1% MS ( $\sigma_y = 19$  Pa) are reproduced in figure 4.11. One can observe that the points do not all align on a single line. The solid red triangles correspond to the first series of stretching, starting at the top-right angle of the plot. The red line is the linear fit of these points, and its slope is denoted  $\Gamma_{app}^U$ . The black squares correspond to the series of compressions. They align on a second line, whose slope  $\Gamma_{app}^L$  is always smaller than for the stretched points. Note that  $\Gamma_{app}^U$  and  $\Gamma_{app}^L$  are apparent surface tensions. This behavior is reproducible for every sample of carbopol, and the greater the yield stress, the wider the difference of slopes between the two sets of points.

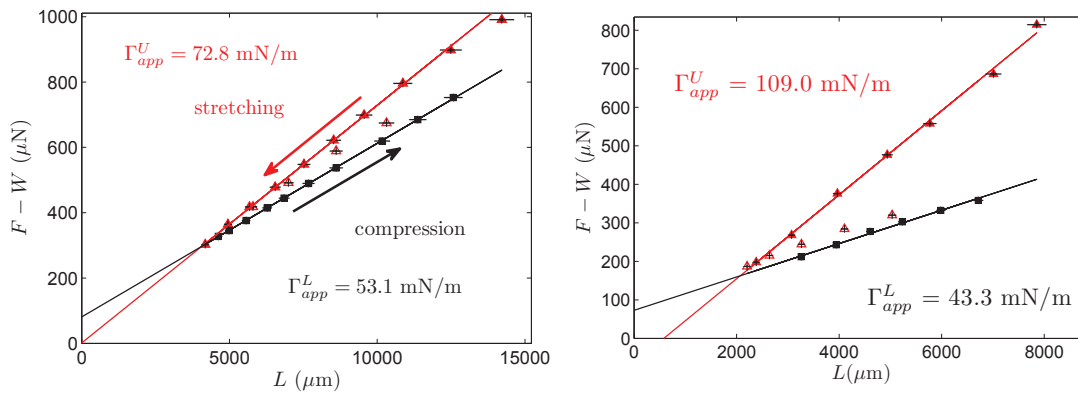


Figure 4.11 – Force- $L$  plot for two different carbopol samples. Left: ETD 0.25% HS, yield stress  $\sigma_y = 4.6$  Pa. Right: ETD 1% MS, yield stress  $\sigma_y = 19.0$  Pa. The solid (resp. empty) red triangles stand for the first (resp. second) series of stretchings, the black squares for the series of compressions. The slopes correspond to the apparent surface tensions, their values are written in the figure.

To confirm the influence of the yield stress on the apparent surface tension, we performed several experiments, varying  $\sigma_y$  between 0.5 Pa and 38 Pa. This could be achieved by varying either the polymer concentration or the stirring. Hand-stirred carbopols have indeed a much greater yield stress than machine-stirred carbopols of same concentration. This is convenient because we can vary the rheology keeping the same chemical composition.

For a few samples the experiment was performed with several droplet volumes between 2  $\mu$ L and 15  $\mu$ L. Moreover for two of them, 10 identical measurements were carried out in order to evaluate the dispersion of the effective surface tension values. The standard deviation of the results is of about 5 mN/m for given yield stress and volume.

Figure 4.12, left, shows the values of the upper and lower slopes as a function of the sample yield stress, and each point is an average on 1 to 4 droplets of similar volume (within 1  $\mu$ L steps) and yield stress (within 1 Pa steps). It can be observed that the upper slope increases with the

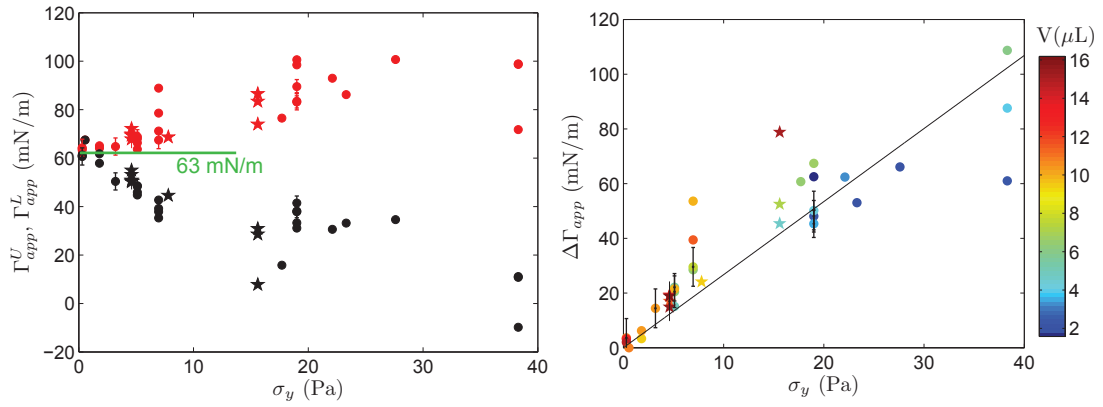


Figure 4.12 – Left: upper (red) and lower (black) slopes of the force- $L$  plots plotted as a function of the yield stress. The green line is a guide for the eyes, indicating the mean surface tension of vanishing yield stress carbopols. The error bars indicate the averaged points (see text). The error on all the other points is  $\pm 5$  mN/m. Right: difference  $\Delta\Gamma_{app} = \Gamma_{app}^U - \Gamma_{app}^L$  of the force- $L$  plots slopes, as a function of the yield stress of the samples. Each point color represents the volume of the droplet. Star-shaped points stand for HS carbopols and dots for MS carbopols. The line is a linear fit. The correlation coefficient  $R^2$  is only 0.74.

yield stress while the lower slope decreases. For vanishing yield stress, they both converge to 63 mN/m.

Figure 4.12, right, is a plot of the slopes difference  $\Delta\Gamma_{app} = \Gamma_{app}^U - \Gamma_{app}^L$  versus  $\sigma_y$ , with the same average as before, and the droplet volume is represented by the point color. It confirms the monotonic dependence of the slopes difference with the yield stress, and it also shows that greater  $\Delta\Gamma_{app}$  often correspond to larger drops, for a given yield stress.

In both figures the star-shaped points stand for HS carbopols samples and the other points for MS samples. The averaged points are indicated by error bars.

Finally, as shown on figure 4.13, the shape of the second stretching cycle (empty red triangles) varies from one experiment to another. The second stretching set of points joins the first stretching line (red) faster when the elastic modulus of the carbopol is higher, for equal yield stresses.

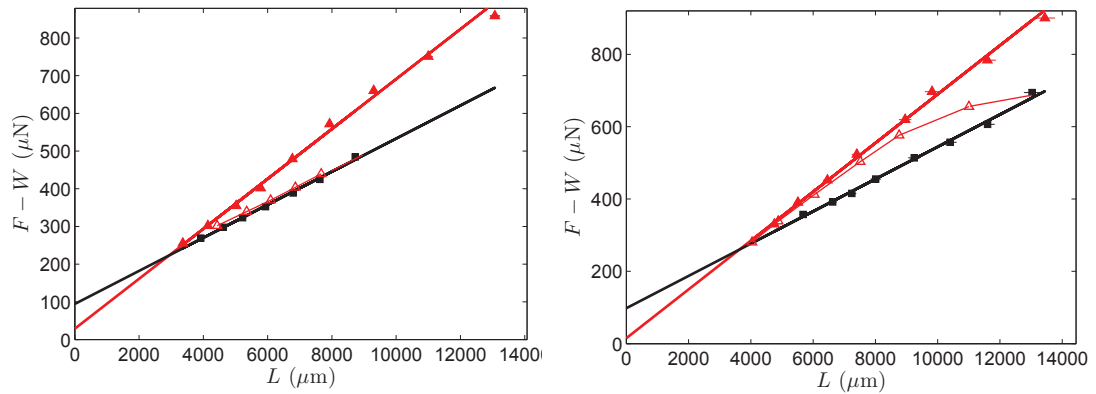


Figure 4.13 – Example of two force- $L$  plots for carbopols of same yield stress  $\sigma_y = 7$  Pa and different elastic moduli. Left: MS carbopol,  $G = 20$  Pa. Right: HS carbopol,  $G = 45$  Pa.

## 4.4 Elastoplastic model

To understand the influence of the different parameters in the experiment, we have developed a simple model in collaboration with Marie Le Merrer and H el ene Delano -Ayari. The goal is to understand the role of the flow history on the curves obtained with a yield-stress fluid.

Because the experiments clearly show an influence of both the yield stress and the elasticity of the fluid, we consider an elastoplastic fluid: below  $\sigma_y$  it behaves as an elastic solid, and at  $\sigma_y$  it flows until it reaches a stationary state. We neglect the consistency  $K$  of the Herschel-Bulkley model as the time evolution of the force is not investigated here, only the final state. Indeed in the experiments  $F$  and  $L$  are systematically measured in a quasistatic state.

The model mimics the experimental protocol and explores the influence of the elastic deformation on the stress state of the bridge for either stretching or compression and different initial conditions. To be able to calculate the stress, we consider two limiting simplified geometries, the filament and the pancake (figure 4.14). This model allows to faithfully reproduce the experimental results and thus to explain the observations exposed in part 4.3.

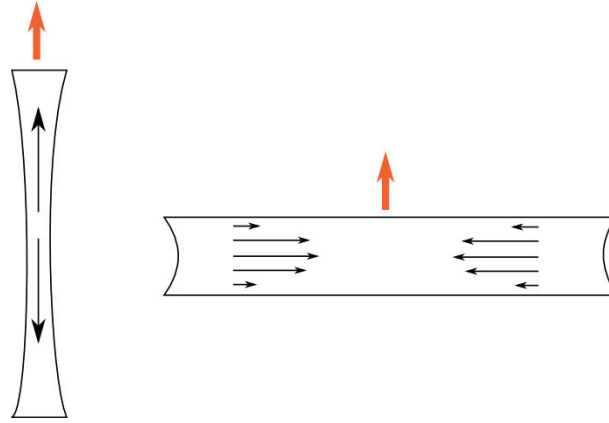


Figure 4.14 – Simplified geometries used to calculate the stress inside the bridge. Left: filament geometry. Right: pancake geometry.

A drop of viscoplastic liquid with yield stress  $\sigma_y$  and shear elastic modulus  $G$  is considered. The drop has a nearly cylindrical shape with height  $h$  and neck radius  $R_N$ , so that the volume of the drop is  $V \approx \pi R_N^2 h$ . We denote  $\theta = 30^\circ$  the contact angle, which is roughly the contact angle observed in the experiments. The total curvature is assumed to be constant along  $z$ , and the geometric parameter  $L$  is approximated by

$$\begin{aligned} L &= 2\pi R_N - \pi R_N^2 \left( \frac{1}{R_N} - \frac{2 \cos \theta_0}{h} \right) \\ &= \pi R_N + \frac{2\pi R_N^2 \cos \theta_0}{h} \\ &\approx \pi \sqrt{\frac{V}{\pi h}} + \frac{2V \cos \theta_0}{h^2} \end{aligned}$$

For a given volume  $V$ , the filament (resp. pancake) geometry corresponds to heights  $h \gg (V/\pi)^{1/3}$  (resp.  $h \ll (V/\pi)^{1/3}$ ). The volume is fixed to  $V = 10 \text{ mm}^3$ , as often encountered in

experiments. This corresponds to  $(V/\pi)^{1/3} \approx 1.5$  mm. As this is the typical experimental value of  $h$ , the experiments do not correspond to any of these limiting geometries (filament or pancake), but to an intermediate regime where  $h \sim R$ . However, as discussed later, the results of the model do not qualitatively depend on the geometry chosen.

#### 4.4.1 General expression of the elastoplastic force

Let us define  $\vec{v} = u\vec{e}_r + w\vec{e}_z$  as the flow velocity *just before* the measurement.  $p$  is a hydrodynamic pressure and it is defined as  $p = p_{\text{in}} - p_{\text{out}} - \Gamma C$ , where  $p_{\text{in}}$  is the pressure inside the liquid,  $p_{\text{out}}$  the atmospheric pressure and  $\Gamma C$  the Laplace pressure.

In general the vertical elastoplastic force on the upper plate is defined as

$$F_{\text{ep}} = \int_0^{R_N} T_{zz} 2\pi r dr \quad (4.6)$$

where  $\mathbf{T}$  is the total stress tensor. It can be decomposed into a deviatoric tensor and an isotropic pressure tensor:  $\mathbf{T} = \boldsymbol{\sigma} - p\mathbf{I}$ .

The three-dimensional Herschel-Bulkley constitutive equation is expressed as

$$\boldsymbol{\sigma} = (\sigma_y + K\dot{\gamma}^n) \frac{\dot{\gamma}}{\dot{\gamma}} \quad (4.7)$$

with

$$\dot{\gamma} = \begin{pmatrix} 2\frac{\partial u}{\partial r} & 0 & \frac{\partial w}{\partial r} + \frac{\partial u}{\partial z} \\ 0 & 2\frac{u}{r} & 0 \\ \frac{\partial w}{\partial r} + \frac{\partial u}{\partial z} & 0 & 2\frac{\partial w}{\partial z} \end{pmatrix} \quad (4.8)$$

and  $\dot{\gamma} = \sqrt{(\text{Tr}(\dot{\gamma}^2) - (\text{Tr}\dot{\gamma})^2)/2}$  [101].

When  $\dot{\gamma}$  vanishes, because of the yield stress the deviatoric stress tensor does not decrease to zero. Instead it is

$$\boldsymbol{\sigma} = \sigma_y \frac{\dot{\gamma}}{\dot{\gamma}} \quad (4.9)$$

In simple geometries,  $\dot{\gamma}$  can be simplified and  $\dot{\gamma}$  can be estimated.

Finally, the pressure  $p$  also has to be calculated, from a force balance at a free surface, for example at the bridge neck. At this point  $\sigma_{rr} - p = 0$ .

#### 4.4.2 Filament approximation

In this geometry, usually encountered in capillary thinning or filament-stretching devices [77, 79], elongational deformation and normal stress (and not shear) are assumed to be dominant. The deformation rate tensor  $\dot{\gamma}$  reduces to

$$\dot{\gamma} = \begin{pmatrix} 2\frac{u}{r} & 0 & 0 \\ 0 & 2\frac{u}{r} & 0 \\ 0 & 0 & -4\frac{u}{r} \end{pmatrix}$$

so  $\dot{\gamma} = \left| \frac{2u}{\sqrt{3}r} \right|$  and

$$\boldsymbol{\sigma} = \sigma_y \begin{pmatrix} \frac{S}{\sqrt{3}} & 0 & 0 \\ 0 & \frac{S}{\sqrt{3}} & 0 \\ 0 & 0 & -\frac{2S}{\sqrt{3}} \end{pmatrix}$$

$S$  is the sign of the radial velocity  $u$  just before the flow arrest. The pressure  $p$  is constant in the filament. At the neck it is  $p = \sigma_{rr} = \frac{S}{\sqrt{3}}$ , so the total vertical stress along the top plate is

$$T_{zz} = -S\sqrt{3}\sigma_y$$

Small height variations  $\Delta h$  are imposed to the system. The corresponding step in deformation is:

$$\Delta\varepsilon = \frac{\Delta h}{h}$$

and the total stress before each step is denoted  $T_0$ .  $S$  is the opposite sign of  $\Delta\varepsilon$ . But in the elastoplastic hypothesis, after one or a few steps, the deformation is possibly not sufficient for the fluid to have yielded. Then if the fluid is still in an elastic regime,  $T_{zz}$  can be smaller than the value calculated above. Therefore the new stress after a step is given by the following function:

$$T_{zz} = \begin{cases} -\sqrt{3}\sigma_y & \text{if } T_0 + 3G\Delta\varepsilon < -\sqrt{3}\sigma_y \\ T_0 + 3G\Delta\varepsilon & \text{if } -\sqrt{3}\sigma_y < T_0 + 3G\Delta\varepsilon < \sqrt{3}\sigma_y \\ +\sqrt{3}\sigma_y & \text{if } T_0 + 3G\Delta\varepsilon > +\sqrt{3}\sigma_y \end{cases}$$

The stress increment is  $3G\Delta\varepsilon$  because the fluid is considered incompressible, so that its elongational Young modulus is  $E = 3G$ .

Finally, the normal elastoplastic force applied on the cantilever is evaluated at each step:

$$F_{\text{ep}} = T_{zz}\pi R_N^2 = T_{zz} \frac{V}{h}$$

### 4.4.3 Pancake approximation

We also checked the other limit of a flattened drop. In this case, the deformations and dissipation are dominantly due to shear along the  $z$  direction. Therefore we cannot use a homogeneous description but we need to describe the stress profile at the wall. Here one can use the lubrication assumption. The deformation rate tensor  $\dot{\gamma}$  approximates as

$$\dot{\gamma} = \begin{pmatrix} 0 & 0 & \frac{\partial u}{\partial z} \\ 0 & 0 & 0 \\ \frac{\partial u}{\partial z} & 0 & 0 \end{pmatrix}$$

so  $\dot{\gamma} = \left| \frac{\partial u}{\partial z} \right|$  and

$$\boldsymbol{\sigma} = \sigma_y \begin{pmatrix} 0 & 0 & S \\ 0 & 0 & 0 \\ S & 0 & 0 \end{pmatrix}$$

The momentum equation gives  $\frac{\partial p}{\partial r} = \frac{\partial \sigma_{rz}}{\partial z} \sim 2\sigma_{\text{wall}}/h$ . At the neck, on the surface,  $p = \sigma_{rr} = 0$ .

In the same way as for the filament, the elastic response at low deformation is taken into account by the function

$$\sigma_{\text{wall}}(r) = \begin{cases} -\sigma_y & \text{if } T_0 + \Delta T(r) < -\sigma_y \\ T_0 + \Delta T(r) & \text{if } -\sigma_y < T_0 + \Delta T(r) < \sigma_y \\ +\sigma_y & \text{if } T_0 + \Delta T(r) > +\sigma_y \end{cases}$$

where  $\Delta T(r) = 3Gr \frac{\Delta h}{h^2}$ , assuming a Poiseuille (ie. parabolic) elastic deformation. The new radii are also reevaluated after each step with the formula  $r' = r - \frac{r\Delta h}{2h}$ . Finally

$$\begin{aligned} F_{\text{ep}} &= - \int_0^{R_N} p(r) 2\pi r dr \\ &= - [p(r)\pi r^2]_0^{R_N} + \int_0^{R_N} \frac{\partial p}{\partial r} \pi r^2 dr \\ &= \int_0^{R_N} \frac{2\sigma_{\text{wall}}(r)}{h} \pi r^2 dr \end{aligned}$$

which is evaluated at each step.

#### 4.4.4 Resulting curves and comparison with experiments

In the experiments the drop is initially stretched so the initial stress is set to  $+\sqrt{3}\sigma_y$  for the filament or to  $+\sigma_y$  for the pancake. Then many successive steps of deformation  $\Delta h$  are applied to the model drop, starting with stretching, then compressing and finally stretching again. For the filament,  $\Delta h = 50 \mu\text{m}$  and  $h$  ranges from 1.5 mm to 4.5 mm. For the pancake,  $\Delta h = 10 \mu\text{m}$  and  $h$  ranges from 1 mm to 1.5 mm.

For each step, the total traction force, which is the sum of the capillary force  $\Gamma L$  and the elastoplastic one  $F_{\text{ep}}$ , is calculated for  $\Gamma = 60 \text{ mN/m}$ . Different values of the rheological parameters have been used for the filament and the pancake. For the filament, figure 4.15 shows results for  $\sigma_y = 2 \text{ Pa}$  and  $5 \text{ Pa}$ , using the following approximation of  $L = \pi\sqrt{V/(\pi h)}$ . For the pancake, figure 4.17 shows results for  $\sigma_y = 10 \text{ Pa}$  and  $20 \text{ Pa}$ , with  $L \approx \frac{2V \cos \theta}{h^2}$ .

Several values of the elastic modulus  $G$  have also been tested:  $G/\sigma_y = 0.5, 2$  and  $8$  for the filament, and  $G/\sigma_y = 1, 4$  and  $8$  for the pancake. The results are shown in figures 4.16 and 4.18.

On figure 4.15, the two plots differ only by the yield stress value. It is clear that the slopes difference between the two branches increases with the yield stress  $\sigma_y$ . The same feature can be seen on figure 4.17, obtained with the pancake approximation. Figure 4.16 represents three typical force- $L$  plots from the model, for a given yield stress ( $\sigma_y = 5 \text{ Pa}$ ) and different elastic moduli  $G$ . It shows that the elastic modulus has a strong influence on the shape of the stretching-compression cycle. The change in the shape of the stretching and compression branches can induce errors in the estimation of  $\Gamma_{\text{app}}^U$  and  $\Gamma_{\text{app}}^L$ , especially if  $G/\Gamma$  is very small. In the case  $G/\Gamma = 0.5$ , the yielding point is never reached during the compression stage, and the elastoplastic force is purely elastic

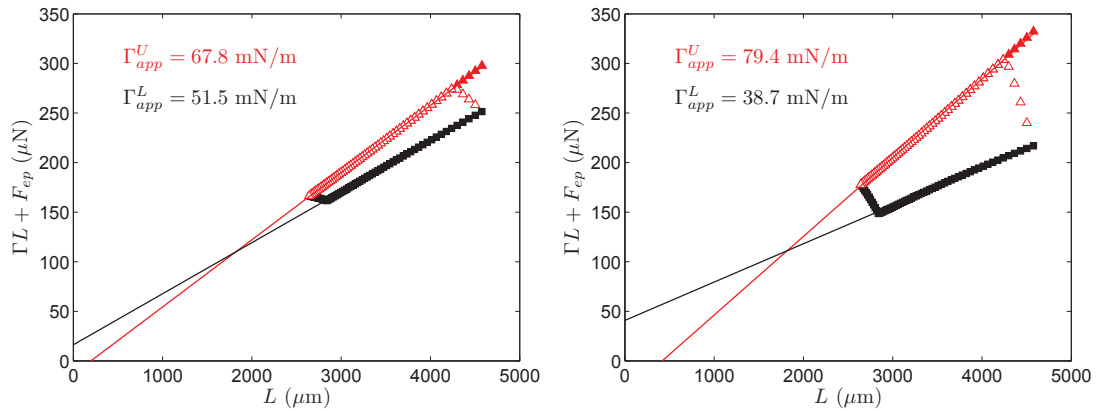


Figure 4.15 – Results from the model:  $F$  as a function of  $L$  for a filament geometry, with  $G/\sigma_y = 8$ . Left:  $\sigma_y = 2$  Pa. Right:  $\sigma_y = 5$  Pa.

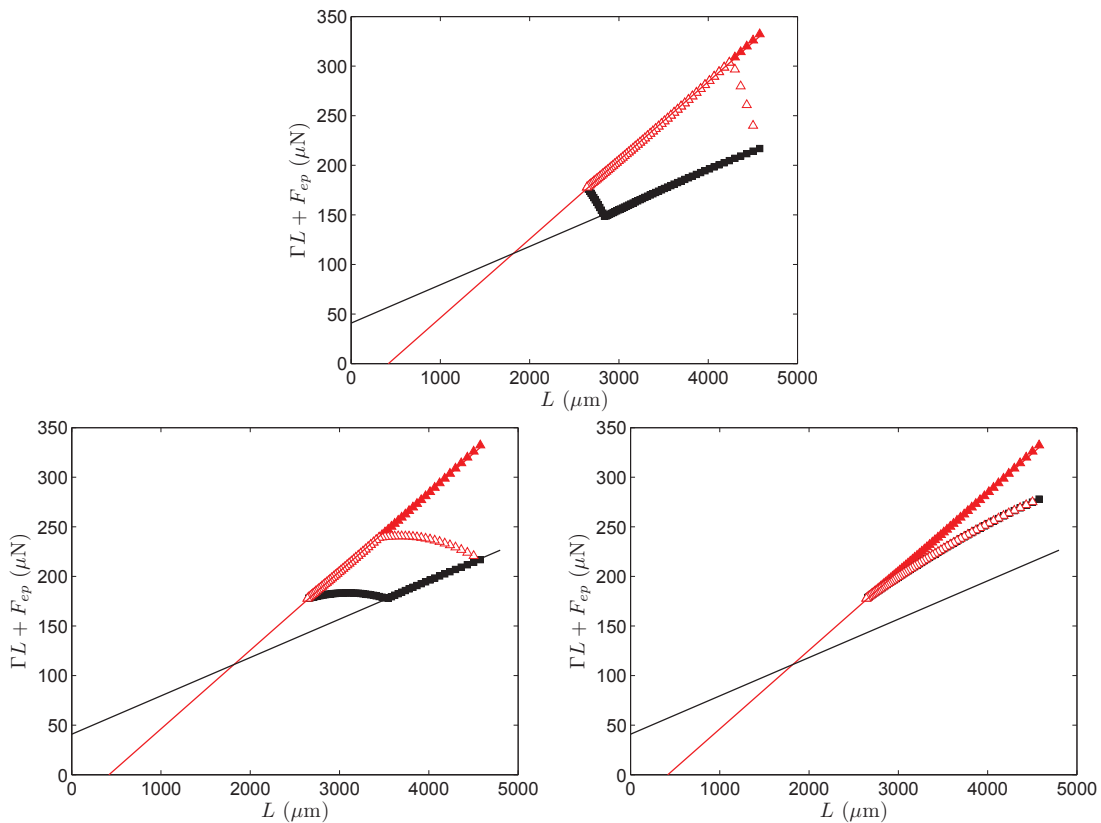


Figure 4.16 – Results from the model:  $F$  as a function of  $L$  for a filament geometry.  $\sigma_y = 5$  Pa and  $G/\sigma_y = 0.5, 2$  and  $8$  from a) to c).

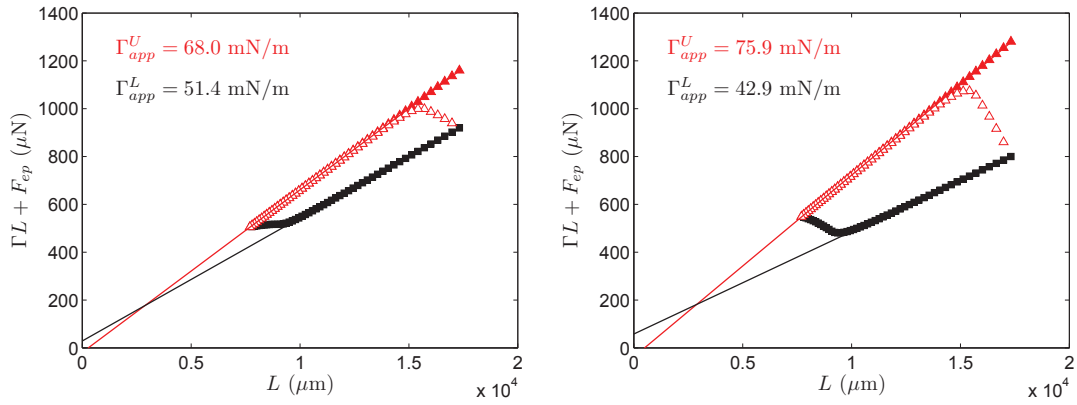


Figure 4.17 – Results from the model:  $F$  as a function of  $L$  for a pancake geometry, with  $G/\sigma_y = 8$ . Left:  $\sigma_y = 10$  Pa. Right:  $\sigma_y = 20$  Pa.

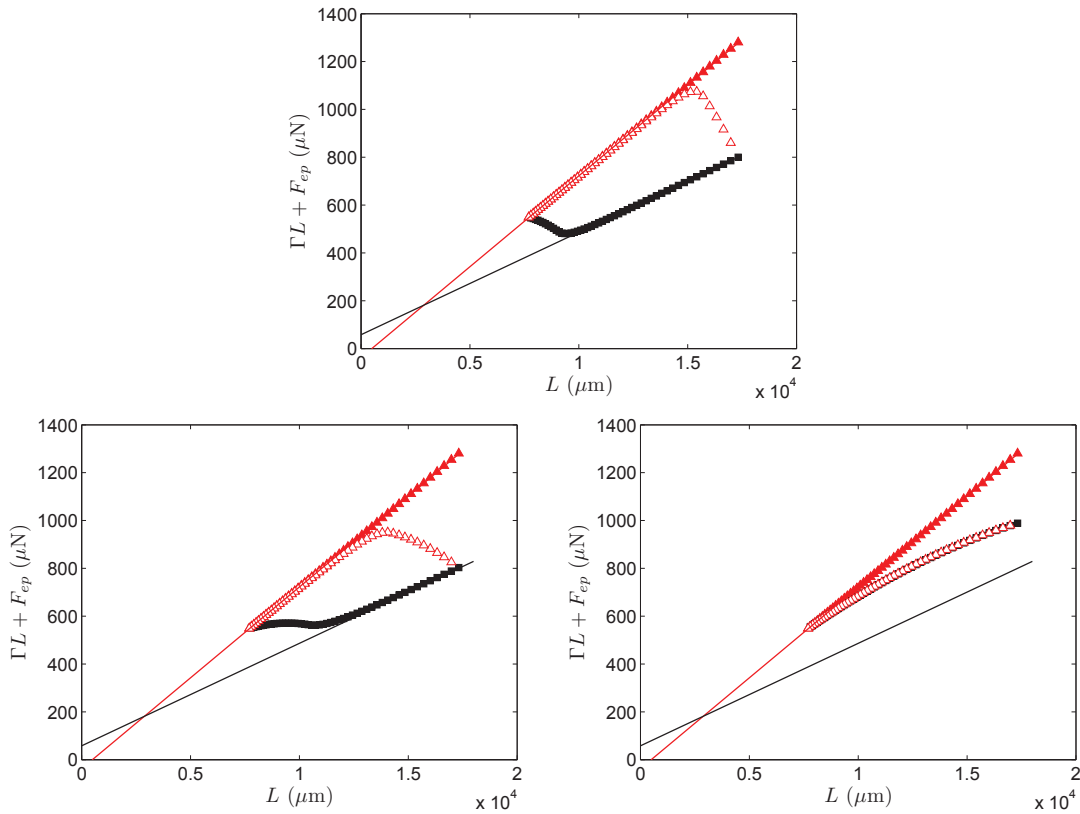


Figure 4.18 – Results from the model:  $F$  as a function of  $L$  for a pancake geometry.  $\sigma_y = 20$  Pa and  $G/\sigma_y = 8$  (top), 4 (bottom left) and 1 (bottom right).

and reversible. Again, the same phenomenon is observed with the pancake model (figure 4.18). In the model and presumably also in the experiments, the initial stress is maximal (the fluid has been deformed plastically). Then the slope of the stretching branch is not affected by a low  $G/\Gamma$ .

Note that for values of  $G/\sigma_y$  of the order of 10 or more, the maximal elastoplastic stress is reached immediately after the direction change. This means that for  $G/\sigma_y \geq 10$  the points fall on two limiting curves determined only by the yield stress. These two curves are symmetrical with respect to  $F - W = \Gamma L$ . This allows to find the true value of  $\Gamma$  by taking the mean of the two limiting slopes:

$$\Gamma = 1/2(\Gamma_{\text{app}}^U + \Gamma_{\text{app}}^L) \quad (4.10)$$

## 4.5 Discussion

### 4.5.1 Influence of yield stress and volume

The model confirms the influence of yield stress on the difference of apparent surface tensions. For large enough elastic moduli  $G \gg \sigma_y$ , the excess force due to the yield stress can be approximated by  $\frac{\Delta\Gamma_{\text{app}}}{2} \times L$ . In the filament geometry, assuming that the stress has reached its saturation value, this excess force can be estimated by  $\sqrt{3}\sigma_y \times \pi R_N^2$ , and  $L \approx \pi R_N$  so the slopes difference reduces to  $\Delta\Gamma_{\text{app}} \propto R_N \sigma_y$ . In the pancake geometry, the excess force is about  $\frac{2\pi}{3}\sigma_y \times R_N^3/h$  [102] and  $L \approx 2\pi R_N^2 \cos \theta_0/h$  so the relation  $\Delta\Gamma_{\text{app}} \propto R_N \sigma_y$  still holds.

To refine the interpretation, we rescaled our experimental data with the droplet size. Namely, considering the most compressed state (indicated with an asterisk), the yield stress was multiplied by the neck radius  $R_N^*$ . The effective surface tension difference  $\Delta\Gamma_{\text{app}}$  shows to be proportional to the resulting quantity. The alignment of the data points is better after rescaling (figure 4.19,  $R^2 = 0.85$ ) than for the raw data (figure 4.12,  $R^2 = 0.74$ ) and the prefactor is of order 1.

This evidences that even a static surface tension measurement will depend on the flow history, and this all the more as the yield stress is high and the droplet is large. The error on the measurement, if it is performed after a flow, will be of the order of  $\sigma_y \times r$  with  $r$  a dimension of the system. The length  $r$  must be thoroughly identified. In our experiments the bridge radius at the most compressed state  $R_N^*$  is the characteristic length scale because it corresponds to the greatest force difference in a force- $L$  plot and thus determines  $\Delta\Gamma_{\text{app}}$ .

### 4.5.2 Influence of elasticity

Results of figure 4.13 clearly show that  $G$  has a strong effect on the shape of the stretching-compression cycle. Indeed the elastoplastic force depends on the elastic deformation of the bridge (see part 4.4), and especially at changes of deformation direction.

To analyze this effect in a more systematic way, the difference between the force  $F - W$  of the first step of the second stretching and the force corresponding to a compressed bridge at the same  $L$  (see figure 4.20, left) was measured on each force- $L$  plot. This force difference  $\Delta F$  is plotted as a function of an estimated elastic force  $\Delta F_{\text{estim}}$  in figure 4.20, right. In the filament

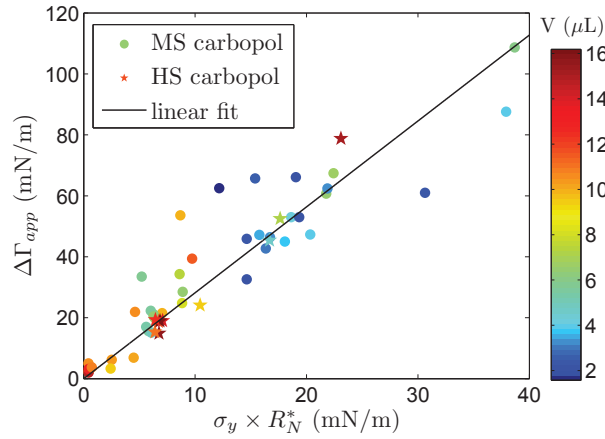


Figure 4.19 – Effective surface tensions difference  $\Delta\Gamma_{app}$  versus  $\sigma_y R_N^*$  (see text). The line is a linear fit for which  $R^2 = 0.85$  and the prefactor is 2.8.

approximation this elastic force corresponds to:

$$\Delta F_{estim} = 3G \times \frac{\delta h}{h} \times \pi R_N^2 \quad (4.11)$$

where  $3G$  is an estimation of the Young modulus of the gel,  $\frac{\delta h}{h}$  is the relative variation of the bridge height  $h$  on the first step of the second stretching and  $\pi R_N^2$  is the section of the bridge at the neck after the first step of the second stretching. These two forces are nearly equal, which evidences the elastic behavior at the change between compression and stretching. This confirms that the shape of the stretching-compression cycle is driven by the elasticity modulus  $G$ .

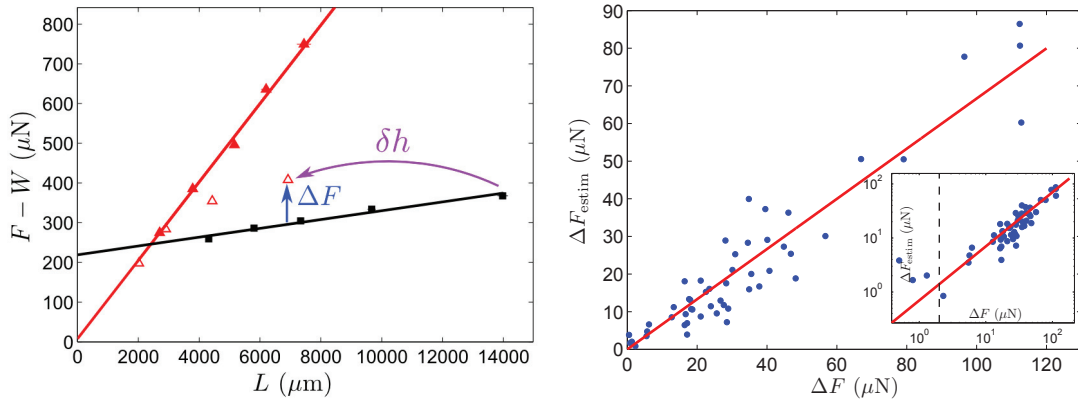


Figure 4.20 – Left: Definition of  $\Delta F$  in a force- $L$  plot. Right: Calculated elastic force (see text)  $\Delta F_{estim}$  versus  $\Delta F$  (measured). The red line is a linear fit with a slope of 0.67. Inset : same plot in log log scale. The dashed line indicates the measurement error on the x-axis. On the y-axis, the error is around 25% of the values.

This analysis provides a criterion on the minimal stretching magnitude  $\delta h$  necessary to saturate the elastoplastic stress and reach the plastic regime in a single stretching step. The force difference  $\Delta F$  must be equal to  $2\sqrt{3}\sigma_y\pi R_N^2$  (still in the filament approximation), which means

that if:

$$\frac{\delta h}{h} > \frac{2\sqrt{3}}{3} \frac{\sigma_y}{G} \approx \frac{\sigma_y}{G} \quad (4.12)$$

then the cycle has reached the limiting (red) line. Any further stretching step has to produce  $F(L)$  points aligned on the limiting line.

For machine-stirred ETD carboxyl, in the worst case  $\sigma_y/G \approx 0.5$ , which corresponds to  $\delta h/h \approx 50\%$  to reach stress saturation. This criterion has not been tested yet but it seems experimentally accessible.

### 4.5.3 Effect of the initial stress

Many experimental force- $L$  plots show a positive y-intercept for the stretching part (red fits), whereas this feature does not appear in the model, where this y-intercept is always negative. This can be explained as follows: the model assumes that the initial stress is maximum (ie. the fluid has reached the yielding point) before the first stretching phase. But this cannot be checked experimentally. It is likely that in some experiments the initial stress is not maximum, although the fluid is strongly stretched before the beginning of the experiment.

Three different cases are illustrated in figure 4.21 which shows results from the model with different initial conditions: the full red symbols stand for a stretching phase beginning with a maximum stress, the pink symbols for the same stretching series with an intermediate initial stress and the empty symbols for a stretching phase beginning with a zero stress. The ratio  $G/\sigma_y$  is set to 0.5 in this figure and the geometry is filament-like. In the case of a zero or even intermediate initial stress, it is clear that even if the points seem nearly aligned, a positive y-intercept arises and the slope  $\Gamma_{app}^U$  decreases.

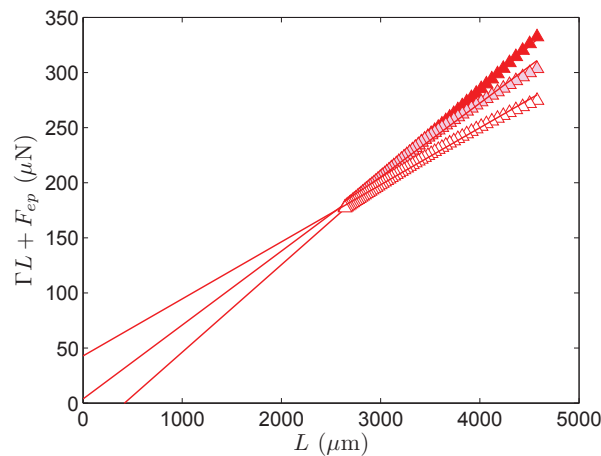


Figure 4.21 – Stretching phase in the filament geometry, with  $G/\sigma_y = 0.5$  and three different initial conditions. Solid red symbols: maximum initial stress  $T_0 = \sqrt{3}\sigma_y$ . Pink symbols: intermediate initial stress  $T_0 = \sqrt{3}/2\sigma_y$ . Empty symbols: zero initial stress  $T_0 = 0$ . Each set of points is shown with its linear fit.

The model shows that above a ratio  $G/\sigma_y \approx 8$ , the force- $L$  curves are not sensitive any more to the initial stress (see figure 4.15 for example) and the y-intercept of the stretching branch (red) is always negative.

For the carbopol samples we used, the ratio  $G/\sigma_y$  is comprised between 2.3 and 6.1. The curves are sensitive to the initial conditions. This explains the occurrence of positive y-intercepts for the stretching branch and also the dispersion in the limiting slopes values. However for our samples where  $G/\sigma_y > 5$  (HS carbopols), we could obtain force- $L$  plots with negative y-intercept and limited influence of initial stress, as predicted by the elastoplastic model (figure 4.22).

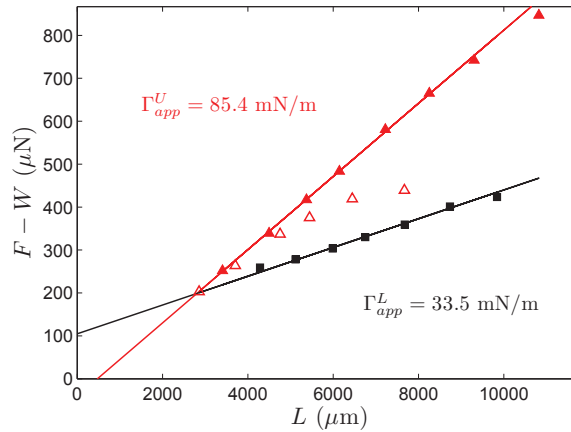


Figure 4.22 – Force- $L$  plot for carbopol 0.75% (HS) with  $G/\sigma_y = 5.1$ . From the second stretching branch (empty triangles) we see that the initial condition is quickly forgotten. The mean slope is 59.5 mN/m.

#### 4.5.4 Surface tension

**Measurement with the bridge tensiometer.** As can be seen in figure 4.12, left, for vanishing yield stress the upper and the lower slopes both tend to around 63 mN/m. This suggests that the surface tension of carbopol gels is close to this value. For higher values of the yield stress, our experiment clearly shows that the way an experiment is performed (ie. the fact that the yield stress fluid is stretched or compressed) influences a lot the value of the surface tension found via this experiment.

The bridge tensiometer setup provides a way to measure the surface tension of yield stress fluids with  $G \approx 8\sigma_y$  or more: on a force- $L$  plot the data align on two limiting curves which are symmetrical with respect to  $F - W = \Gamma L$ . The true value of the surface tension is thus the mean of the slopes of the two linear fits (equation 4.10). With the model, taking  $G/\sigma_y = 8$  in the filament geometry, the surface tension value could be recovered in this way within less than 1%. Note that the condition  $G/\sigma_y > 8$  is usually met in a large range of yield stress fluids like emulsions ( $G/\sigma_y \sim 10$  to 20) [103], clay suspensions ( $G/\sigma_y \sim 30$  to 1000) [37] and microgel pastes ( $G/\sigma_y \sim 15$ ) [24]. By this method and with our HS samples for which  $G/\sigma_y > 5$  we obtained as a maximal value for the mean slope 63.1 mN/m for 0.25% carbopol ( $\sigma_y = 4.6$  Pa) and 59.5 mN/m for 0.75% carbopol ( $\sigma_y = 15.6$  Pa).

**Ascending bubble measurements.** Our results with the bridge tensiometer are confirmed by other experiments with an ascending bubble setup (Teclis Tracker) and carbopols of very low yield stress ( $\sigma_y < 2$  Pa). Here again the apparent surface tension depends on the flow history.

The surface tension between carbopol and air was measured by injecting an air bubble in a large volume of very low yield stress carbopol ( $\sim 1$  Pa) and analyzing the bubble profile. The device has a built-in analysis program that fits the interface with a solution of Laplace's equation to determine  $\Gamma$ . At the beginning of each experiment, a given volume of air is injected in the fluid (corresponding to a given interface area  $A_0$ , calculated by the analysis program). Then a fixed interface area is imposed, either greater or smaller than  $A_0$ . The area remains then fixed thanks to a feedback loop during the whole measurement, which lasts for about 10 minutes each time. The surface tension is automatically recorded about every second.

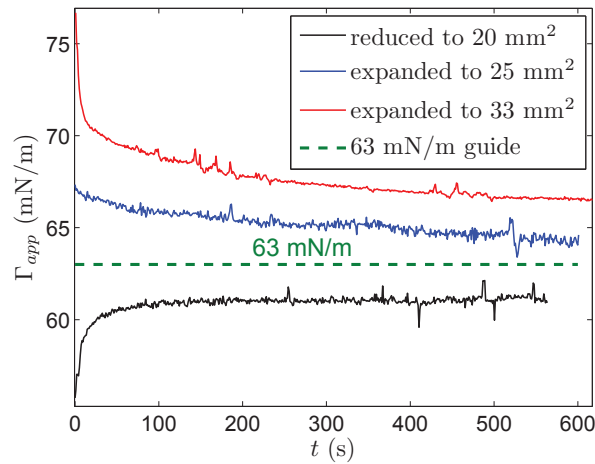


Figure 4.23 – Evolution of surface tension measured by an ascending bubble method, for a 0.25%(MS) carbopol of yield stress  $\sigma_y = 0.3$  Pa, after different changes in interface area at  $t = 0$ . Before  $t = 0$  the volume of the bubble is  $13 \mu\text{L}$  and its area is slightly less than  $25 \text{ mm}^2$ .

The evolution of the apparent surface tension is plotted in figure 4.23. A slow relaxation can be observed after the increase (resp. decrease) of the area of the bubble, at  $t = 0$ . The end value of the apparent surface tension is rather stable, but depends on the quantity of area added (resp. removed) at the beginning. Above all, it depends on the sign of the surface variation. We interpret this as an elastoplastic effect. More precisely, the interface first response is related to a bulk elastic deformation of the fluid, resulting in an increased (or decreased) apparent surface tension. The surface then evolves towards its equilibrium shape, but the yield stress prevents the system to reach equilibrium.

For a 0.25% MS carbopol of yield stress 0.3 Pa, the apparent surface tension after 10 minutes is between 61 mN/m and 66 mN/m, depending on the history of the bubble. For a 0.5% MS carbopol of yield stress 1.75 Pa, the apparent surface tension is between 59 mN/m and 65 mN/m.

This behavior can be compared to measurements with another polymer solution (poly-oxyethylene or POE) that does not have a yield stress. With this fluid, strongly viscoelastic, the drop profile is laplacian and the steady value of the surface tension does not depend either on the sign or on the amplitude of the surface variation.

The ascending bubble commercial device can however not be used for determining the surface tension of a wide range of carbopols, since it is not powerful enough to push a bubble in the

liquid when the yield stress is over 2 Pa. In addition, the apparent surface tension is extracted from a laplacian fit of the interface profile, although this condition may not be verified for yield-stress fluids.

**Comparison with other values.** The surface tension values found with the capillary bridge method are very consistent with most of the literature. For 0.25% carbopol, we find  $\Gamma \approx 63$  mN/m and around 59 mN/m for 0.75% carbopol. What is expected for a polymer solution in water is a decrease of  $\Gamma$  with concentration.

This was also observed by Manglik *et al.* [14], who measured the surface tension of Carbopol 934 solutions up to 0.2% in weight, with a maximum bubble pressure method. They did not neutralize their solutions, but the most concentrated could have a small yield stress, which is not taken into account. With their technique they obtain  $\Gamma \approx 69$  mN/m for 0.2% carbopol. The real value (after correcting the yield stress effects) is probably a little smaller. Moreover, Carbopol 934 does not contain the same additives as Carbopol ETD 2050, and this may be another explanation for the difference with our measurements.

Boujlel and Coussot found  $\Gamma = 66$  mN/m with a plate withdrawal method [1]. The value is a bit higher than our measurements, but given the present uncertainty on the results, the two conclusions are compatible.

Baudouin Géraud extracted a value of the capillary force  $\Gamma \cos \theta$  from capillary rise experiments [11]. They found  $\Gamma \cos \theta = 49$  mN/m. Their analysis included the effect of the yield stress and of the flow history, however this value cannot be compatible with  $\Gamma = 63$  mN/m unless the contact angle  $\theta$  is at least  $39^\circ$ . Yet the surfaces used by Baudouin were very clean and hydrophilic, so they expected the contact angle to be close to zero. This motivated a part of the experiments presented in the next chapter, especially at the end of the spreading. We also suspect an elastic deformation of the arrested meniscus, which would increase the contact angle. It would be interesting to be able to measure precisely the contact angle in the channel at the end of the capillary rise.

Additionally, I had the opportunity to do surface tension measurements at the ESPCI in Paris in June 2014. Laurence Talini kindly introduced me to her surface fluctuation specular reflection (SFSR) spectroscopy setup [44]. I could use this setup to measure carbopol surface tension by a very different method. In particular, SFSR does not rely on force measurements, and the triple line is far enough from the measurement spot to neglect boundary effects. These measurements are described in annex C.

## 4.6 Conclusion

In this chapter, I introduced the capillary bridge setup and the measurements of the adhesion force of capillary bridges. This setup provides a precise method to measure the surface tension of simple fluids. The case of yield-stress fluids is more complicated but the experiments highlighted several important points, specific to these fluids. Our analysis of the results and the development of a model allowed us to propose a reliable method to measure the surface tension of yield-stress

fluids. In addition, we could reconcile the various results found in the literature.

First, it appeared that the existence of the yield stress introduced extra forces in the adhesion, even at rest. Reducing the size of the system reduced a little the effect of yield stress on the adhesion force, but never enough to be able to neglect it. These forces could be computed in simplified geometries, specially chosen to be able to define the stress field everywhere in the fluid system. We could also evidence the influence of the fluid elasticity when the deformation is less than the critical yielding strain. Our elastoplastic model allowed us to underline the crucial importance of the deformation history for the stress repartition and magnitude, which impacts directly the elastoplastic force and thus the adhesion. The practical consequences for surface tension measurements are that yield stress, elasticity and flow history all have an influence on the measured value.

These ideas are characteristic of yield-stress fluids and more general than the capillary bridge framework. In all experiments involving yield-stress fluids, apart from steady flow situations, the yield stress, the fluid elasticity and the flow history must be taken into account.

## 4.7 Perspectives

**Setup improvements.** A few adjustments can be made on the capillary bridge tensiometer. First, the top plate, for the moment a small square piece of flat glass, should be replaced by a small glass lens. This would avoid a potential deformation of the contact line at the surface edges when the liquid spreads a lot. A spherical shape also solves problems with the parallelism of the surfaces and makes it easier to control the position of the bridge. It would also allow to vary the drop volume. For the moment, the contact area of a large drop is limited by the edges of the square surface, but a small drop, if it spreads completely, creates such a large adhesion force that the surfaces cannot be separated at all. For this reason, the volume of the bridges is controlled by the size of the top surface. Then, temperature and humidity should be controlled to minimize both sensor drift and evaporation. This means that the box containing the setup has to be closed, which complicates the deposition of the drop between the surfaces. Finally, the experiment would benefit from being fully automated with Labview.

**Curvature oscillations.** The method used to compute the surface curvature is not perfect, because the polynomial fit of the profile generates oscillations after differentiation. I have tried to extract the surface tension of the simple fluids by fitting the curvature  $C(z)$  curve. As already mentioned in section 4.2, for simple fluids this curve is expected to be a straight line with a slope  $\rho g/\Gamma$ .  $\rho$  and  $g$  are known, so  $\Gamma$  can be calculated from the slope. Unfortunately, the oscillations induce a large uncertainty on the slope of the fit, so the values found for  $\Gamma$  are not reliable.

However, two interesting points deserve to be examined further. The first point is that the values of  $\Gamma$  extracted from the slope of  $C(z)$  are not randomly dispersed. They are clearly correlated with the deformation direction (figure 4.24), especially when contact angle hysteresis is large. This suggests that the line pinning constraints the shape of the surface so much that the inner pressure cannot be hydrostatic any more.

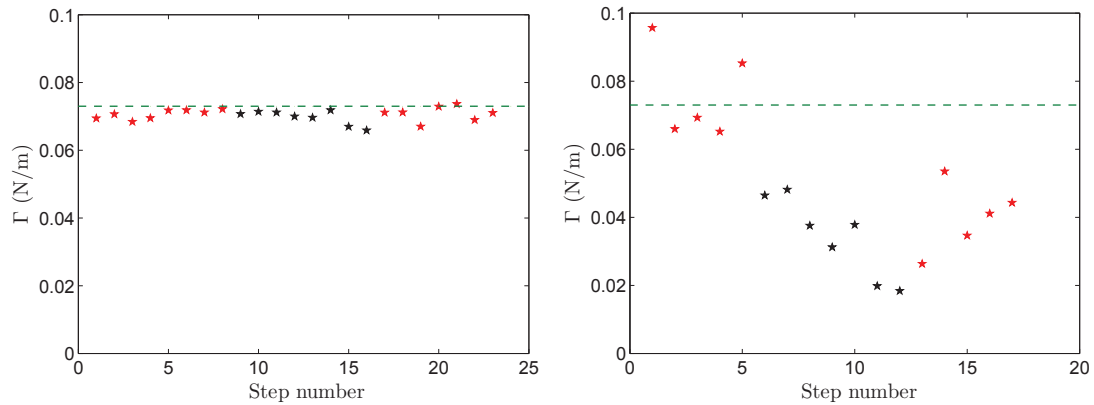


Figure 4.24 – Surface tension values  $\Gamma$  calculated from the slope of  $C(z)$ , for each step, with water bridges. The red symbols stand for stretching steps and the black ones for compression steps. The dashed line is the expected (tabulated) surface tension. Left: water on very clean and hydrophilic glass (contact angle range:  $5^\circ$ ). Right: water on polluted glass (contact angle range:  $25^\circ$ ).

The second point is that in spite of the oscillations, we can clearly see that  $C(z)$  is not linear at all in carbopol bridges (figure 4.25). There is a minimum at the neck position. This minimum is not detectable at the first step but it grows during the stretching series. It is a reflect of the inner stress. We can assume that at the neck the depth of the minimum is proportional to  $\sigma_{rr}$ . What is surprising is that during the compression, we expect this minimum to reverse and become a maximum (because in the filament model the radial stress should be  $\sigma_{rr} = u/r$ ). Instead of that, the amplitude of the minimum remains constant. It suggests that there is no flow near the neck during compression. This may be linked to wall slip, because the glass surfaces are smooth. The experiment could be tried with rough glass.

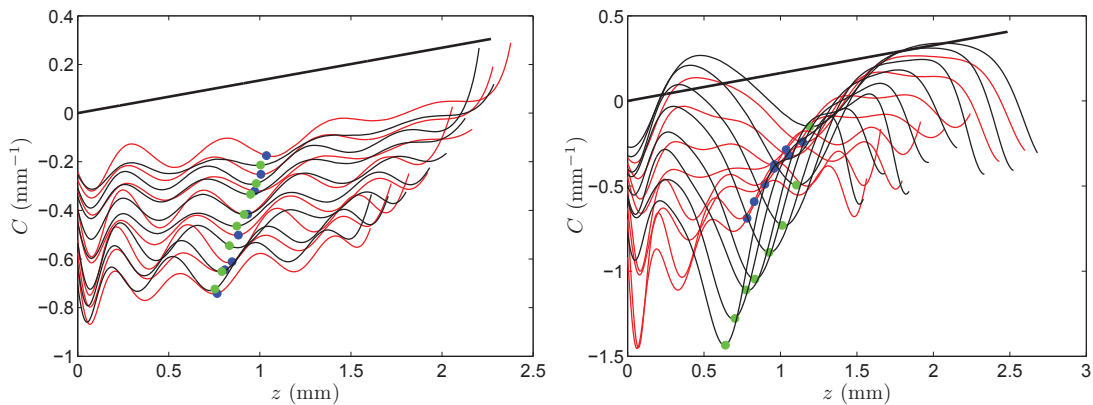


Figure 4.25 – Curvature  $C$  plotted along  $z$  for each step. Left: water bridge on clean glass. Right: carbopol bridge on clean glass. The red curves are for stretching steps and black ones for compression steps. The black line is the slope corresponding to hydrostatic pressure in the liquid. The dots materialize the position of the neck. Note that the first stretching step corresponds to the lowest curve (smallest mean curvature), as well as the last compression step. This means that the average pressure increases with stretching, which is counterintuitive.

**Contact angle.** With carbopol, the contact angle varies sensibly during the experiment, even on very clean and hydrophilic glass. The hypothesis that the spreading is hindered by the yield stress was confirmed later. This point is discussed at the end of chapter 5. But it is not clear whether this effective contact angle hysteresis has the same effect on the force- $L$  curves as real wetting hysteresis with simple fluids, as described in section 4.2. In any case, the force hysteresis cannot be due only to contact angle hysteresis, as the maximum  $\Delta\Gamma$  measured with water with a strong line pinning is smaller than most of the  $\Delta\Gamma$  measured with the yield-stress fluid.

**Stress relaxation and creep.** During the experiments, I noticed that the force drifted slowly even after a long waiting time (several minutes), as can be seen on figure 4.5. I first attributed this to evaporation, because it appeared also with water sometimes. But after questions from a referee for our article [104], we examined the relaxation of shear stress in a rheometer (see chapter 3), where the stress geometry is much simpler than in capillary bridges. The behavior of the stress is very similar to the force evolution in the tensiometer (figure 4.26). It is thus possible that part of this evolution is creep.

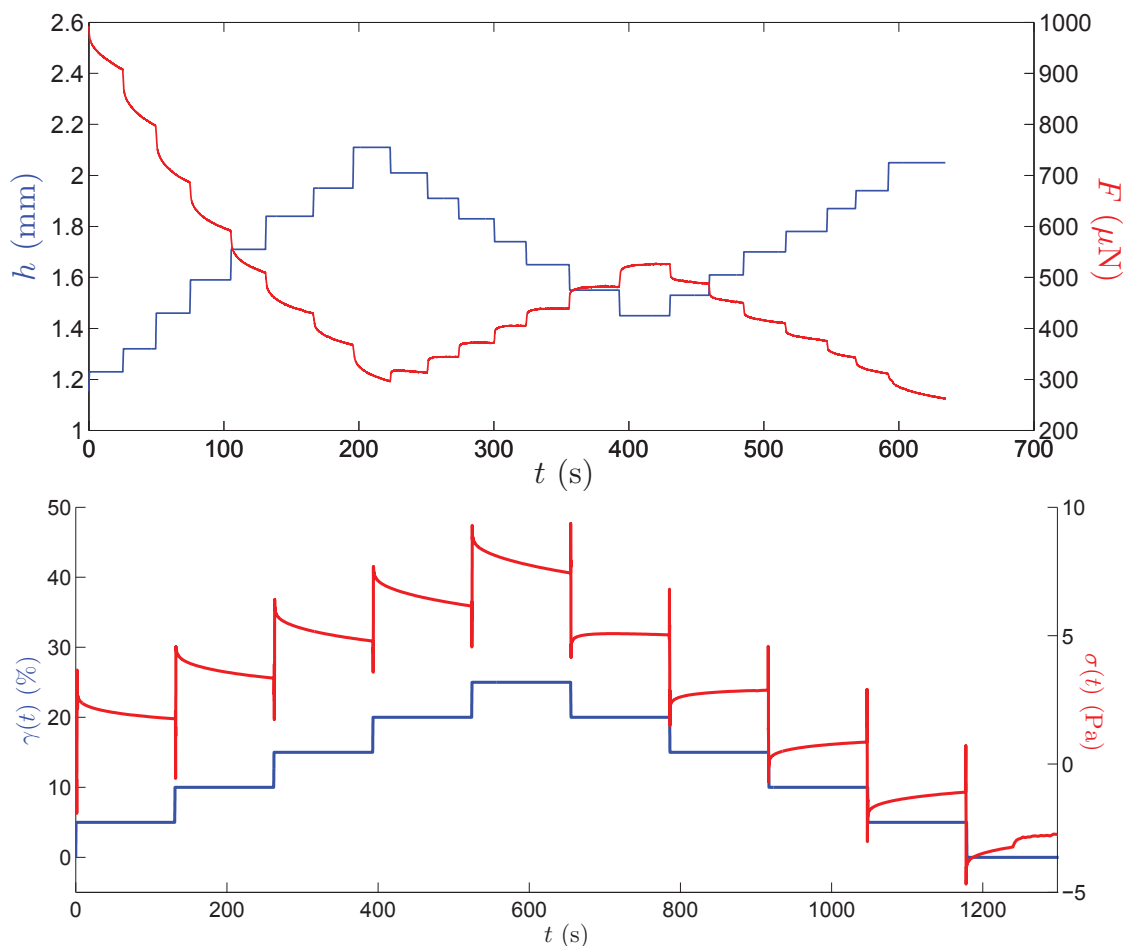


Figure 4.26 – Top: height  $h$  of the bridge (blue) and corresponding adhesion force  $F$  evolution (red) in time. Bottom: same figure as 3.4 in chapter 3. The blue line is the deformation amplitude and the red line is the stress response in time.

# Chapter 5

## Spreading of yield-stress fluid drops

### Contents

---

<b>5.1</b>	<b>Experiments at short timescales</b>	<b>96</b>
5.1.1	Setup and protocol	96
5.1.2	Observations	99
	Simple fluids	99
	Complex fluids	101
5.1.3	Model and discussion	104
5.1.4	Conclusions	106
<b>5.2</b>	<b>Experiments at long timescales</b>	<b>108</b>
5.2.1	Setup and protocol	108
5.2.2	Radius evolution in time	110
5.2.3	Final contact angle	114
	Setup	114
	Influence of the yield stress	116
	Influence of wall slip	117
5.2.4	Conclusions	118

---

The second main part of the work bears on spreading of complex fluids. The motivation was to understand why a yield-stress fluid drop never spreads completely, even on a very wetting surface, and to rationalize the real contact angles observed with yield-stress fluids. It seemed also interesting to explore the effects of the yield stress on the spreading dynamics. This work continues the path of Baudouin Géraud's thesis on confined flows and capillary rise of yield-stress fluids. The first part, on carbopol surface tension, allowed us to compare his value of the capillary force  $\Gamma \cos \theta$  to a value of  $\Gamma$  obtained independently. The second part, as I will show now, allowed us to investigate  $\cos \theta$ . Moreover it raised new issues on the dynamical effects due to the friction of the contact line on the surface imperfections and on their similarity with yield-stress effects.

Three regimes are generally distinguished in drop spreading: an inertial regime, a gravitational regime and a capillary regime.

The inertial regime is the first one and does not last more than a few milliseconds. It results from a balance between the capillary force and the inertial part of the line acceleration. In this regime viscosity should not play any role [32].

The gravitational regime follows the inertial regime, until the center of mass of the system does not move any more. It corresponds roughly to the moment where the height of the drop reaches the capillary length. It results from a balance between the gravitational energy loss and the viscous dissipation near the line.

The last regime is known as the capillary regime. Inertia and gravity do not play a role any more. The energy balance is between the surface energy gain and the viscous dissipation.

I made experiments on the one hand on the inertial and gravitational regimes, and on the other hand on the capillary regime. Two different setups were used to get the best precision on the radius in each case.

Some experiments were made, under my supervision, by Antoine Vitté, a L3 student, during his internship in the lab, and by Jérémy Auffinger and Aurélien Valade, also L3 students, during practical classes. This was a good opportunity for me to learn about students supervision, and the quality of their work was so good that I could use some of their results.

## 5.1 Experiments at short timescales

### 5.1.1 Setup and protocol

The short timescale experiments are performed in a side-view setup with a fast camera (figure 5.1).

A drop of fluid is slowly pushed at the tip of a metal flat-end needle attached to a vertical syringe. This syringe is fixed above a wetting surface placed on an horizontal stage. The height of the needle is adjusted in order that the drop detaches when its bottom nearly touches the surface, so that it falls with the smallest velocity attainable. For very wetting fluids (such as surfactant solutions), the metal needle was coated with Teflon. For yield-stress fluids, effective viscosity at low flow rate is too high to use a small capillary and a syringe needle. These are then replaced by Tygon tube (inner diameter 2.4 mm) and a polypropylene micropipette tip, because carbopol drops detach easily from these tips.

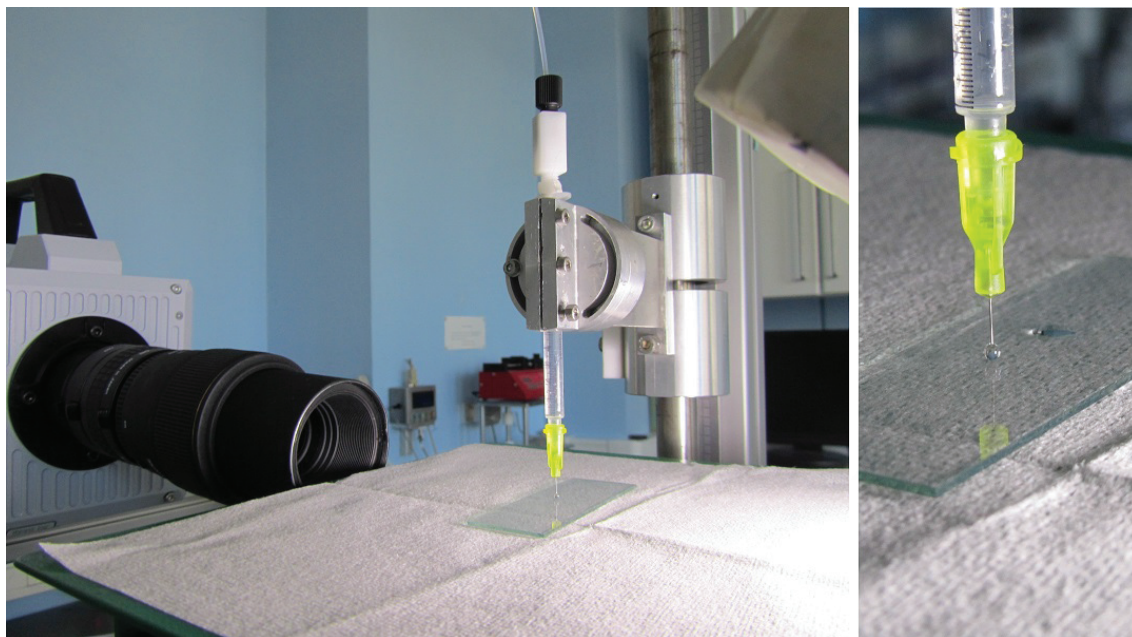


Figure 5.1 – Picture of the setup for spreading at short timescales.

The contact event is recorded with a fast camera Photron (Fastcam SA4) equipped with a 105 mm EX Sigma objective and 56 mm of extension tubes. The camera is installed close to the drop, with the objective end at approximately 10 cm from the needle tip, to get a very high magnification. It is slightly tilted with respect to the horizontal direction ( $5^\circ$ ) to have a good view on the contact line without too much distortion.

In this section I present measurements of the contact radius as a function of time for different fluids: simple fluids (pure water, surfactants in water and glycerin-water mixture), shear-thinning dilute polyacrylic acid solutions and carbopol gels. The wetting surfaces are clean hydrophilic glass microscope slides, generally smooth if nothing else is mentioned. They are rubbed with soap under hot tap water, then rinsed with ethanol and deionized water and finally made hydrophilic in a plasma cleaner (Harrick) during 5 minutes. The glass is cleaned the same day as the measurement and kept in closed disposable Petri dishes before being used.

When the setup is ready, a glass slide is taken from a Petri dish and carefully placed on the horizontal stage. A drop is pushed very slowly by hand (approximately one minute per drop). When it touches the surface, the film is triggered. At the image rates used (between 10000 fps and 50000 fps) the available time is not more than a few seconds. Then the whole film is saved for future analysis. A few snapshots of a typical film are shown in figure 5.2.

The velocity  $V_0$  at  $t = 0$  (instant of contact) has been checked and it is always less than  $10 \mu\text{m/s}$ . This way the kinetic energy is reduced.

In some experiments the metal tip is electrically charged, especially when the weather is dry, and the liquid is attracted by the hydrophilic surface (figure 5.3). As I found out later, this accelerates the spreading and should be avoided, for example by replacing the metal needle by a plastic needle (or pipette tip) or by touching the needle to discharge it before making a drop.

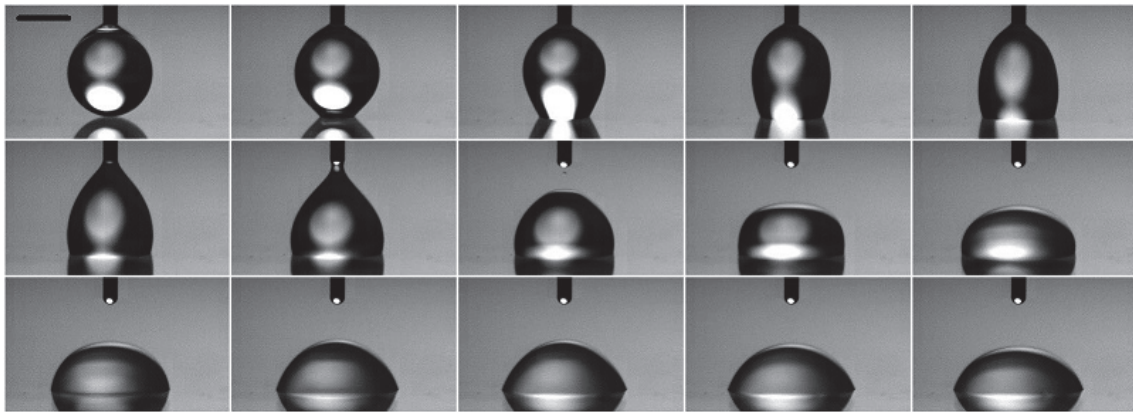


Figure 5.2 – Typical spreading of a simple liquid (60% glycerin in water). The scale bar represents 1 mm. The time interval is  $\Delta t = 1$  ms.

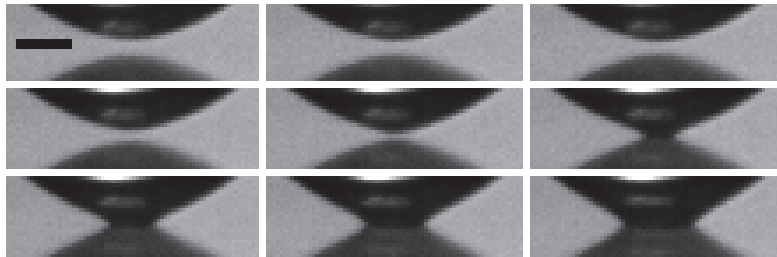


Figure 5.3 – Contact when the metal needle is charged. The bottom of the drop looks like it is sucked by the glass slide. The time interval is  $\Delta t = 100$   $\mu$ s and the scale bar represents 200  $\mu$ m.

**Film processing.** The film is processed with ImageJ. A straight line is drawn by hand on the contact position and the image stack is resliced along this line. This gives directly the evolution of the contact radius in time (figure 5.4). Then the outline of this picture is detected with Matlab. The curve of radius  $R$  versus time  $t$  has two regimes that are clearly distinguished when plotted in log-log scale. The first regime is fitted with a power law to retrieve the exponent.

This exponent is then compared to existing models.



Figure 5.4 – Example of a resliced film (truncated to 1500 images after contact). The film is the same as in figure 5.2. The vertical bar stands for 1 mm and the horizontal one for 1 ms.

**Estimation of errors.** The first sources of error are the image resolution and the sharpness of the drop silhouette at the level of the contact line. The Matlab function “edge” is used on the resliced film with two different methods: ‘Laplacian of gaussian’ for the first 200 images (to avoid possible noise) and ‘Canny’ for the rest of the film (to detect weaker edges). This way the

contact radius is estimated with an error of about 1 pixel ( $\approx 15 \mu\text{m}$ ).

The very first images after contact have a larger error because the contact area is shaded by the drop (see figure 5.5). This issue is also raised in a paper by Eddi *et al.* [33] and they suggest an alternative setup with a bottom view to track the contact radius below the detection limit of the side view. We do not use the bottom view because our camera is not fast enough to get many images below this threshold. But the fits do not take into account the first 5 points.

The estimation of the precise contact time  $t_0$  is also difficult because of this shading. It is yet crucial because an error of 1 image ( $20 \mu\text{s}$ ) on  $t_0$  induces an error of about 2% on the power law exponent. The uncertainty on  $t_0$  can reach  $\pm 5$  images if it is determined from the film. To help the eye, I determine  $t_0$  from the resliced film. This reduces the uncertainty to  $\pm 1$  image (see figure 5.5).

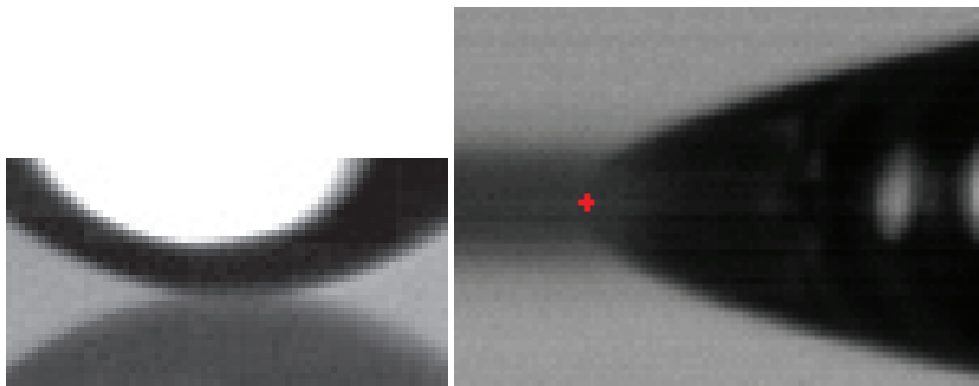


Figure 5.5 – Left: zoom on the contact at  $t_0$ . The radius is not well defined at this instant. Right: zoom on the resliced film around  $t_0$ . The estimated  $t_0$  is represented by a red cross. One pixel is about  $15 \mu\text{m}$ .

The fit is a linear least squares fit on  $\log(t)$  and  $\log(R)$ . The error indicated on the figures is the confidence interval returned by the fitting function. It is generally of the order of 0.001.

As the number of identical experiments is about 10 to 15 for each fluid, the standard deviation of the exponents distribution is computed as well. It is always higher than the uncertainty on the fit, which is not surprising because I expect the dispersion of the values to be due in a large part to the determination of  $t_0$ . Physical effects such as wetting imperfections or electrostatic interactions can also affect the dispersion. The electrostatic artifact is discussed in the following paragraph.

## 5.1.2 Observations

### Simple fluids

To check the protocol I started the experiments with simple fluids: pure water, a surfactant solution (SDS, 7 mM), a mixture of glycerin and water (60% glycerin - 40% water, mass fraction) and silicone oil (M1000 from Roth).

The experiments with silicone oil are not exploitable because the liquid completely wets the needle before falling with a noticeable velocity.

For all three other fluids, the curve  $R(t)$  is well fitted with a power law up to a few milliseconds (example figure 5.6). The exponent of the power law is always close to 0.5. The mean and standard deviation of the exponents for each fluid are presented in table 5.1.

The exponent tends to be higher for the surfactant solution than for pure water and glycerin mixture: this is probably due to electrostatic interactions, as described in the previous section, because the metallic needle is often electrically charged. I visually noticed a clear correlation between “surface sucking” (figure 5.3) and increased exponents (sometimes more than 10%). In practice I only take into account for the mean the experiments where the sucking effect is visually unnoticeable, but electrostatic effects could be present even if not visible.

Liquid	mean( $p$ )	std( $p$ )	#
Pure water	0.494	0.009	12
Glycerin mixture	0.505	0.010	10
Surfactant solution	0.518	0.002	9

Table 5.1 – Power law exponents for the simple fluids. mean( $p$ ) is the mean, std( $p$ ) the standard deviation and # the number of experiments included in the mean.

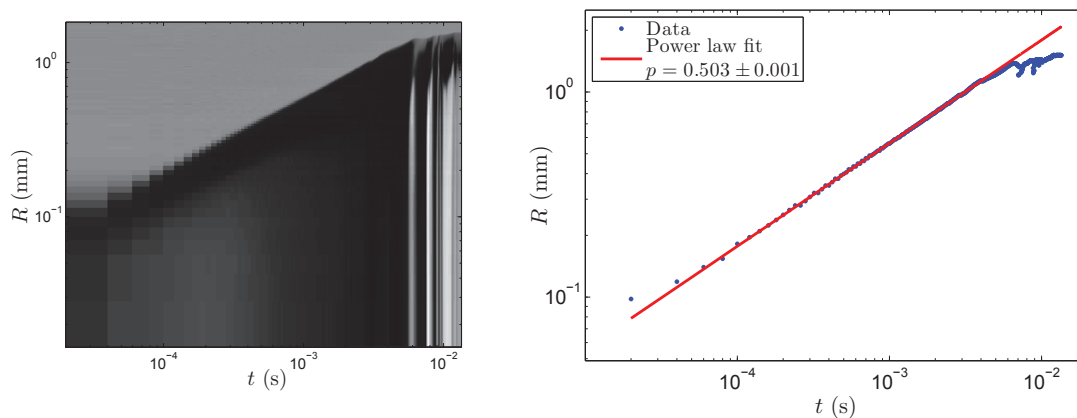


Figure 5.6 – Left: log-log spatio-temporal representation of the contact radius in time. Right: log-log plot of the contact radius in time. Pure water on hydrophilic glass.

A troubling feature of the short-time spreading of simple fluids is the duration of the  $p = 0.5$  regime. Indeed the inertial model used to predict this exponent (see sections 1.3.1 and 5.1.3) is valid only while the contact radius is smaller than the drop initial radius. Experimentally, we see on the images that the  $p = 0.5$  regime lasts much longer than this condition (figure 5.7). The two top pictures correspond respectively to  $t = 1$  ms for a water drop of initial radius  $R_0 = 0.6$  mm (left) and  $t = 3$  ms for a water-glycerin mixture drop of initial radius  $R_0 = 0.85$  mm (right). The two bottom pictures correspond to the same drops at the end of the  $p = 0.5$  regime, here  $t = 6$  ms for water and  $t = 10$  ms for glycerin.

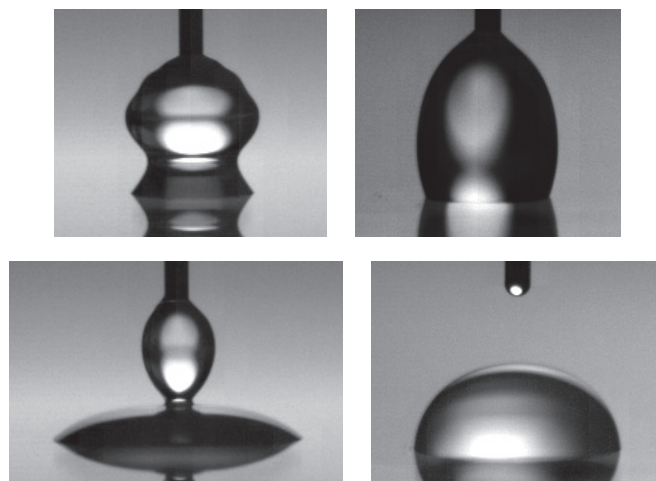


Figure 5.7 – Left: water drop at  $t = 1$  ms (end of the inertial model validity) and  $t = 3$  ms (end of the  $p = 0.5$  regime). Right: water-glycerin mixture drop at  $t = 3$  ms and  $t = 10$  ms.

### Complex fluids

I did experiments with neutralized polyacrylic acid (PAA) solutions of different concentrations in water (ranging from 0.1% to 3%, weight fraction) and with carbopol. I used a relatively short polyacrylic acid ( $M_w = 450000$ ). PAA and carbopol have the same chemical composition but PAA is not crosslinked and the molecules are not too long, so that it does not gel, even at neutral pH. This allowed me to compare carbopol with a chemically similar fluid, viscoelastic but without yield stress. The idea was to distinguish the effects due to the yield stress from the effects due to the fluid elasticity.

**PAA solutions rheology.** From a rheology point of view, PAA solutions are shear-thinning, without yield stress, and viscoelastic. Their flow curves can be fitted by a power law  $\sigma = K\dot{\gamma}^n$ . For the viscoelastic moduli, a simple Maxwell model with a spring of elasticity  $G$  and a dashpot of viscosity  $\eta$  is well adapted to dilute polymer solutions. It predicts:

$$G' = G \frac{\omega^2 \tau^2}{1 + \omega^2 \tau^2} \quad (5.1)$$

$$G'' = G \frac{\omega \tau}{1 + \omega^2 \tau^2} \quad (5.2)$$

where  $\tau = \eta/G$  is the characteristic viscoelastic time of the model. However, the model does not fit the storage modulus data, because of rheometer inertia effects. This inertia, in a controlled-stress rheometer, can lead to a relatively strong deviation of the storage modulus  $G'$  and to the absence of a plateau at high frequency [105]. Some experimental curves are presented along with the Maxwell model curves in figure 5.8. We can see that the  $G'$  curve is very different from Maxwell model. The  $G''$  curve is better fitted by the model, but the inertia artifact also impacts  $G''$  at high frequency and the rheometer is not designed to measure viscoelastic moduli at such frequencies.

For this reason, to determine  $\tau$ , I use the maximum of  $G''$  (at this point  $\omega\tau = 1$ ) and not the crossing of  $G'$  and  $G''$ , which is strongly shifted. I get  $\tau \approx 5$  ms ( $\pm 20\%$ ) for all concentrations.

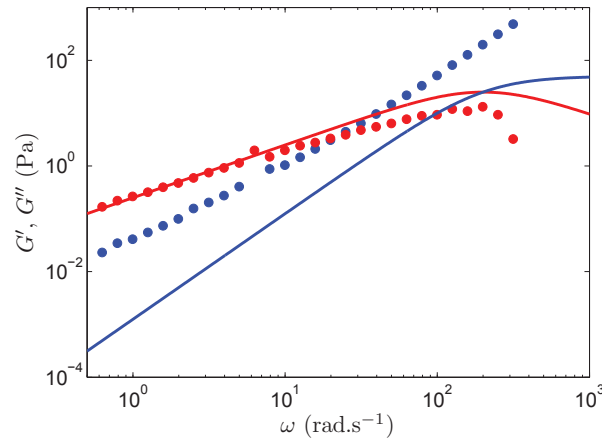


Figure 5.8 – Experimental viscoelastic moduli for a 1% PAA solution (dots). The blue (respectively red) dots are experimental values of  $G'$  (respectively  $G''$ ). Corresponding Maxwell model (lines) for the values  $\tau = 5$  ms and  $G = 50$  Pa measured as explained in the text. We can see the strong deviation of  $G'$  with respect to the model, due to inertia artifacts.

Then I determine  $G$  from the value of  $G''$  at  $\omega = 1$  rad s<sup>-1</sup>. The uncertainties on  $\tau$  and  $G$  are quite high, and the measurement had to be repeated many times before getting exploitable data.

Table 5.2 shows the parameters  $K$  and  $n$  measured for each PAA concentration in steady shear mode, and the values of  $G$ .

Concentration	$K$ (Pa.s <sup>n</sup> ) ±5%	$n$ ±1%	$G$ (Pa) ±10 Pa
0.1%	0.069	0.80	10
0.2%	0.110	0.79	17
0.5%	0.175	0.81	26
1%	0.40	0.80	50
2%	0.90	0.76	110
3%	1.58	0.74	210

Table 5.2 – Rheology parameters of the PAA solutions. The parameters  $K$  and  $n$  are measured in steady shear mode and  $G$  is extracted from the linear oscillation measurements.

**PAA spreading** Again, the gravitational regime can be fitted by a power law of exponent  $p$  (figure 5.9). However, contrary to simple fluids,  $p$  deviates sensibly from 0.5. Even at low polymer concentration the exponent is only  $p \approx 0.46$  and when the concentration increases,  $p$  decreases. The evolution of the measured  $p$  with concentration is shown in figure 5.10. For the concentration  $C = 3\%$ , the square point takes into account all experiments where no electrostatic effect can be seen. However the exponent increases regularly from 0.327 to 0.372 from the beginning of the series to the end. For this reason, I also indicated with a dashed line the value obtained by averaging only the first 5 experiments of the series (out of 15).

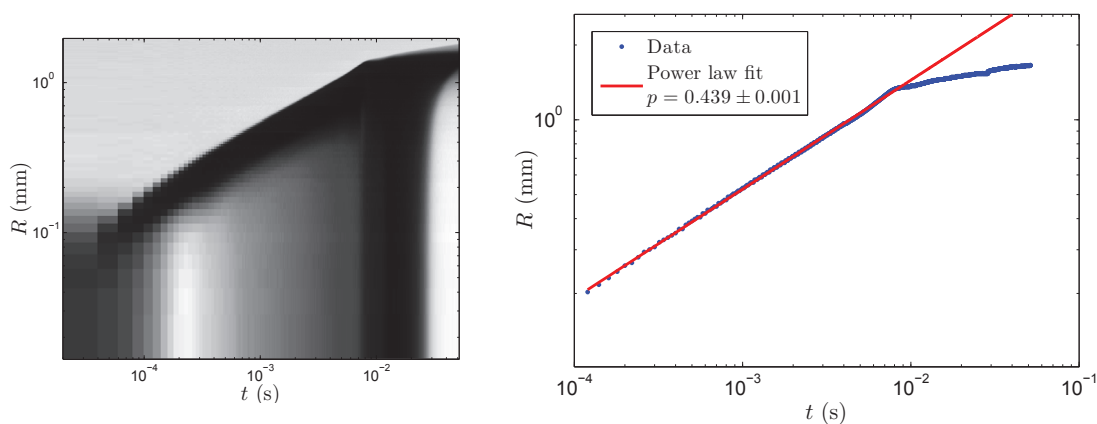


Figure 5.9 – Left: log-log spatio-temporal representation of the contact radius in time for a 0.5% PAA solution of elastic modulus  $G = 26$  Pa. Right: plot of the contact radius in time (log-log scale). The red line is the power law fit. The exponent is given in the legend.

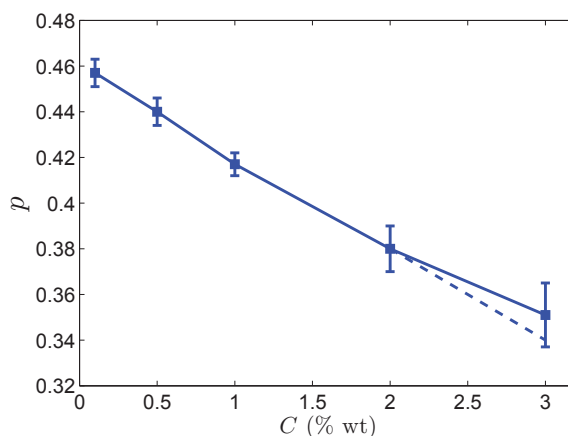


Figure 5.10 – Evolution of the spreading exponent  $p$  of viscoelastic PAA solutions with polymer concentration. Error bars stand for the standard deviation of the exponent distribution. The dashed line represents the evolution if I take into account only the 5 first experiments at  $C = 3\%$  (see text).

**Carbopol spreading** With carbopol,  $R(t)$  deviates a little from a power law (figure 5.11). However, two regimes can still be identified. To characterize the short time spreading dynamics, the end of the first regime (around 10 ms) is fitted with a power law. The exponents of this power law are rather reproducible. They are given in table 5.3 along with the rheological properties of the carbopols used.

Carbopol	$\sigma_y$ (Pa)	$K$ (Pa s $^n$ )	$n$	$G$ (Pa)	$p$
MS 0.5% ETD	3.3	3.2	0.54	18	$0.353 \pm 0.007$
HS 0.5% ETD	8.7	7.8	0.49	45	$0.326 \pm 0.006$

Table 5.3 – Rheological parameters and average spreading exponent of the two carbopols used in short timescale spreading experiments.

The most probable is that the spreading exponent could decrease because of elasticity, since

it has been shown above that a viscoelastic fluid without yield stress has a spreading exponent smaller than 0.5. However, it is not possible to compare quantitatively the elasticity of PAA solutions and carbopol, because the evolution of  $G'$  and  $G''$  with frequency are very different. Indeed, for PAA solutions,  $G$  is extracted from a Maxwell model. For carbopol, it is the value of the  $G'$  plateau at low frequency, in the linear regime (figure 3.2 of chapter 3).

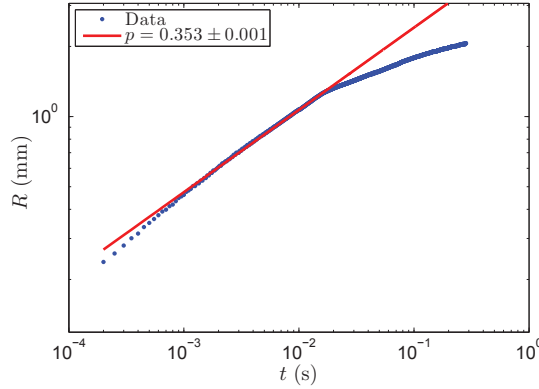


Figure 5.11 – Contact radius in time (log-log scale) for MS 0.5% carbopol of yield stress  $\sigma_y = 3.3$  Pa and elastic modulus  $G = 18$  Pa. The red line is the power law fit. The exponent is given in the legend.

### 5.1.3 Model and discussion

In this section, I develop a dimensional model inspired by the work of Bianco *et al.* [32], who studied the first regime of spreading of a liquid drop. Our model explains the evolution of the contact radius  $R$  in time and the exponents found for simple and complex fluids at short times.

As shown by Bianco, the first moments of the spreading of a low viscous drop involve the surface tension as a driving force and inertia as a brake. The capillary power can be written dimensionally as

$$P_c \sim \Gamma \frac{d}{dt} (R^2) \sim \Gamma \dot{R} R \quad (5.3)$$

On the other hand, the kinetic energy variation is due to the velocity of the line  $\dot{R}$  and to the variation of the mass  $m$  involved in the spreading. At the beginning of the spreading, this mass can be approached by  $\rho R^2 h = \rho R^2 / \kappa$  where  $h$  is the thickness of the spreading meniscus and  $\kappa$  is the curvature of the surface. A geometrical relation gives  $\kappa \sim R_0 / R^2$  with  $R_0$  the initial radius of the spherical drop. Then, the kinetic energy variation can be written as

$$\frac{dE_c}{dt} \sim \frac{d}{dt} \left( \frac{\rho}{R_0} \pi R^4 \dot{R}^2 \right) \quad (5.4)$$

These quantities must be equal at all times. We know that the solution  $R(t)$  is a power law, so  $R$  and  $\dot{R}$  are replaced respectively with  $At^p$  and  $pAt^{p-1}$  in expressions 5.3 and 5.4. This results in a left member (inertia) proportional to  $t^{6p-3}$  and a right member (capillarity) proportional to  $t^{2p-1}$ . Finally

$$p = 0.5 \quad (5.5)$$

But in the experiments with complex fluids I observe an exponent  $p$  smaller than 0.5 and decreasing with polymer concentration. The most natural ingredient that one can think of as a brake is viscosity. However the fluid viscosity  $\eta$  does not appear in the previous equations.

Actually, viscous dissipation can also play a braking role in spreading. It is already known at long timescales, in Tanner's law, but it is generally neglected at short timescales. First I will show that one also finds an exponent  $p' = 0.5$  for simple fluids if the driving power is gravity and the brake is viscous dissipation. Then I will define a criteria that separates the inertial regime from the gravitational regime. Finally I will adapt the model to apply it to a shear-thinning fluid.

The difficulty with viscous dissipation is that it is well known in a wedge with a small angle  $\theta \ll 1$ , but much less when the angle is close to  $\pi/2$ , as it is the case in my experiments. I will express this dependency via an unknown function  $f(\theta)$  which tends to  $1/\tan \theta$  at small  $\theta$  and is of the order of 1 for  $\theta \approx \pi/2$ . Then viscous dissipation is

$$P_v \sim \eta \dot{R}^2 R f(\theta) \quad (5.6)$$

The variation of potential energy of the drop is

$$\frac{dE_p}{dt} = Mg z_G \dot{z}_G \quad (5.7)$$

where  $M$  is the mass of liquid in the drop and  $z_G$  the altitude of the center of mass. The geometry is too complicated to express  $z_G$  exactly. But dimensionally, the only velocity in the problem is  $\dot{R}$ . Moreover the volume of a sphere portion is  $V = \frac{\pi}{2} H \left( \frac{H^2}{3} + R^2 \right)$  with  $H$  the total height of the sphere portion. Because the volume of the drop  $V$  is constant, after derivation this gives  $\dot{H} = \frac{-2RH}{R^2 + H^2} \dot{R}$ . Finally  $\frac{RH}{R^2 + H^2}$  is of the order of 1 and  $z_G$  is not very different from  $H/2$ .

Therefore we can reasonably write

$$\frac{dE_p}{dt} \sim -Mg \dot{R} \quad (5.8)$$

If we equate 5.6 and 5.8, injecting a power law  $R(t) = Bt^{p'}$ , we find:

$$p' = 0.5 = p \quad \text{and} \quad B = \sqrt{\frac{Mg}{\eta}} \quad (5.9)$$

Finally, we see that for simple fluids, the spreading exponent is the same ( $p = p' = 0.5$ ) whatever the regime (inertial or gravitational). The idea is summed up in table 5.4.

Regime	Driving power	Brake	Simple fluids spreading exponent
Inertial	Capillarity	Inertia	$p = 0.5$
Gravitational	Gravity	Viscosity	$p' = 0.5$

Table 5.4 – Recapitulation of the main ingredients of the two possible initial regimes and of the corresponding spreading exponent for simple fluids.

Now let us determine a criteria to know if the observed regime is inertial or gravitational. This transition occurs when the driving powers are of the same order of magnitude, that is to

say the variation of gravitational energy (equation 5.8) is of the same order of magnitude as the capillary power (equation 5.3). If we write the mass of the drop  $M = \rho R_0^3$ , the equation is

$$\rho g R_0^3 \dot{R} \sim \Gamma R \dot{R} \quad (5.10)$$

$$R \sim R_0 \left( \frac{R_0}{l_c} \right)^2 \quad (5.11)$$

where  $l_c = \sqrt{\Gamma/\rho g}$  is the capillary length, which is approximately  $l_c = 2.5$  mm for the liquids I used. As  $R_0$  is of the order of 1 mm in my experiments, the inertial regime is valid until  $R \sim 0.16$  mm. On the films and on the  $R(t)$  curves, we see that the inertial regime does not last more than 0.1 ms in our case. As the data below 0.1 ms are anyway not reliable because of the time and space resolutions, what we see is necessarily the gravitational regime. Moreover, from the films it is clear that the center of mass of the drop is falling. This also explains why we observe a power law of exponent 0.5 for a much longer time than predicted by the inertial model.

What we see is thus the gravitational regime and this regime includes a viscosity part. For simple fluids we recover an exponent  $p' = 0.5$ . Now this can be a basis for shear-thinning fluids. Here I use a rough approximation: the viscosity  $\eta$  is considered as an effective viscosity depending on  $\dot{R}$  with the same power law as the flow curve. Moreover, for yield-stress fluids, the yield stress itself is neglected because the shear rate is large enough to have  $K\dot{\gamma}^n \gg \sigma_y$ .  $\eta$  is then replaced with  $K_{\text{eff}}\dot{R}^{n-1}$ . If  $R$  is expressed as a power law of time with an exponent  $p'$ ,  $\dot{E}_p \sim t^{p'-1}$  and  $P_v \sim t^{3p'-2-(n-1)(p'-1)}$ . It finally yields

$$p' = \frac{n}{n+1} \quad (5.12)$$

PAA's flow curve exponent is between  $n = 0.74$  and  $n = 0.80$ , so from this model we expect a spreading exponent between  $p' = 0.425$  and  $p' = 0.444$ . The experimental values (figure 5.10) are between  $p' = 0.34$  and  $p' = 0.46$ . For carbopol, the agreement is even more striking. The flow curve exponents are  $n = 0.54$  and  $n = 0.49$ , which correspond to  $p' = 0.351$  and  $p' = 0.329$ , and we find experimentally  $p' = 0.353$  and  $p' = 0.326$ . Given the approximations, the model is very consistent with the experimental results.

The drawback is that it does not explain why the exponent decreases with concentration. In my opinion it is due to the fact that it includes a rheological ingredient ( $n$ ) related to flow curves, that is to a stationary flow. It does not take into account the elasticity  $G$  of the fluid, which though plays a strong role in the transient stress response. Another cause can be that I completely neglected the contact angle dependency in the viscous dissipation. However, figure 5.12 shows that the contact angle  $\theta$  is nearly constant during the spreading of 1% PAA but not at all for 3% PAA. I think that it may influence the speed of the line.

#### 5.1.4 Conclusions

The dynamics of the spreading is divided in several regimes. Here we look at the gravitational regime, where the driving force is the weight of the drop and the brake is viscosity. This regime lasts for a few milliseconds and ends abruptly. The physical cause of the transition to a slower

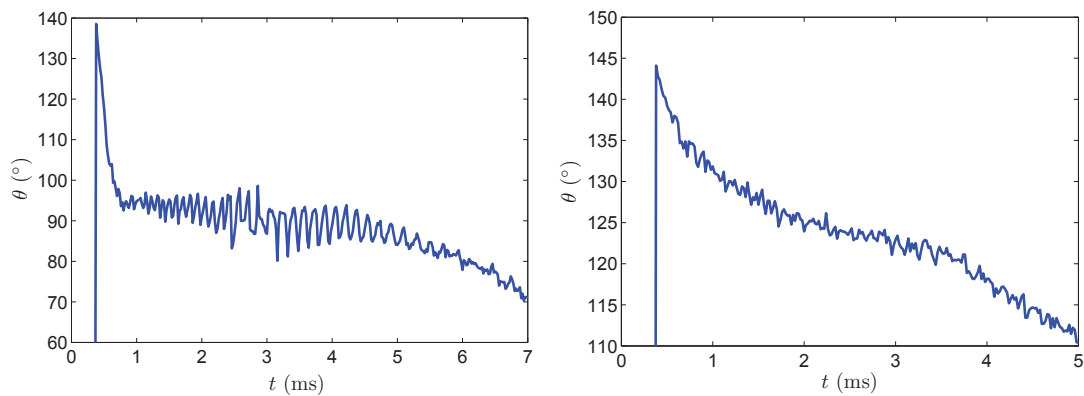


Figure 5.12 – Evolution of the contact angle in time for a 1% PAA solution (left) and for a 3% PAA solution (right). The end of the gravitational regime observed on the  $R(t)$  curves is respectively 6 ms and 4 ms. The oscillations on the graph are not physical, they are an artifact from the angle measurement method.

regime is not clear, but it might come from a geometrical constraint because we notice a simultaneous change in the evolution of the contact angle. Moreover the transition roughly corresponds to the moment where the drop shape becomes a spherical cap.

For viscoelastic fluids the spreading exponent is lower than 0.5, predicted for simple fluids, and it decreases when the polymer concentration increases. We propose a model based on the flow curve exponent  $n$ . Although this model does not take the fluid elasticity into account, and thus does not predict the evolution of the spreading exponent with polymer concentration, it already provides a good estimation. We plan to do the experiment with a shear-thickening fluid, for which  $n > 1$ .

Another project is to try rough surfaces and to see if roughness influences the spreading dynamics at short timescales. We can also spread water on normal clean glass, where there is contact angle hysteresis. The model does not predict any change with respect to smooth and completely wetting surfaces, but it is worth checking.

## 5.2 Experiments at long timescales

The experiments at short timescales provide information on the dissipation in the line with shear-thinning and yield-stress fluids. Another interesting point with yield-stress fluids spreading is raised at the end of the experiment: even when the substrate is perfectly wetting, yield-stress fluid drops stop spreading at a finite contact angle, while viscoelastic fluids without a yield stress spread completely. There is no reason for carbopol to have interfacial tensions with glass very different from PAA solutions, so Young's contact angle is expected to be the same for both fluids. This is not very surprising that here again, the yield stress prevents the system to reach its macroscopic equilibrium state.

The goal of this second experiment is to check how and when yield-stress fluid drops stop spreading, and to relate it to the yield stress value. The main questions were: do we find the exponent predicted for shear-thinning fluids (see section 1.3.1) also with yield-stress fluids? When does the transition to an arrested state occur? Does elasticity have an influence? Can we define a modified Young's law for yield-stress fluids? What is the influence of the surface roughness?

### 5.2.1 Setup and protocol

Long timescale spreading is very sensitive to any dust particle or imperfection on the wetting surface. Moreover evaporation has to be avoided. For these reasons a closed transparent box was built by Gilles Simon to allow me to perform the experiments in a clean environment, without having to work in a clean room. At the bottom of the box, a long ridge is regularly filled with water to maintain a wet atmosphere and hinder evaporation of the drops. A picture of the setup can be seen in figure 5.13. Before starting the experiments this box is completely cleaned with water and ethanol, and dried with compressed air, in a clean room. Then it is closed and never opened out of a clean environment.

The glass slides used as a substrate are cleaned as explained in section 5.1 and stored in a new petri dish. They are then placed horizontally in the box, on a homemade 3D-printed stage, under a laminar flow hood. The drop is deposited on the glass slide with a plastic pipette tip adjusted in a small hole in the box back wall. The end of the pipette tip is about 5 mm above the glass surface. The liquid is stored in a syringe linked to the pipette tip by 30 cm of Tygon tube. An inclined mirror is set under the glass slide to allow me to visualize the spreading drop from the bottom with a camera. The drop is illuminated from above with a LED panel which was half hidden by a piece of thick paper (this will be explained later). The setup is drawn schematically in figure 5.13.

The camera is a Phantom V5.1 used at 100 frames per second with a field of  $256 \times 256$  pixels. The objective is a tunable 28-300 mm aspherical Tamron used at its maximal focal length. The image scale is 21 pixels/mm.

For each experiment, the camera is started, then a drop is slowly pushed so that it hangs at the end of the pipette tip. The film is stopped 3 minutes after the moment where the drop detaches and touches the glass slide. A sample of resulting images is presented in figure 5.14. One can now see why the LED panel is half-hidden: the drop plays the role of a lens, so that the image of

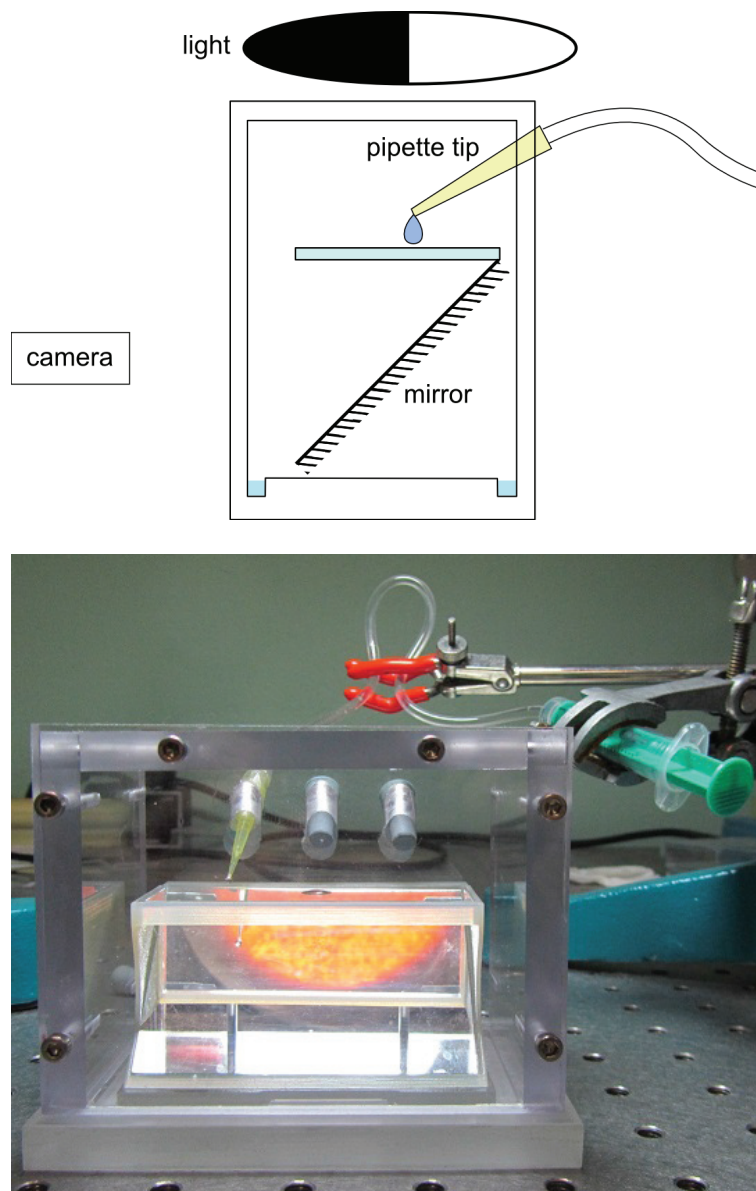


Figure 5.13 – Schematic drawing of the setup for spreading at long timescales, seen from the side, and a picture of the real setup, seen from the front.

the light is inverted only on the contact area. This way I get a good contrast on the whole drop outline, except where the pipette tip is visible. Otherwise the drop would appear white on a white background.

The films are processed with ImageJ and Matlab. The drop outline is detected with a home-made Matlab program. The output is a set of about 70 points that are fitted by a circle with the code *fitcircle* proposed by Richard Brown [106]. To minimize the error on the circle radius when the drop is not perfectly circular, the fit does not always take all the points into account. The distance from each outline point to the circle center (supposed to be the same as in the preceding image) is averaged. If one of these distances is less than the mean minus 10 pixels, the corresponding point is not taken into account for the fit, because at this point the line is probably trapped by a defect.

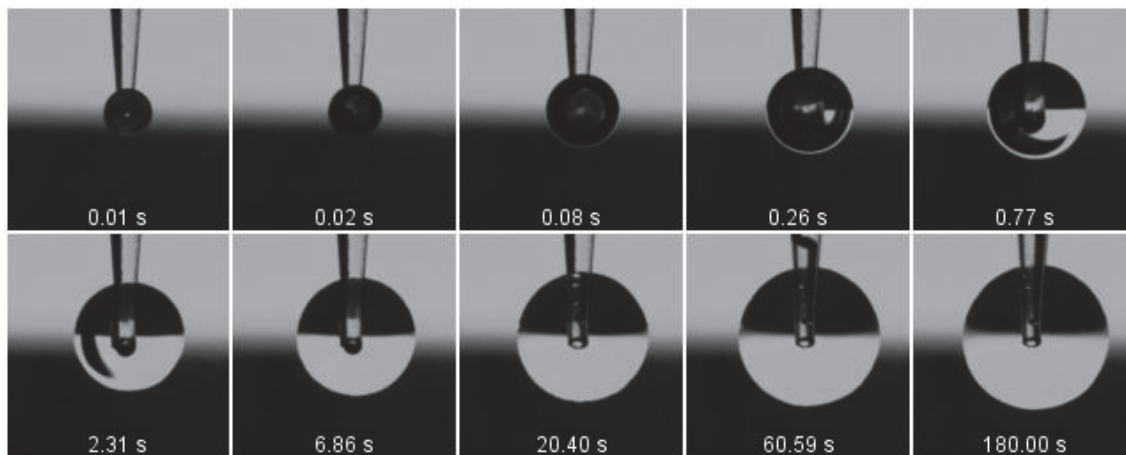


Figure 5.14 – Sample of snapshots from the film of the spreading of 0.5% MS carbopol. The yield stress is  $\sigma_y = 3.3 \text{ Pa}$ . The time interval is logarithmic. The size of each snapshot is 12 mm.

An example of a circular fit on one image from a film is shown in figure 5.15. Each film contains 18000 images at least. Finally the radius of the circular fit is plotted as a function of time.

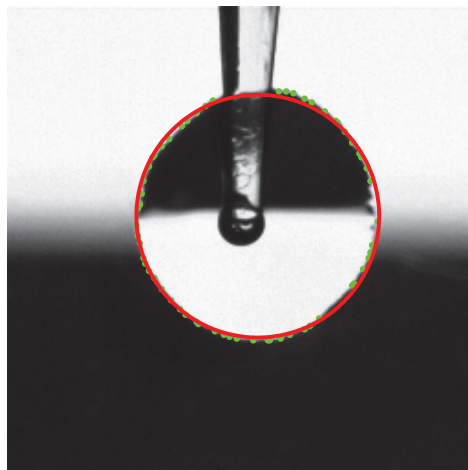


Figure 5.15 – Example of a typical image, with the detected outline (green dots) and the circular fit (red). During the analysis, 10 of these images are displayed to check the quality of the detection and of the fit.

## 5.2.2 Radius evolution in time

A first series of spreading experiments has been led with a 0.5% PAA solution. The goal was to compare the results with the spreading of 0.5% carbopol, which has the same chemical composition. The other purpose was to check if I recovered the spreading exponent calculated by Starov [10], solving Navier-Stokes equation under the assumptions of a small contact angle and a small Reynolds number. The main physical ingredients are a capillary driving balanced by viscous dis-

sipation. The exponent predicted by the theory, for a shear-thinning fluid of rheological exponent  $n$ , is

$$p = \frac{n}{3n + 7} \quad (5.13)$$

For 0.5% PAA,  $n = 0.8$ . I thus expect  $p = 0.085$  for the spreading exponent. However the curve of the contact radius evolution in time  $R(t)$  cannot be fitted with a power law of exponent 0.085 (figure 5.16, left). The contact radius increases slower than the power law. But if we look at the film, we see that the line is highly trapped by defects on the surface (figure 5.16, right). This trapping slows the progression of the line and the spreading.

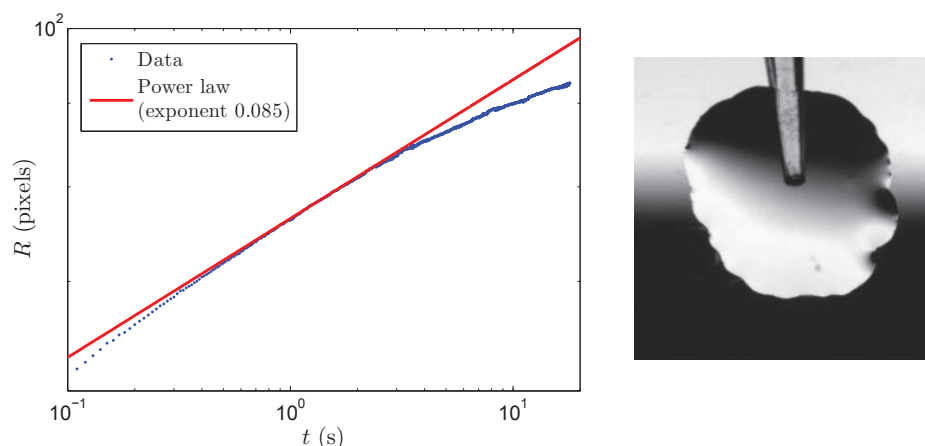


Figure 5.16 – Left:  $R(t)$  curve for the 0.5% PAA solution, with semilogarithmic axes. The blue dots are the data (averaged on 2 experiments) and the red line is the expected power law, with an exponent calculated from the rheological parameter  $n$ . Right: image from the film at  $t = 1$  min. The contact line is deformed by defects on the surface.

I have tried the same experiment with a 3% PAA solution ( $n = 0.74$ ). Surprisingly, although the glass plates are cleaned in exactly the same way as for the 0.5% PAA solution, the line does not look trapped any more (figure 5.17, right) and it is true for all 6 drops. The radius evolution seems to tend to the expected power law of exponent  $p = 0.080$  (figure 5.17, left).

Then experiments have been made with carbopols of different concentrations, types and stirrings. Because carbopol is known to slip on smooth surfaces, two solid surfaces have been tested. Most of the surfaces are smooth clean and hydrophilic glass slides (microscope slides). The second type of surface is clean and hydrophilic rough glass. The glass is roughened by sandblasting. The roughness has been measured with an optical profilometer (figure 5.18). On the picture we observe ‘holes’ in the surface corresponding to the impacts of the sand particles. Both the width and the depth of these holes are about  $20 \mu\text{m}$ .

Figure 5.19 shows 9  $R(t)$  curves, obtained from the analysis of 9 films with a same 1% carbopol. For each carbopol, between 6 and 9 experiments are analyzed, and an averaged  $R(t)$  is computed. Figure 5.20 shows this averaged  $R(t)$  for all the carbopols available. Several observations can be made from the  $R(t)$  curves, especially plotted with a logarithmic scale for time  $t$ .

First, compared to the spreading of PAA solutions, carbopol stops spreading after a time

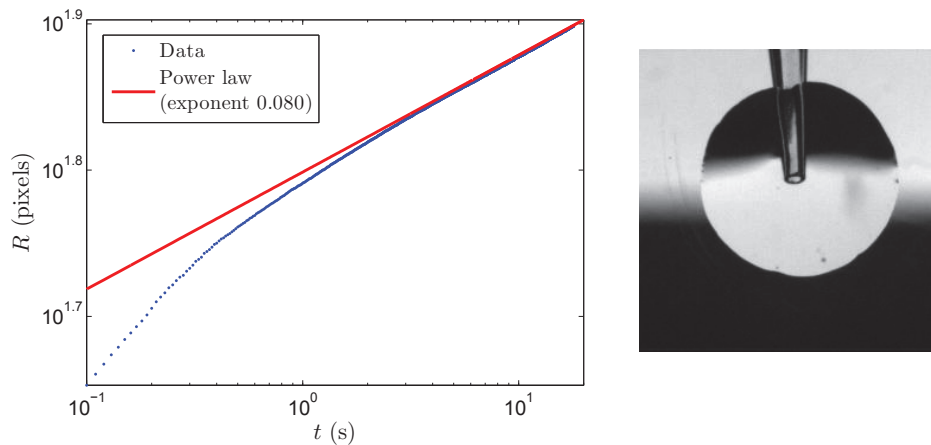


Figure 5.17 – Left:  $R(t)$  curve for the 3% PAA solution, with semilogarithmic axes. The blue dots are the data (averaged on 6 experiments) and the red line is the expected power law, with an exponent calculated from the rheological parameter  $n$ . Right: image from the film at  $t = 1$  min. The drop outline is circular this time.

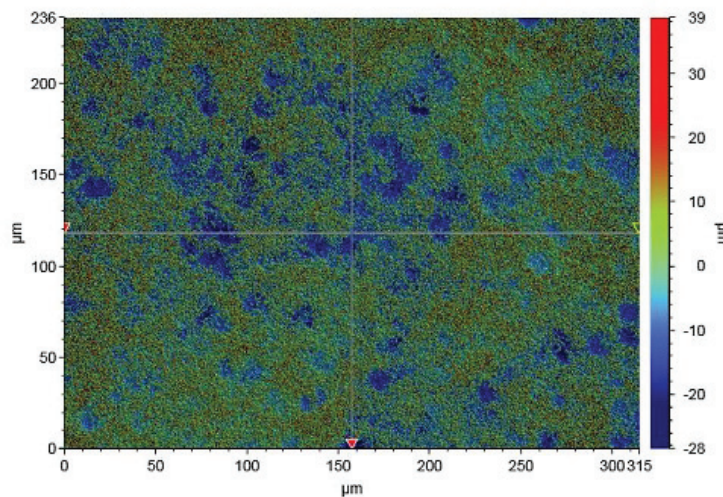


Figure 5.18 – Map of the surface of a sandblasted glass plate, measured with an optical profilometer.

comprised between 1 and 100 s, depending on the carbopol. Actually only the U10 carbopol stops as soon as 1 s. For ETD carbopols, spreading clearly slows down after a few tenths of seconds and seems to stop progressively. Longer experiments, with a better control of evaporation, could be performed to see the stop more clearly.

Secondly, the maximal radius is greater for lower yield stress. As the initial radius is not very well controlled, it is not relevant to interpret the precise evolution of the final radius with  $\sigma_y$ , but the overall tendency is clear. Another point that needs to be improved is controlling the volume of the drops. For the moment the volume is only controlled by the size of the tip. The same model of tip is used all the time, except for very concentrated carbopol. The volume of each drop is of the order of  $10 \mu\text{L}$  but it varies a little. Of course this must have an influence on the radius dispersion.

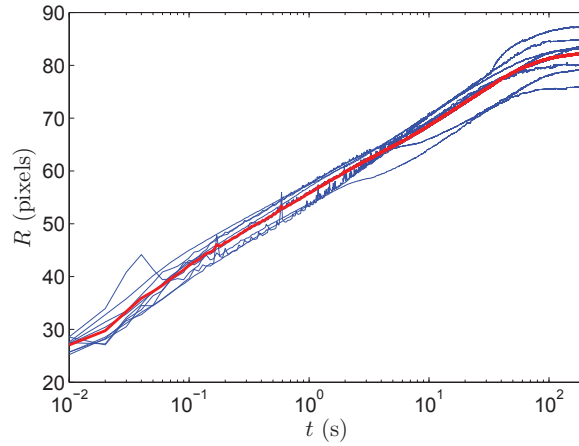


Figure 5.19 – Set of 9  $R(t)$  curves for the same carbopol (0.5% MS,  $\sigma_y = 3.3$  Pa), in blue. The red thick line is the average.

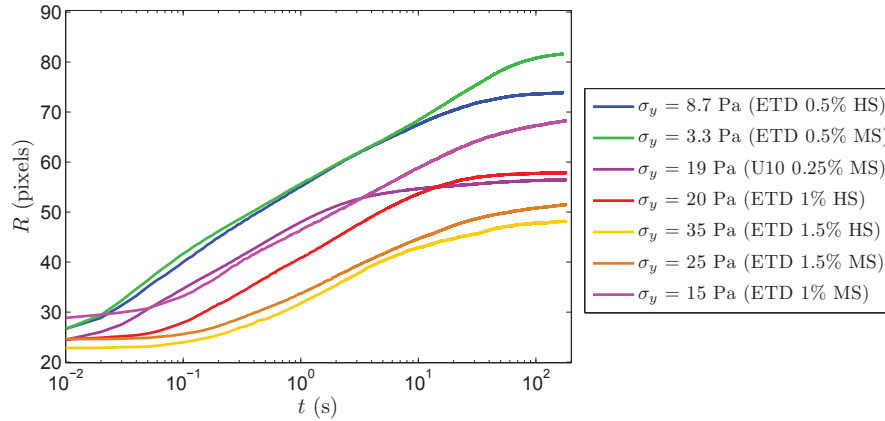


Figure 5.20 – Averaged  $R(t)$  curves for all the carbopols available. The carbopol nature and the yield stress are given in the legend.

Finally, a same carbopol in the same conditions spreads less on rough glass than on smooth glass (figure 5.22). It is especially visible for U10 carbopol because this carbopol slips much more than ETD carbopol on smooth glass. Figure 5.22 shows comparisons of the radius evolution, normalized by the initial radius, on smooth and rough glass, for two different carbopols of different types but similar yield stresses. The spreading plots are presented with the corresponding flow curves showing the amplitude of wall slip (actually the apparent stress) as a function of shear rate. Clearly, more slip induces a larger gap between  $R(t)$  on rough surfaces and  $R(t)$  on smooth surfaces:

$$\frac{\sigma_{\text{slip}}}{\sigma_y} \searrow \Rightarrow \frac{R_f(\text{smooth})}{R_f(\text{rough})} \nearrow \quad (5.14)$$

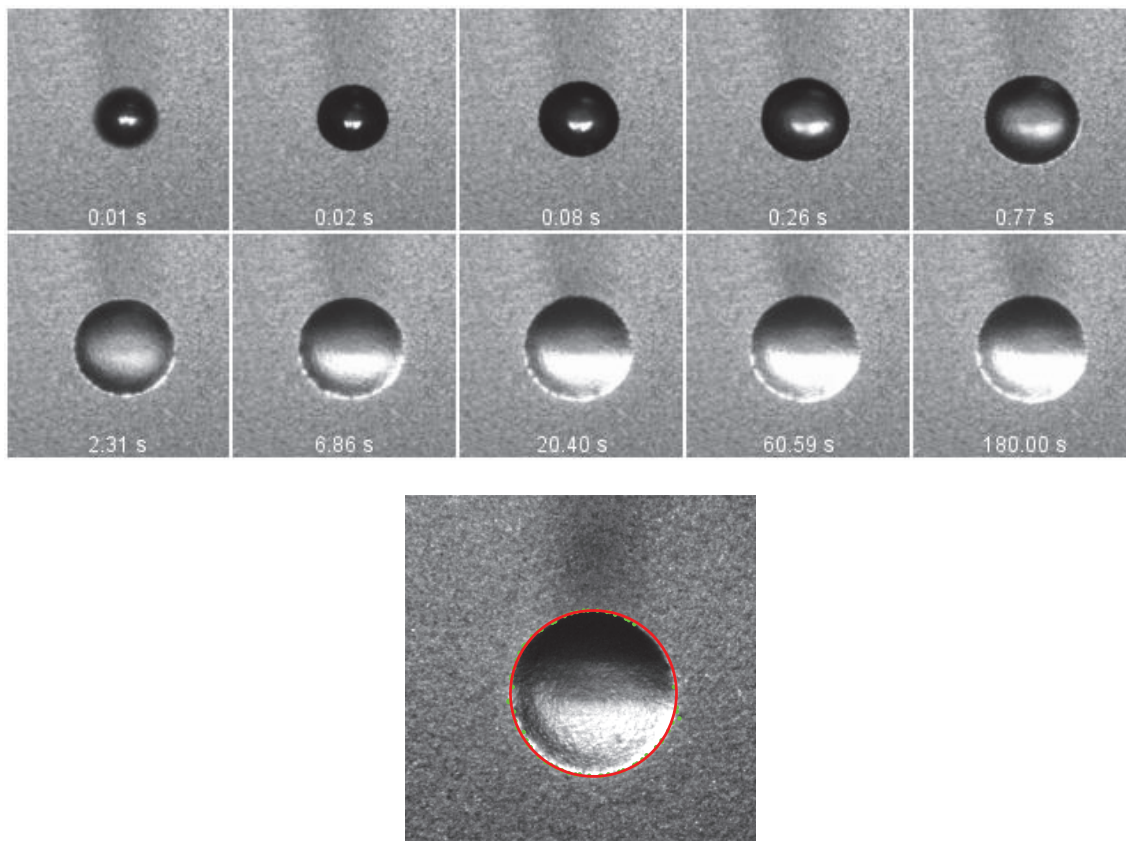


Figure 5.21 – Top: sample of snapshots from the film of the spreading of 0.5% MS carbopol on rough glass. The yield stress is  $\sigma_y = 3.3 \text{ Pa}$ . The time interval is logarithmic. The size of each snapshot is 12 mm. Bottom: illustration of the outline detection with rough glass. The presence of a white external ring interferes a little with the detection algorithm, causing extra noise in  $R(t)$ .

### 5.2.3 Final contact angle

From the previous section, we see that carbopol spreads less when the yield stress is higher and also less on a rough surface than on a smooth surface. If the drops had the shape of a spherical cap, this would suggest that the final contact angle increases with the yield stress and is larger on rough surfaces than on smooth surfaces. But at the beginning I had no information, either on the shape of the drops or on the contact angle. Therefore, I also started to take pictures of the drops final state from the side.

#### Setup

The camera is an IDS (UI-3580CP) with a resolution of 5 megapixels, equipped with a 50 mm Tamron objective. The contrast is optimized placing a white paper screen above the drop and a black background. An example of picture is shown in figure 5.23.

The profile and the contact angles of each drop are analyzed with the ImageJ plugin *Drop-Snake* [107]. To make this easier and more precise, a dozen of points are defined by hand on

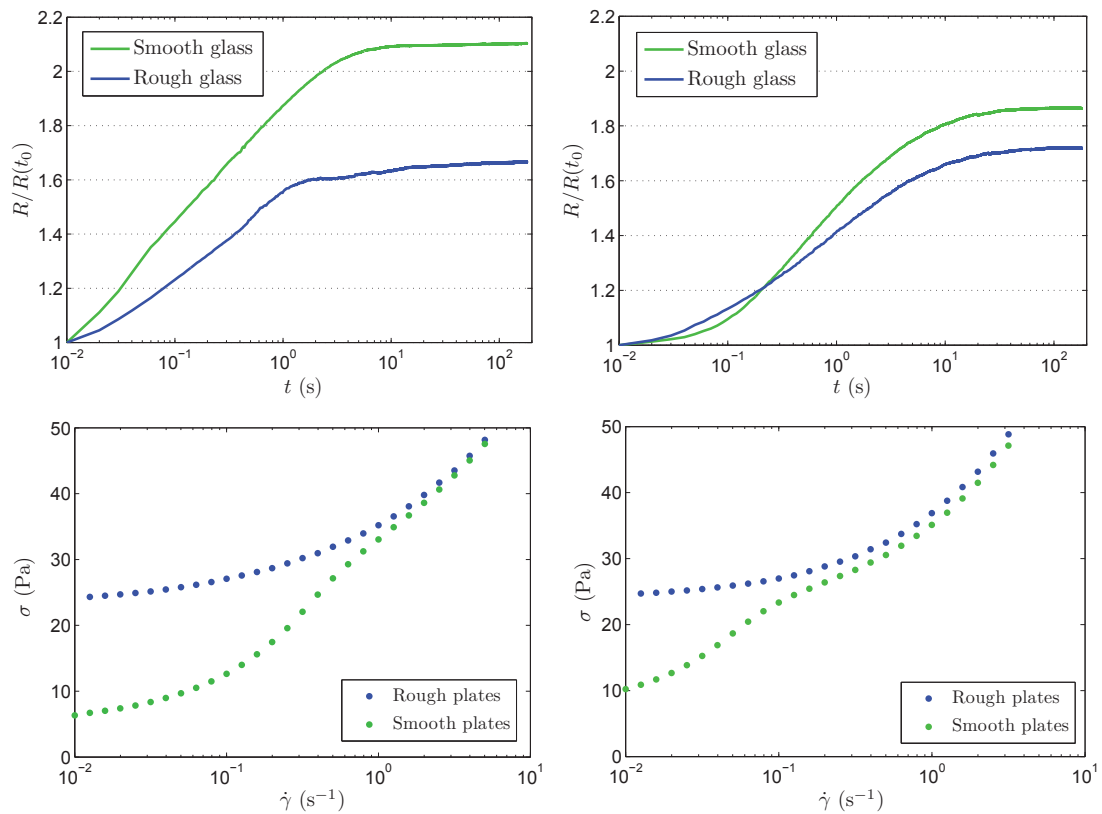


Figure 5.22 – Top: rescaled spreading radius of 0.25% U10 carbopol (left side) and of 1% ETD HS carbopol (right side), on smooth and rough glass. Bottom: respective flow curves measured with the rheometer, with smooth and rough plates. On smooth plates, we observe a kink between  $0.1 \text{ s}^{-1}$  and  $1 \text{ s}^{-1}$  and a strong decrease of the stress due to wall slip.

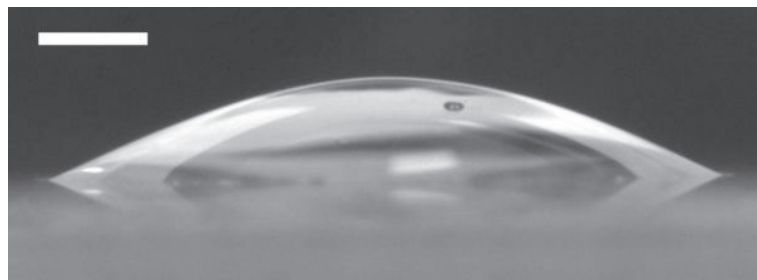


Figure 5.23 – Image of a final sessile drops of 0.5% ETD HS carbopol ( $\sigma_y = 8.7 \text{ Pa}$ ), on smooth glass. The scale bar represents 1 mm.

the image gradient intensity map (ImageJ function *Find Edges*). This is illustrated in figure 5.24. The resulting uncertainty on the angle estimation is about  $\pm 2^\circ$ , but the dispersion of the values measured for a same gel and a same surface is rather of the order of  $\pm 5^\circ$ , probably because of physical causes such as heterogeneities of the gel or of the surface.

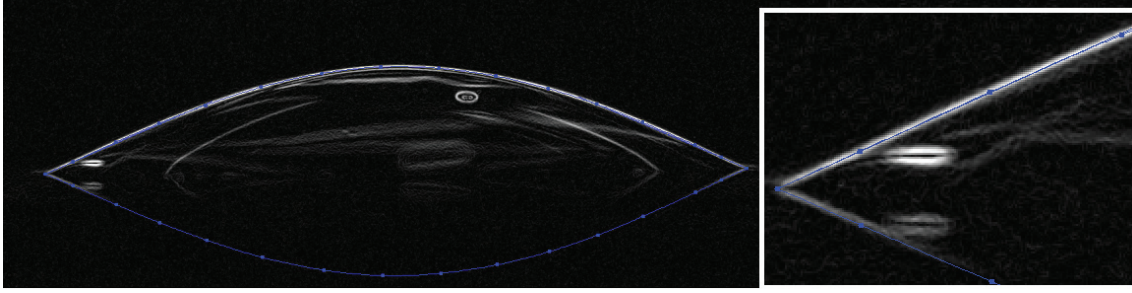


Figure 5.24 – Gradient intensity map (computed with ImageJ) of the image of a drop in its final state. The liquid is 0.5% HS carbopol. The blue points and line are the profile drawn with the plugin DropSnake. On the right, zoom on the contact zone.

### Influence of the yield stress

Figure 5.25, left, shows the evolution of the final contact angle  $\theta_f$  with the yield stress of the gel, on clean and hydrophilic smooth glass. We see that the angle increases with the yield stress. This suggests that spreading is arrested before reaching Young-Dupré equilibrium angle, because of the yield stress.

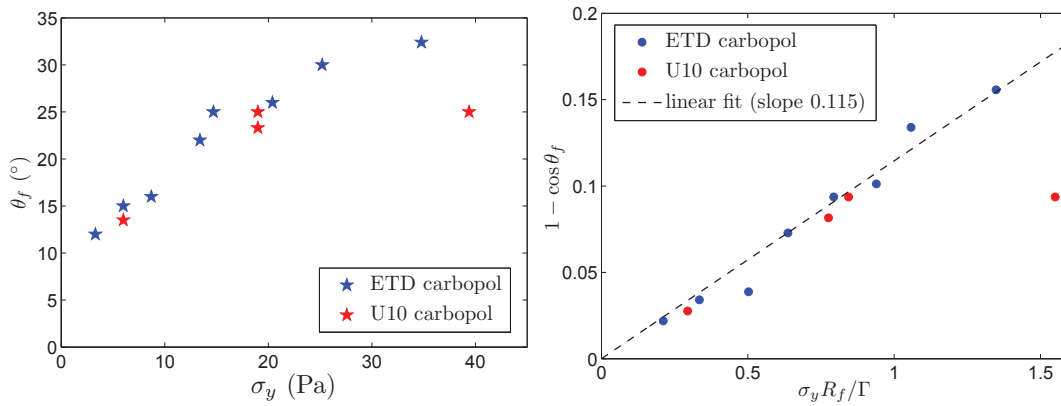


Figure 5.25 – Left: average final contact angle  $\theta_f$  plotted as a function of the yield stress  $\sigma_y$ . Each point is an average on 6 to 9 pictures. The dispersion of the angle measurements is about  $\pm 5^\circ$ . The blue and red points respectively stand for ETD carbopol and U10 carbopol. The surface is smooth glass. Right: to check relation 5.15, plot of  $1 - \cos \theta_f$  versus  $\sigma_y R_f / \Gamma$ .

A force balance on a portion of line provides a relation between  $\theta_f$  and  $\sigma_y$ . The driving force is of capillary origin. It is the difference between  $\Gamma_{SV} - \Gamma_{SL}$ , which is also  $\Gamma \cos \theta_0$  at equilibrium (see chapter 1), and  $\Gamma \cos \theta_f$ . The resisting force arises from the stress at the wall. This stress must be multiplied by a length to get a force per unit length. The most natural length is  $R_f$ , the final contact radius. Finally:

$$1 - \cos \theta_f = \beta \frac{\sigma_y R_f}{\Gamma} \quad (5.15)$$

where  $\beta$  is a prefactor of order 1. A rigorous derivation of the resisting force can be found in annex D.

This prediction fits well with the experimental results (see figure 5.25, right). However, one point obtained with U10 carbopol of high yield stress ( $\sigma_y = 39.5$  Pa) does not align with the other points. The final contact angle is clearly smaller than expected from the value of the yield stress. Here again, this is interpreted as an effect of wall slip. Indeed U10 carbopol slips more than ETD carbopol on smooth glass.

### Influence of wall slip

We thus made measurements on rough glass. For 7 different carbopols, varying the type, the concentration and the stirring, we measured the final contact angle on smooth and rough glass. The rough glass is sandblasted glass with a roughness of  $20\ \mu\text{m}$ . Figure 5.26 shows the average contact angle (on 3 to 6 drops) as a function of the yield stress, for the two types of surface. We see that, except for one carbopol, the contact angle is always greater on rough glass.

This cannot be due to a Wenzel effect. Indeed Wenzel's law [108] predicts that for a partially wetting fluid, the equilibrium contact angle is smaller on a rough surface, because the real solid-liquid interface is larger than the apparent contact area.

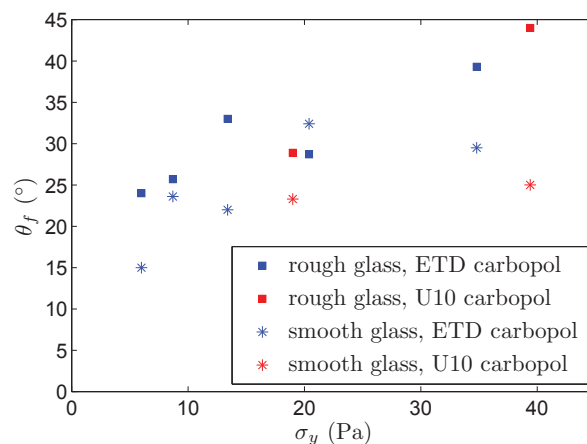


Figure 5.26 – Average final contact angle as a function of yield stress, on smooth and rough glass. The uncertainty is of the order of the angle dispersion, that is to say about  $\pm 5^\circ$ . We see that, except for one case (probably due to the large uncertainty),  $\theta_f$  is always greater on rough glass.

This result is consistent with the flow curves of figure 5.22, because in case of wall slip, the stress at vanishing velocity is smaller than the yield stress of the fluid. Following the relation 5.15, this explains why  $\theta_f$  and  $1 - \cos \theta_f$  are smaller on smooth surfaces than on rough surfaces. It is also consistent with what was observed in capillary rises [11]. Géraud *et al.* observed that the height reached by the yield-stress fluid in narrow channels was significantly larger when the channel walls were smooth than when they were rough. This observation had already been explained by a wall slip effect.

The influence of the surface roughness is clearly highlighted. Nevertheless the measurements are dispersed and it would be profitable to produce more data to be able to correlate experimentally the angle decrease on smooth glass with the wall slip stress.

### 5.2.4 Conclusions

This part is not complete, but it already shows interesting facts on the influence of the yield stress and of the surface roughness on the spreading of yield-stress fluids.

The most obvious conclusion is that a yield stress prevents the liquid to spread completely even on a totally wetting surface. We want to test the inverse experiment, sucking liquid from a big drop of yield-stress fluid, to measure an effective receding angle. This experiment should be made on a partially wetting substrate, and ideally with a very low contact angle hysteresis, to be able to see a difference between the receding angle and the equilibrium angle. For this, we could use glass treated with the process proposed by Krumpfer and McCarthy [100], or maybe smooth plastic such as Plexiglas. We can test these surfaces with PAA solutions, that have the same chemical composition as carbopol, but no yield stress.

A second conclusion is that the final state of a sessile yield-stress fluid drop depends a lot on the surface roughness because of wall slip. This conclusion is the same as in capillary rises [11], where a similar effect was observed, in a different geometry. We would like to make more experiments to have a more quantitative result. In particular, it is necessary to vary the drop volume to check the effect of the final radius  $R_f$  on the final contact angle. We also want to control the drop shape. Indeed, the carbopol drops seemed not to be axisymmetric. They had rather an oblate or even rounded triangular profile (seen from below). This was often a source of error on the contact radius (figure 5.27). A more systematic way to form drops would allow us to compare quantitatively the final contact radii from an experiment to another.

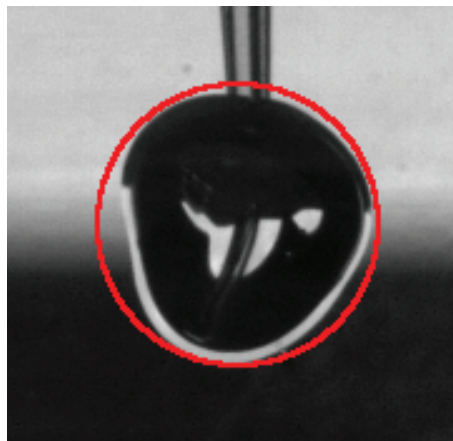


Figure 5.27 – Snapshot of a spreading drop of yield stress  $\sigma_y = 35$  Pa, seen from below. To emphasize the fact that the drop is not circular, a red circle has been superimposed on the picture.

# General conclusion

## Conclusions

The main goal of my thesis was to determine experimentally the influence of the specific rheology of yield-stress fluids on behaviors involving wetting. This specific rheology includes the existence of a yield stress, a solid-like elastic regime at low deformation, and a memory of the flow history through the internal stress. The large wall slip on smooth surfaces is also characteristic of yield-stress fluids and could be added to these features.

Therefore, during these three years, I have done several classical wetting experiments, but with yield-stress fluids.

The first experiment was quasi-static and highlighted the need to take into account the yield stress when doing surface tension measurements, even when capillary effects should predominate. It consisted in a measurement of the adhesion force of capillary bridges and the comparison with a purely capillary adhesion.

I have improved the tensiometer setup, to adapt it to the measurement of the surface tension of simple and complex fluid. For yield-stress fluids, it appears that this setup gives access to two different apparent surface tensions. The difficulty was to interpret these values and extract the physical surface tension of the gel. We could first explain why the values found in the literature do not always agree. Then we managed, in collaboration with Marie Le Merrer and H  l  ne Delano  -Ayari, to find a model that rationalized the experimental results, based on the computation of an elastoplastic force which must be added to the capillary force. An interesting point is that the sign of the elastoplastic force depends on the direction in which the bridge was deformed before the measurement. From this model, we explored the influence of the deformation history in the fluid and of the elasticity on the elastoplastic force. Finally we concluded that the actual surface tension of the gel was the mean of the two apparent surface tensions, under a few conditions. Among these conditions, the elastic modulus of the fluid must be several times greater than the yield stress. In other words, the critical yielding deformation must be much smaller than the total deformation undergone by the bridge.

In a second part, we have investigated the spreading dynamics of viscoelastic fluids, with or without a yield stress, as well as the influence of the yield stress on the final state. We have designed two different setups, each appropriate for a different time scale. Again, the experimental results have been explained by scaling laws. Several observations are interesting: first, the spreading dynamics at short timescales (during a few milliseconds) obeys to a power law, as predicted by

the theory, although both the driving forces and the dissipation sources are different. Indeed, the usual model takes into account a purely capillary driving power and an inertial resistance. Here we show that the movement of the center of mass, due to gravity, is balanced by viscous dissipation, and also in all likelihood by elasticity. The radius evolution that results is also a power law, but for complex fluids (shear-thinning) the exponent is lower than  $p = 0.5$  predicted by the capillary-inertia model. Secondly, the long-timescale evolution is rather dominated by the presence of a yield stress and by wall slip. The final contact angle increases with the yield stress value. But when the solid substrate is smooth, the contact angle is smaller than on a rough surface. This is interpreted as a wall slip effect.

These two parts are complementary in the sense that the capillary bridge experiments explored the elastoplastic character of the yield-stress fluid, while the spreading experiments focused on the viscoplastic side.

Aside from these two main experiments, I have also participated in a study on carbopol microstructure, using confocal microscopy, and performed rheometry measurements on carbopol samples. This was the opportunity to go into rheology issues more in depth, especially concerning the slow relaxation of carbopol under stress.

In a personal perspective, this work has been a rich experience that allowed me to develop many experimental skills and to deepen my understanding of complex fluids. But more globally, it is a contribution to the soft matter world, in the sense that it clarifies some important points on the issue of out-of-equilibrium wetting.

Two important ideas come out of the capillary bridge experiment. On the one hand, if capillary forces are measured, the non-relaxed stress creates supplementary elastoplastic forces that must be counted for the analysis. On the second hand, the shape of the surface of a yield-stress fluid system does not reflect an isotropic pressure (via Laplace's law), but rather an anisotropic total stress. The difficulty comes from the fact that generally, both the amplitude and the direction of the stress are unknown.

The spreading experiment inspires a tempting analogy. The finite stress at the wall prevents the liquid from spreading to the (Young) equilibrium state. This suggests an effective contact angle hysteresis, but involving a stress on all the contact area instead of a force on the line only. The line depinning was shown to be different from the yielding transition, in terms of universal exponents [70], but experimentally there seems to be a fruitful similarity.

To summarize the most prominent conclusion of the present thesis, yield-stress fluids are special because they are not just complex viscous fluids. Their behavior is in a large part governed by friction, and as a consequence, they are intrinsically out-of-equilibrium, or more rigorously, stuck out of the global energy minimum state. Therefore, the capillarity laws can be adapted to these fluids in some cases where the flow history is controlled and the stress field is known, but no general prediction can be made on the final state otherwise.

## Perspectives

This work also opened the way to new questions and future experiments.

The tensiometer experiments raised the issue of the effect of contact angle hysteresis and contact line pinning on the adhesion of capillary bridges, even with simple fluids. This is a troubling question, because the force balance (see chapter 4) does not need that the contact angle is the Young angle. The beginning of an answer hides perhaps in the slopes of the curvature  $C(z)$ , as mentioned in section 4.7, but this needs more work. Some experiments on this subject are presented in annex B.

Concerning the spreading experiments, we now want to explore the effect of the surface imperfections (roughness, chemical heterogeneities) on the spreading dynamics. We would like to exploit the analogy between contact angle hysteresis and yield stress to understand better both phenomena. Spreading experiments and contact angle hysteresis measurements are scheduled, on different surfaces: totally or partially wetting, with or without hysteresis, smooth or rough. We hope to see a signature of a similar non-viscous (ie. frictional) dissipation both with yield-stress fluids on rough surfaces and with simple (or viscoelastic) fluids on surfaces with hysteresis.

Finally, the carbopol stress relaxation process will be investigated more in depth, combining rheology measurements and microstructure images.



# **Annexes**

## A Rheological parameters of the carbopols used in the experiments

### Structure images

Type	Concentr.	Stirring	$\sigma_y$ (Pa)	$K$ (Pa.s <sup><i>n</i></sup> )	<i>n</i>	$G$ (Pa)	Used in ...
ETD	1%	MS	9.5	3.85	0.60	36	Fig. 3.8
ETD	0.75%	MS	6.1	3.43	0.58	28	Table 3.1
ETD	0.5%	MS	3.7	2.86	0.56	21	
ETD	0.25%	MS	0.8	1.36	0.57	7	
ETD	0.5%	HS	?	?	?	?	Fig. 3.11
U10	0.25%	MS	17.7	13.8	0.40	155	Fig. 3.8
ETD	1%	MS	19	5.18	0.59	48	
ETD	1.25%	MS	14.5	4.73	0.58	42	Table 3.1
ETD	1%	MS	10.7	4.78	0.56	38	Figs. 3.10 and 3.13
							Table 3.1
ETD	0.5%	MS	3.5	3.24	0.53	18	Table 3.1
ETD	0.25%	MS	1.0	1.87	0.53	7.5	Table 3.1

### Capillary bridges

Type	Concentr.	Stirring	$\sigma_y$ (Pa)	$K$ (Pa.s <sup><i>n</i></sup> )	<i>n</i>	$G$ (Pa)	Used in ...
ETD	0.25%	MS	0.3	0.76	0.60	1,5	Fig. 4.23
ETD	0.25%	MS	0.3	0.85	0.60	1,6	
ETD	0.25%	MS	0.6	1.39	0.54	4,5	
ETD	0.5%	MS	1.8	1.47	0.60	5	
ETD	0.5%	MS	1.9	1.66	0.59	7	
ETD	0.75%	MS	3.2	1.73	0.63	8	
ETD	0.75%	MS	5.1	3.57	0.56	20	
ETD	1%	MS	6.9	2.99	0.60	20	Fig. 4.13
ETD	0.75%	MS	7.0	3.55	0.58	23	
ETD	1%	MS	19.0	5.20	0.59	47	Figs. 4.11 and 4.25
ETD	1.75%	MS	22.1	6.09	0.59	55	
ETD	1,5%	MS	23.3	5.80	0.59	54	
ETD	2%	MS	27.6	8.73	0.56	71	
ETD	2%	MS	38.3	11.90	0.54	100	Fig. 4.20
U10	0.25%	MS	17.7	13.82	0.40	155	
ETD	0.25%	MS (30 min)	2.0	2.89	0.48	15	
ETD	0.25%	HS	4.6	5.42	0.46	28	Fig. 4.11
ETD	0.3%	HS	7.8	8.02	0.45	45	Fig. 4.13
ETD	0.75%	HS	15.6	12.68	0.49	80	Fig. 4.22

All these carbopols have been used for figures 4.12, 4.19 and 4.20.

**Spreading**

Type	Concentr.	Stirring	$\sigma_y$ (Pa)	$K$ (Pa.s <sup><i>n</i></sup> )	<i>n</i>	$G$ (Pa)	Used in ...
ETD	0.5%	MS	3.3	3.20	0.54	18	Figs. 5.11, 5.14, 5.19, 5.20, 5.25, 5.26 and 5.21
ETD	0.5%	HS	8.7	7.80	0.49	45	Figs. 5.20, 5.23, 5.24 and 5.26
ETD	1%	MS	14.7	5.22	0.57	50	Fig. 5.20
ETD	1%	HS	20.4	13.45	0.51	100	Figs. 5.20, 5.22 and 5.26
ETD	1.5%	MS	25.2	6.55	0.58	70	Fig. 5.20
ETD	1.5%	HS	34.8	15.75	0.54	130	Figs. 5.20, 5.26 and 5.27
ETD	0.5%	MS	6.0	4.06	0.51	35	Fig. 5.26
ETD	0.5%	HS	13.4	10.14	0.48	70	Fig. 5.26
U10	0.25%	MS	19.0	15.07	0.39	190	Figs. 5.20, 5.22 and 5.26
U10	0.5%	MS	39.4	16.31	0.40	250	Fig. 5.26
U10	0.5%	HS	51.9	17.58	0.41	335	

All these carbopols, except the last one, have been used for figure 5.25.

## B Effect of contact angle hysteresis on the adhesion of a capillary bridge

The experiments using the bridge tensiometer performed with simple fluids like water have shown an influence of the surface cleanliness and of contact angle hysteresis (CAH) on the force- $L$  plots (see chapter 4). To study this issue in more details, I proposed and supervised an internship on that issue during summer 2015. The experiments presented below have been performed by Quentin Legrand, a L3 student.

### B.1 Experiments

The experiments have been done on the capillary bridge tensiometer introduced in chapter 4. The measurement protocol and the analysis are the same. Therefore I invite the reader to refer to this chapter for details.

I only recall that we measure the force  $F$  exerted by the capillary bridge on two parallel glass plates. The force is saved for different aspect ratios of the bridge, either after axial stretching or compression. The force values are then plotted versus  $L$ , a geometrical parameter defined as:

$$L = 2\pi R_N - \pi R_N^2 C_N \quad (6.1)$$

where  $R_N$  is the neck radius and  $C_N$  the mean curvature of the surface, also at the neck.

If the surface tension  $\Gamma$  is the only ingredient at play, we expect a proportional relation between  $L$  and  $F$ , the slope being  $\Gamma$ . For experiments performed with silicone oil, no CAH was visible and the proportionality between  $L$  and  $F$  was observed. In the case of water, it was more delicate to have no CAH. Nonetheless, a few experiments exhibited a small CAH (less than  $10^\circ$ ) and for those, a good alignment of the points was obtained. For the other experiments, the CAH was strong, and we observed an hysteresis in the force- $L$  plots (figure 6.1). Indeed the points taken after stretching did not align with the points taken after compression and the stretching branch had a higher slope than the compression branch. This means that extra normal forces arise from CAH.

The goal of this internship was to find the origin of the misalignment of the stretching and compression branches, in other words the origin of the extra forces. In order to achieve this, we varied the surface hysteresis of the glass plates. Note that it is very difficult to control CAH, so our strategy was to use different glass surfaces and to measure the CAH a posteriori. More precisely, we used smooth hydrophilic glass to minimize hysteresis, an “old” glass slide exhibiting a large hysteresis (of unknown origin), and also glass slides covered with melt polystyrene microbeads. Indeed, we expected the microbeads to act as surface defects and to strongly pin the line.

For each experiment, the contact angles were measured at the top and at the bottom of the bridge, in addition to the usual quantities  $F$  and  $L$ . The difference of slopes between the stretched branch and the compressed branch is denoted  $\Delta\Gamma$ , by analogy with the theoretical result (linear dependence with a slope equal to the surface tension of the fluid  $\Gamma$ ). Quentin categorized the results in several groups, depending on the angle hysteresis intensity, ranging from  $10^\circ$  to  $40^\circ$ .

Unfortunately, because of many experimental problems, few experiments could be really exploited, and no clear correlation could be detected between the contact angles and  $\Delta\Gamma$ . Nevethe-

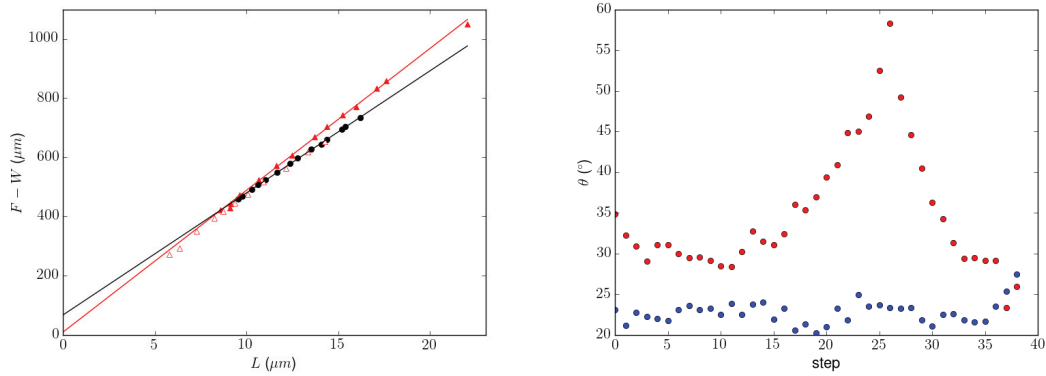


Figure 6.1 – Left: force- $L$  plot of pure water.  $\Delta\Gamma = 6.7 \text{ mN/m}$ . Right: contact angles on the top plate (red circles) and on the bottom plate (blue circles), for each step. The top plate has a strong CAH and the bottom plate has nearly no CAH.

less, most of the experiments exhibited a positive  $\Delta\Gamma$ , typically of the order of  $5 \text{ mN/m}$ , and a strongly asymmetric contact angle hysteresis, as shown in figure 6.1. For those experiments, the amplitude of  $\Delta\Gamma$  increases, in average, with the CAH amplitude. But a few experiments had fully aligned points in spite of a noticeable CAH (figure 6.2), which shows that other physical phenomena are certainly at play. Finally, some experiments had a negative  $\Delta\Gamma$  but a thorough examination of the pictures shows that the wetted surface was limited by the top glass plate edges, so the conditions of the experiment were not the same as those showing a positive  $\Delta\Gamma$ .

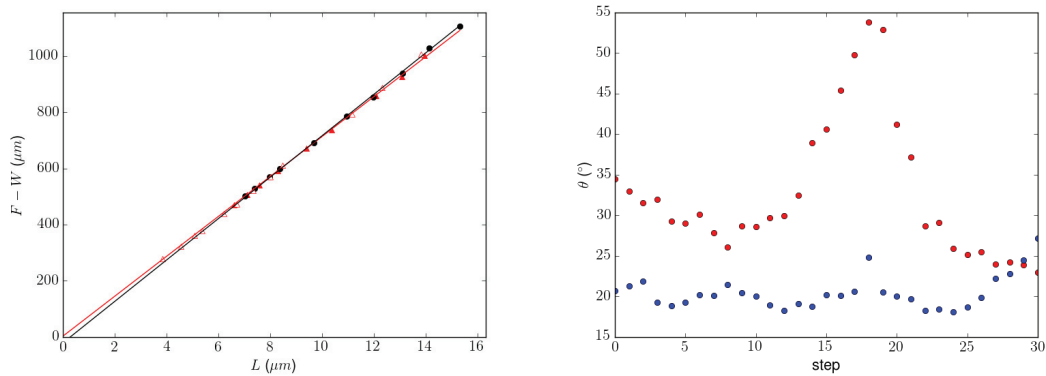


Figure 6.2 – Left: force- $L$  plot of pure water. Right: contact angles on the top plate (red circles) and on the bottom plate (blue circles), for each step. Here the points are aligned in spite of a strong CAH on the top plate.

### B.2 Friction-based model

The interesting result is the existence of a force perpendicular to the plates associated to a CAH. It is well known that CAH can be explained by the energetic dissipation due to the pinning-depinning of the moving contact line, as presented in chapter 2. This pinning-depinning process results in a macroscopic friction force, exerted by the surface defects on the contact line, tangential to the

surface and opposed to the motion. This has been modeled by Crassous and Charlaix [58] and has been evidenced experimentally by Moulinet [54] who measured a force hysteresis along the plate, associated to the dissipation of a moving contact line. On the other hand, normal forces at the contact line have been studied only at equilibrium [109]. We did not find in the literature any reference on a force perpendicular to the surface associated to the pinning of the line.

To describe our experimental results, we tried to develop simple models based on CAH. Here we suppose that the supplementary force is due to CAH and to the friction of the contact line on the solid surface.

The first attempt consisted in applying a correction to the force, assuming a normal force per unit length  $\Gamma \sin \theta$ . We estimated the equilibrium contact angle  $\theta_0$  by:

$$\cos \theta_0 = \frac{1}{2}(\cos \theta_a + \cos \theta_r) \quad (6.2)$$

with  $\theta_a$  and  $\theta_r$  the maximum and minimum contact angles observed during the experiment. Note that it is an approximation because we cannot be sure to have actually reached the advancing and receding angles. From the real angles  $\theta$  and the contact radii  $R_c$  at the top and the bottom of the bridge, we corrected the measured force with:

$$\Delta F_{\text{corr}} = 2\pi R_c \Gamma (\sin \theta - \sin \theta_0) \quad (6.3)$$

However this correction did not result in a better alignment of the two branches. Sometimes it reduced  $\Delta\Gamma$ , but sometimes it increased it, in particular in the case of figure 6.2, where the points were already aligned. Therefore the origin of the normal force must be more complex.

The second attempt consisted in associating an energy dissipation to the CAH, through a friction force hypothesis. I started with a numerical calculation of the bridge profile relying on an article by Fortes [95], who proposes a convenient parametrization to compute the bridge profile. I imposed boundary conditions mimicking a contact hysteresis, a fixed volume and height steps (increasing and decreasing series, like in the experiments). The model neglects gravity, so the numerical bridge has a vertical symmetry. First I mimick a stretching phase. The contact angle is set to its receding value (here  $30^\circ$ ) and the contact radius is free (phase 1 on figure 6.3). Then the deformation is reversed, the bridge is compressed. At the beginning of the compression, the line is pinned and the contact angle increases (phase 2). When the contact angle reaches its advancing value (here  $60^\circ$ ) it is kept constant and the contact radius is set free (phase 3) Finally, the bridge is stretched again and the line is pinned until the contact angle reaches its receding value (phase 4). The variation of the contact angle with respect to the bridge height  $d$  is summarized in figure 6.3, left.

I make the hypothesis that when the line moves tangentially to the surface, it undergoes a friction force equal to:

$$f = \Gamma(\cos \theta - \cos \theta_0) \quad (6.4)$$

Again, the equilibrium contact angle is defined by:

$$\cos \theta_0 = \frac{1}{2}(\cos \theta_a + \cos \theta_r) \quad (6.5)$$

Then if the bridge is stretched, the line recedes,  $R$  decreases and an energy (per unit length of the line)  $\delta w = -f\delta R > 0$  is dissipated. The same applies if the bridge is compressed. The supplementary normal force resulting from this dissipation is:

$$F_d = \frac{2\pi R\delta w}{\delta d} = -2\pi R\Gamma(\cos\theta - \cos\theta_0)\frac{\delta R}{\delta d} \quad (6.6)$$

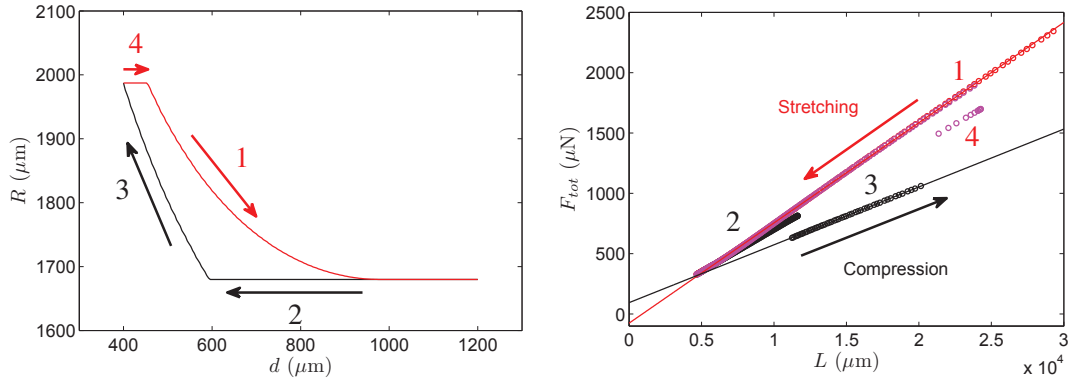


Figure 6.3 – Left: evolution of the contact radius with the bridge height  $d$ , with a  $30^\circ$  imposed CAH. Right: force- $L$  plot resulting from the friction model.

The force- $L$  plot resulting from this rough model is presented in figure 6.3, right. We recover two branches, the upper one for stretching and the lower one for compression. For phases 2 and 4, where the line is pinned and does not move, there is no dissipation and  $F_d = 0$ , which results in discontinuities in the force- $L$  plot. Of course it is not realistic, but the important result is that we find a normal force with a sign depending on the direction of the bridge deformation and an amplitude depending on the CAH strength.

### B.3 Perspectives

On the one hand, the experiments need to be repeated more. We have to use surfaces with a controlled CAH. In addition, to avoid the limitation of the wetted area because of the size of the top plate, we could use spherical-cap-shaped glass, for example a small lens, at the end of the cantilever, as in [110]. We have also tried to pin the line strongly in a circular micro-ridge, but for technical reasons the experiment did not succeed. It would be interesting to try again. For example, instead of etching a circle in a large glass plate, we could use a circular plate of the desired size, and pin the line on its edge.

Part of the improvements are the same as in chapter 4: in particular the temperature and humidity in the measurement chamber have to be controlled, to avoid the drift of the sensor and the drop evaporation.

On the other hand, the friction model has to be developed more in depth. A simulation software such as COMSOL Multiphysics might be used. However, such a simulation would still rely on a theoretical assumption such as triple line friction.

## C Surface Fluctuation Specular Reflection spectroscopy measurements

In June 2014, I had the opportunity to use an experimental setup designed by Laurence Talini at the ESPCI in Paris. The experiment is called Surface Fluctuation Specular Reflection (or SFSR) spectroscopy. It is described in details in reference [44].

### C.1 Setup and protocol

The basic principle is to measure the frequency spectrum of the thermal free surface fluctuations. A thin ( $\sim 1$  mm) layer of liquid is placed in a cell of diameter 5 cm. The probe is a laser beam focused on the liquid surface, and the beam deviation after reflection is monitored with a two-quadrant photodiode. Then the time fluctuations of the photodiode signal are analyzed. The resulting spectrum depends on the linear rheology of the fluid (ie. the viscoelastic moduli  $G'$  and  $G''$  as functions of the frequency) and on the material surface tension  $\Gamma$ . Therefore, if the linear rheology of the fluid is known from another experiment, for example rheometry, we can deduce the surface tension from the SFSR spectrum.

The goal was to compare the surface tension measurements obtained with the capillary bridge tensiometer with values from another method. The SFSR method was really interesting for us because the triple line (solid-liquid-air boundary) had no role and because it did not imply a force measurement. Thus the contact angle hysteresis and the residual internal stress were not supposed to interfere with the surface tension measurement.

In practice, the fluid is poured in the cell and weighted to be able to know the thickness of the sample. The fluctuation signal is recorded and the frequency spectrum is computed from 5 Hz to 50 000 Hz. The fluctuation spectrum is fitted with 20 parameters for  $G^*(\omega)$  and one parameter for  $\Gamma$ . For a better result, the  $\Gamma$  parameter is imposed at a plausible value and the  $G'(\omega)$  and  $G''(\omega)$  curves are compared with those from the rheometer.

### C.2 Results

It appears that  $G'$  at low frequency (down to a few Hz) is very sensitive to very small changes in  $\Gamma$ . For example, table 6.1 summarizes the values of  $G'$  and  $G''$  at 10 Hz corresponding to different values of the parameter  $\Gamma$ , for a 1% MS carbopol with  $G' = 50$  Pa at 10 Hz measured with a rheometer.

$\Gamma$ (mN/m)	$G'$ (Pa) at 10 Hz	$G''$ (Pa) at 10 Hz
45	120	20
47	90	20
49	57	19
50	40	18
51	25	18

Table 6.1 – Variation of  $G'$  and  $G''$  at 10 Hz when varying the fitting parameter  $\Gamma$ , for a SFSR spectrum of 1% MS carbopol.

For this 1% MS carbopol, we deduce a surface tension value between 49 mN/m and 50 mN/m. The results are summarized in table 6.2.

Concentration % wt	$\Gamma$ (mN/m)	From SFSR		From a rheometer	
		$G'$ (Pa)	$G''$ (Pa)	$G'$ (Pa)	$G''$ (Pa)
0.25%	56	8	8	9	7
0.5%	51	25	11	17	12
1%	49	57	19	50	21

Table 6.2 – Surface tensions measured by the SFSR technique, and the corresponding values of  $G'$  and  $G''$  at 10 Hz. The values of  $G'$  and  $G''$  at 10 Hz from a rheometer measurement are also given.

### C.3 Comments

With the capillary bridge tensiometer, we obtained surface tension values between 63 mN/m (for 0.25% carbopol) and 59 mN/m (for 0.75% carbopol). We see from table 6.2 that the values measured with the SFSR technique are sensibly lower.

We have no clear explanation for this difference, but we can propose a few hypothesis. First, the surface can have been polluted by dust or surfactants. We also measured the surface tension of water (distilled but stored in a plastic bottle) and obtained  $(67 \pm 1)$  mN/m, which is also a bit lower than the tabulated value for pure water. Secondly, the liquid thickness also played a role but it was not well controlled precisely for most of the experiments.

These experiments lasted for only two days, and I did not have enough time to master the setup enough to exploit its full potential. However it already provided interesting information, such as an order of magnitude of the surface tension and a decrease of the values for carbopols of increasing concentration.

## D Spreading dynamics calculations

In this annex, I give the details of the flow calculation in the liquid wedge near the triple line, when a yield-stress fluid drop is spreading on a wetting surface.

The surface is supposed to be completely wetting, which means that the equilibrium contact angle is zero. The fluid is described by the Herschel-Bulkley model :  $\sigma = \sigma_y + K\dot{\gamma}^n$ . The geometry used for the calculation is given in figure 6.4.

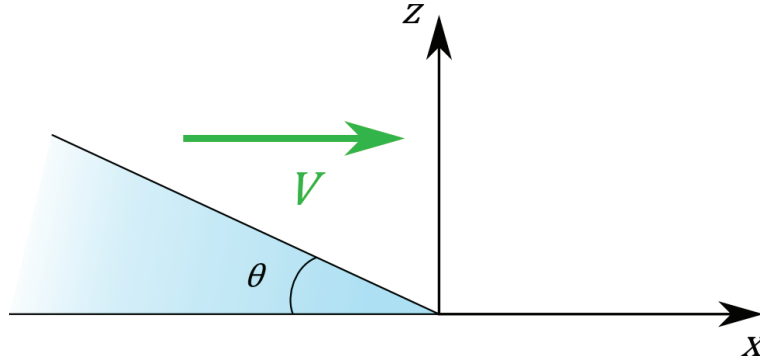


Figure 6.4 – Geometry used for the calculation.

**Driving power.** While advancing at a velocity  $V$ , the contact line makes an angle  $\theta$  with the surface, so the force per unit length is:

$$F = \Gamma(1 - \cos \theta) \quad (6.7)$$

Then, the driving power is:

$$P = FV = \Gamma(1 - \cos \theta)V \quad (6.8)$$

**Velocity profile in the wedge.** In the lubrication assumption, and because the stress is zero at the free surface, the shear stress depends mainly on the height  $z$ :

$$\sigma = A(\xi(x) - z) \quad (6.9)$$

where  $A$  is the pressure gradient created by the capillary forces, and  $\xi(x)$  is the liquid-air interface position. Note that  $A$  is unknown a priori. It will be determined at the end from a flow rate balance. For a yield-stress fluid it is appropriate to define a critical height  $z_y(x) = \xi - \sigma_y/A$ , which divides the fluid wedge in two parts:

- for  $z < z_y$ , the stress is above the yield stress and the fluid is sheared. The velocity gradient is given by:

$$A(\xi(x) - z) = \sigma_y + K \left( \frac{\partial v_x}{\partial z} \right)^n \quad (6.10)$$

The integration of this equation leads to:

$$v_x(z) = \left( \frac{A}{K} \right)^{\frac{1}{n}} \frac{n}{1+n} \left( z_y^{1+\frac{1}{n}} - (z_y - z)^{1+\frac{1}{n}} \right) \quad (6.11)$$

- for  $z > z_y$ , the stress is below the yield stress and the flow is a plug flow at the velocity:

$$v_x(z) = v_{\max} = \left(\frac{A}{K}\right)^{\frac{1}{n}} \frac{n}{1+n} z_y^{1+\frac{1}{n}} \quad (6.12)$$

Using equation 6.12, it is easier to rewrite to velocity profile for  $z < z_y$ :

$$v_x(z) = v_{\max} \left(1 - (1 - z/z_y)^{1+\frac{1}{n}}\right) \quad (6.13)$$

**Pressure gradient at the flow end.** To get  $A$ , the pressure gradient, we need to equilibrate the flow rates:

$$\int_0^\xi v_x(z) dz = V\xi \quad (6.14)$$

$$v_{\max} \left(\xi - \frac{n}{2n+1} z_y\right) = V\xi \quad (6.15)$$

In the general case,  $z_y$  and  $v_{\max}$  both depend on  $A$ , so the equation that must be solved to find  $A$  is complicated. However, when the flow is just stopping,  $\dot{\gamma} \rightarrow 0$  and  $\sigma \rightarrow \sigma_y$ . Then  $z_y \ll \xi$ . We can thus simplify:

$$V = v_{\max} = \left(\frac{A}{K}\right)^{\frac{1}{n}} \frac{n}{1+n} z_y^{1+\frac{1}{n}} \quad (6.16)$$

$$\left(\frac{A}{K}\right)^{\frac{1}{n}} = \frac{1+n}{n} \frac{V}{z_y^{1+\frac{1}{n}}} \quad (6.17)$$

**Dissipated power.** The dissipated power per unit volume is  $p = \sigma\dot{\gamma} \approx \sigma_y\dot{\gamma}$ , with:

$$\dot{\gamma} = \left(\frac{A}{K}\right)^{\frac{1}{n}} (z_y - z)^{\frac{1}{n}} \quad (6.18)$$

$$= \frac{1+n}{n} \frac{V}{z_y} \left(1 - \frac{z}{z_y}\right)^{\frac{1}{n}} \quad (6.19)$$

Then:

$$P = \int_{-\infty}^0 dx \int_0^{z_y} dz \sigma_y \frac{1+n}{n} \frac{V}{z_y} \left(1 - \frac{z}{z_y}\right)^{\frac{1}{n}} \quad (6.20)$$

$$= \int_{-\infty}^0 dx \sigma_y V \frac{1+n}{n} \frac{1}{1/n+1} \quad (6.21)$$

$$= \sigma_y V \int_{-\infty}^0 dx \quad (6.22)$$

Replacing the infinite boundary of the integral with a cutoff of the order of  $R$ , we finally get:

$$\beta R \sigma_y V = \Gamma(1 - \cos \theta) V \quad (6.23)$$

$$1 - \cos \theta = \beta \frac{\sigma_y R}{\Gamma} \quad (6.24)$$

where  $\beta \sim 1$ .



# Bibliography

- [1] J. Boujlel and P. Coussot. Measuring the surface tension of yield stress fluids. *Soft Matter*, 9(25):5898–5908, June 2013.
- [2] G. German and V. Bertola. The free-fall of viscoplastic drops. *J. Non-Newtonian Fluid Mech.*, 165(13-14):825–828, July 2010.
- [3] G. German and V. Bertola. The spreading behaviour of capillary driven yield-stress drops. *Colloids Surf., A*, 366(1-3):18–26, August 2010.
- [4] V. Bertola. Dynamic wetting of dilute polymer solutions: The case of impacting droplets. *Adv. Colloid Interface Sci.*, 193-194:1–11, June 2013.
- [5] L. Martinie, H. Buggisch, and N. Willenbacher. Apparent elongational yield stress of soft matter. *J. Rheol.*, 57(2):627–646, March 2013.
- [6] B. Géraud. *Mouillage et dynamique confinée de fluides complexes*. PhD thesis, Université Claude Bernard Lyon 1, Lyon, October 2013.
- [7] J. Piau. Carbopol gels: Elastoviscoplastic and slippery glasses made of individual swollen sponges. *J. Non-Newtonian Fluid Mech.*, 144(1):1–29, June 2007.
- [8] D. Lee, I. A. Gutowski, A. E. Bailey, L. Rubatat, J. R. de Bruyn, and B. J. Frisken. Investigating the microstructure of a yield-stress fluid by light scattering. *Phys. Rev. E*, 83(3), March 2011.
- [9] I. A. Gutowski, D. Lee, J. R. d. Bruyn, and B. J. Frisken. Scaling and mesostructure of Carbopol dispersions. *Rheol Acta*, 51(5):441–450, May 2012.
- [10] V. M. Starov, A. N. Tyatyushkin, M. G. Velarde, and S. A. Zhdanov. Spreading of non-Newtonian liquids over solid substrates. *J. Colloid Interface Sci.*, 257(2):284–290, January 2003. WOS:000180947700014.
- [11] B. Géraud, L. Jørgensen, L. Petit, H. Delanoë-Ayari, P. Jop, and C. Barentin. Capillary rise of yield-stress fluids. *Europhys. Lett.*, 107(5):58002, September 2014.
- [12] R. Y. Z. Hu, A. T. A. Wang, and J. P. Hartnett. Surface tension measurement of aqueous polymer solutions. *Exp. Therm. Fluid Sci.*, 4(6):723–729, November 1991.

- [13] S. Ishiguro and J. Hartnett. Surface tension of aqueous polymer solutions. *Int. Comm. Heat Math Transfer*, 19(2):285–295, March 1992.
- [14] R. M. Manglik, V. M. Wasekar, and J. Zhang. Dynamic and equilibrium surface tension of aqueous surfactant and polymeric solutions. *Exp. Therm. Fluid Sci.*, 25(1–2):55–64, 2001.
- [15] K. Niedzwiedz, H. Buggisch, and N. Willenbacher. Extensional rheology of concentrated emulsions as probed by capillary breakup elongational rheometry (CaBER). *Rheol. Acta*, 49(11-12):1103–1116, December 2010.
- [16] J. Boujlel. *Déplacement d'un objet à travers un fluide à seuil : couche limite, contrainte seuil et mouillage*. PhD thesis, Université Paris-Est, November 2012.
- [17] V. Bertola. Wicking with a yield stress fluid. *J. Phys.: Condens. Matter*, 21(3):035107, January 2009.
- [18] A. L. Yarin. Drop Impact Dynamics: Splashing, Spreading, Receding, Bouncing. . . . *Annu. Rev.*, 38(1):159–192, 2006.
- [19] J.-L. Grossiord and A. Ponton. *La mesure en rhéologie: des avancées récentes aux perspectives*. EDP Sciences, Les Ulis, January 2014.
- [20] T. Divoux, C. Barentin, and S. Manneville. From stress-induced fluidization processes to Herschel-Bulkley behaviour in simple yield stress fluids. *Soft Matter*, 7(18):8409, 2011.
- [21] B. Géraud, L. Bocquet, and C. Barentin. Confined flows of a polymer microgel. *Eur. Phys. J. E*, 36(3):1–13, March 2013.
- [22] C. Cottin-Bizonne, S. Jurine, J. Baudry, J. Crassous, F. Restagno, and É. Charlaix. Nanorheology: An investigation of the boundary condition at hydrophobic and hydrophilic interfaces. *Eur. Phys. J. E*, 9(1):47–53, September 2002.
- [23] A. Magnin and J. M. Piau. Shear rheometry of fluids with a yield stress. *Journal of Non-Newtonian Fluid Mechanics*, 23:91–106, January 1987.
- [24] S. P. Meeker, R. T. Bonnecaze, and M. Cloitre. Slip and flow in pastes of soft particles: Direct observation and rheology. *J. Rheol.*, 48(6):1295–1320, November 2004.
- [25] J. R. Seth, M. Cloitre, and R. T. Bonnecaze. Influence of short-range forces on wall-slip in microgel pastes. *Journal of Rheology (1978-present)*, 52(5):1241–1268, September 2008.
- [26] V. Mansard, L. Bocquet, and A. Colin. Boundary conditions for soft glassy flows: slippage and surface fluidization. *Soft Matter*, 10(36):6984–6989, August 2014.
- [27] T. Divoux, C. Barentin, and S. Manneville. Stress overshoot in a simple yield stress fluid: An extensive study combining rheology and velocimetry. *Soft Matter*, 7(19):9335, 2011.
- [28] P.-G. de Gennes, F. Brochard-Wyart, and D. Quéré. *Gouttes, bulles, perles et ondes*. Belin, Paris, 2005.

- [29] E. Jerison, Y. Xu, L. Wilen, and E. Dufresne. Deformation of an Elastic Substrate by a Three-Phase Contact Line. *Phys. Rev. Lett.*, 106(18):186103, 2011.
- [30] E. Guyon, J.-P. Hulin, and L. Petit. *Hydrodynamique physique*. EDP Sciences - CNRS Editions, Les Ulis - Paris, 2001.
- [31] N. Le Grand-Piteira. *Ruissellement avec effets de mouillage : Gouttes et méandres sur un plan incliné*. Thèse de Doctorat, Université Paris-Diderot - Paris VII, June 2006.
- [32] A.-L. Biance, C. Clanet, and D. Quéré. First steps in the spreading of a liquid droplet. *Phys. Rev. E*, 69(1), January 2004.
- [33] A. Eddi, K. G. Winkels, and J. H. Snoeijer. Short time dynamics of viscous drop spreading. *Phys. Fluids*, 25(1):013102, 2013.
- [34] J. Philippi. *Impact de goutte sur une surface solide*. Thèse de Doctorat, Université Pierre et Marie Curie - Paris VI, September 2015.
- [35] H. Lastakowski. *Impacts de gouttes sur coussins d'air : surfaces super-hydrophobes, chaudes ou mobiles*. Thèse de Doctorat, Université Claude Bernard - Lyon I, 2013.
- [36] C. Vernay, L. Ramos, and C. Ligoure. Free radially expanding liquid sheet in air: time- and space-resolved measurement of the thickness field. *J. Fluid Mech.*, 764:428–444, 2015.
- [37] L.-H. Luu and Y. Forterre. Drop impact of yield-stress fluids. *J. Fluid Mech.*, 632:301–327, 2009.
- [38] R. Rioboo, C. Tropea, and M. Marengo. Outcomes from a drop impact on solid surfaces. *Atomization Sprays*, 11(2):12, 2001.
- [39] L.-h. Luu. *Impact de gouttes de fluides à seuil : rhéologie, splash et cratères*. PhD thesis, Aix Marseille I, February 2011.
- [40] K. M. Case and W. C. Parkinson. Damping of surface waves in an incompressible liquid. *J. Fluid Mech.*, 2(02):172–184, March 1957.
- [41] F. Behroozi, B. Lambert, and B. Buhrow. Direct measurement of the attenuation of capillary waves by laser interferometry: Noncontact determination of viscosity. *Appl. Phys. Lett.*, 78(16):2399–2401, April 2001.
- [42] L. Kramer. Theory of Light Scattering from Fluctuations of Membranes and Monolayers. *J. Chem. Phys.*, 55(5):2097–2105, September 1971.
- [43] D. Langevin. Light-scattering study of monolayer viscoelasticity. *J. Colloid Interface Sci.*, 80(2):412–425, 1981.
- [44] A. Tay, C. Thibierge, D. Fournier, C. Fretigny, F. Lequeux, C. Monteux, J. P. Roger, and L. Talini. Probing thermal waves on the free surface of various media: Surface fluctuation specular reflection spectroscopy. *Rev. Sci. Instrum.*, 79(10):103107–103107–7, 2008.

- [45] B. Pottier, G. Ducouret, C. Frétygny, F. Lequeux, and L. Talini. High bandwidth linear viscoelastic properties of complex fluids from the measurement of their free surface fluctuations. *Soft Matter*, 7(17):7843, 2011.
- [46] S. Mora, T. Phou, J.-M. Fromental, L. Pismen, and Y. Pomeau. Capillarity Driven Instability of a Soft Solid. *Phys. Rev. Lett.*, 105(21):214301, November 2010.
- [47] R. G. Lerner and G. L. Trigg, editors. *Encyclopedia of Physics*. Wiley-VCH, Weinheim, 3rd edition, October 2005.
- [48] J.-P. Pérez. *Mécanique : Fondements et applications - Exercices et problèmes résolus*. Dunod, Paris, March 2001.
- [49] J. F. Joanny and P. G. de Gennes. A model for contact angle hysteresis. *J. Chem. Phys.*, 81(1):552–562, July 1984.
- [50] Y. Pomeau and J. Vannimenus. Contact angle on heterogeneous surfaces: Weak heterogeneities. *J. Colloid Interface Sci.*, 104(2):477–488, 1985.
- [51] J.-F. Joanny. *Le mouillage: quelques problèmes statiques et dynamiques*. Doctorat d'état, France, 1985.
- [52] J.-M. Di Meglio. Contact Angle Hysteresis and Interacting Surface Defects. *EPL*, 17(7):607, 1992.
- [53] C. W. Extrand and Y. Kumagai. An Experimental Study of Contact Angle Hysteresis. *J. Colloid Interface Sci.*, 191(2):378–383, 1997.
- [54] S. Moulinet. *Rugosité et dynamique d'une ligne de contact sur un substrat désordonné*. phdthesis, Université Paris-Diderot - Paris VII, July 2003.
- [55] S. Ramos and A. Tanguy. Pinning-depinning of the contact line on nanorough surfaces. *Eur. Phys. J. E*, 19(4):433–440, April 2006.
- [56] M. Reyssat and D. Quéré. Contact Angle Hysteresis Generated by Strong Dilute Defects. *J. Phys. Chem. B*, 113(12):3906–3909, March 2009.
- [57] M. Delmas, M. Monthieux, and T. Ondarçuhu. Contact Angle Hysteresis at the Nanometer Scale. *Phys. Rev. Lett.*, 106(13):136102, March 2011.
- [58] J. Crassous and E. Charlaix. Contact Angle Hysteresis on a Heterogeneous Surface: Solution in the Limit of a Weakly Distorted Contact Line. *EPL*, 28(6):415, 1994.
- [59] A. Marmur. Contact Angle Hysteresis on Heterogeneous Smooth Surfaces. *J. Colloid Interface Sci.*, 168(1):40–46, November 1994.
- [60] U. Öpik. Contact-Angle Hysteresis Caused by a Random Distribution of Weak Heterogeneities on a Solid Surface. *Journal of Colloid and Interface Science*, 223(2):143–166, March 2000.

- [61] G. Whyman, E. Bormashenko, and T. Stein. The rigorous derivation of Young, Cassie–Baxter and Wenzel equations and the analysis of the contact angle hysteresis phenomenon. *Chemical Physics Letters*, 450(4–6):355–359, January 2008.
- [62] L. Gao and T. J. McCarthy. How Wenzel and Cassie Were Wrong. *Langmuir*, 23(7):3762–3765, March 2007.
- [63] H. Y. Erbil. The debate on the dependence of apparent contact angles on drop contact area or three-phase contact line: A review. *Surface Science Reports*, 69(4):325–365, 2014.
- [64] R. J. Good and M. N. Koo. The effect of drop size on contact angle. *Journal of Colloid and Interface Science*, 71(2):283–292, September 1979.
- [65] J. Gaydos and A. W. Neumann. The dependence of contact angles on drop size and line tension. *J. Colloid Interface Sci.*, 120(1):76–86, November 1987.
- [66] J. Drelich and J. D. Miller. Modification of the Cassie equation. *Langmuir*, 9(2):619–621, 1993.
- [67] A. Amirfazli and A. W. Neumann. Status of the three-phase line tension: a review. *Advances in Colloid and Interface Science*, 110(3):121–141, 2004.
- [68] J. H. Weijs, A. Marchand, B. Andreotti, D. Lohse, and J. H. Snoeijer. Origin of line tension for a Lennard-Jones nanodroplet. *Physics of Fluids (1994-present)*, 23(2):022001, February 2011.
- [69] D. S. Fisher. Collective transport in random media: from superconductors to earthquakes. *Physics Reports*, 301(1–3):113–150, 1998.
- [70] J. Lin, E. Lerner, A. Rosso, and M. Wyart. Scaling description of the yielding transition in soft amorphous solids at zero temperature. *PNAS*, 111(40):14382–14387, October 2014.
- [71] R. D. Deegan, O. Bakajin, T. F. Dupont, G. Huber, S. R. Nagel, and T. A. Witten. Capillary flow as the cause of ring stains from dried liquid drops. *Nature*, 389(6653):827–829, October 1997.
- [72] D. Sikorski, H. Tabuteau, and J. R. de Bruyn. Motion and shape of bubbles rising through a yield-stress fluid. *Journal of Non-Newtonian Fluid Mechanics*, 159(1–3):10–16, 2009.
- [73] J. Eggers. Nonlinear dynamics and breakup of free-surface flows. *Rev. Mod. Phys.*, 69(3):865–930, 1997.
- [74] M. Tjahjadi, H. A. Stone, and J. M. Ottino. Satellite and subsatellite formation in capillary breakup. *J. Fluid Mech.*, 243:297–317, October 1992.
- [75] J. Eggers and T. F. Dupont. Drop formation in a one-dimensional approximation of the Navier–Stokes equation. *Journal of Fluid Mechanics*, 262:205–221, October 1994.

- [76] J. R. Lister and H. A. Stone. Capillary breakup of a viscous thread surrounded by another viscous fluid. *Physics of Fluids (1994-present)*, 10(11):2758–2764, November 1998.
- [77] S. L. Anna and G. H. McKinley. Elasto-capillary thinning and breakup of model elastic liquids. *J. Rheol.*, 45(1):115, 2001.
- [78] G. H. McKinley. Visco-Elasto-Capillary Thinning and Break-Up of Complex Fluids. Technical report, Hatsopoulos Microfluidics Laboratory - MIT, June 2005.
- [79] G. H. McKinley and T. Sridhar. Filament-Stretching Rheometry of Complex Fluids. *Annu. Rev. Fluid Mech.*, 34(1):375–415, 2002.
- [80] A. Bach, H. K. Rasmussen, and O. Hassager. Extensional viscosity for polymer melts measured in the filament stretching rheometer. *Journal of Rheology (1978-present)*, 47(2):429–441, March 2003.
- [81] P. Coussot and F. Gaulard. Gravity flow instability of viscoplastic materials: The ketchup drip. *Phys. Rev. E*, 72(3):031409, September 2005.
- [82] N. J. Balmforth, N. Dubash, and A. C. Slim. Extensional dynamics of viscoplastic filaments: II. Drips and bridges. *J. Non-Newtonian Fluid Mech.*, 165(19–20):1147–1160, October 2010.
- [83] N. J. Balmforth, N. Dubash, and A. C. Slim. Extensional dynamics of viscoplastic filaments: I. Long-wave approximation and the Rayleigh instability. *J. Non-Newtonian Fluid Mech.*, 165(19–20):1139–1146, October 2010.
- [84] G. German and V. Bertola. Formation of viscoplastic drops by capillary breakup. *Phys. Fluids*, 22(3):033101, 2010.
- [85] J. Seiwert. *Entraînements visqueux*. phdthesis, Ecole Polytechnique X, September 2010.
- [86] M. Maillard. *Étalements de fluides à seuil*. phdthesis, Université Paris-Est, September 2015.
- [87] M. Maillard, J. Boujlel, and P. Coussot. Solid-Solid Transition in Landau-Levich Flow with Soft-Jammed Systems. *Phys. Rev. Lett.*, 112(6):068304, 2014.
- [88] L. Baudonnet, J.-L. Grossiord, and F. Rodriguez. Effect of Dispersion Stirring Speed on the Particle Size Distribution and Rheological Properties of Three Carbomers. *J. Dispersion Sci. Technol.*, 25(2):183–192, 2004.
- [89] P. Lidon, L. Villa, and S. Manneville. Power-law creep and residual stresses in a carbopol microgel. *arXiv*, May 2016. arXiv: 1605.02083.
- [90] B. Géraud, L. Jørgensen, C. Ybert, H. Delanoë-Ayari, and C. Barentin. Structural and cooperative length scales in polymer gels. *Submitted to EPJE*, 2016.

- [91] M. Doi. *Introduction to Polymer Physics*. Clarendon Press, November 1995.
- [92] J. Goyon, A. Colin, G. Ovarlez, A. Ajdari, and L. Bocquet. Spatial cooperativity in soft glassy flows. *Nature*, 454(7200):84–87, 2008.
- [93] A. Mgharbel, H. Delanoë-Ayari, and J.-P. Rieu. Measuring accurately liquid and tissue surface tension with a compression plate tensiometer. *HFSP Journal*, 3(3):213–221, 2009.
- [94] T. V. Stirbat, S. Tlili, T. Houver, J.-P. Rieu, C. Barentin, and H. Delanoë-Ayari. Multicellular aggregates: a model system for tissue rheology. *Eur. Phys. J. E*, 36(8):1–14, August 2013.
- [95] M. A. Fortes. Axisymmetric liquid bridges between parallel plates. *J. Colloid Interface Sci.*, 88(2):338–352, 1982.
- [96] H. Zuidema and G. Waters. Ring Method for Determination of Interfacial Tension. *Ind. Eng. Chem. Anal. Ed.*, 13(5):312–313, 1941.
- [97] P. M. Heertjes, E. C. de Smet, and W. C. Witvoet. The determination of interfacial tensions with the Wilhelmy plate method. *Chem. Eng. Sci.*, 26(9):1479–1480, September 1971.
- [98] H. H. Girault, D. J. Schiffrin, and B. D. V. Smith. Drop image processing for surface and interfacial tension measurements. *J. Electroanal. Chem.*, 137(2):207–217, 1982.
- [99] S. D. Christian, A. R. Slagle, E. E. Tucker, and J. F. Scamehorn. Inverted Vertical Pull Surface Tension Method. *Langmuir*, 14(11):3126–3128, 1998.
- [100] J. W. Krumpfer and T. J. McCarthy. Contact angle hysteresis: a different view and a trivial recipe for low hysteresis hydrophobic surfaces. *Faraday Discuss.*, 146:103, 2010.
- [101] P. Coussot. Saffman-Taylor instability in yield-stress fluids. *J. Fluid Mech.*, 380:363–376, 1999.
- [102] J. Engmann, C. Servais, and A. S. Burbidge. Squeeze flow theory and applications to rheometry: A review. *J. Non-Newtonian Fluid Mech.*, 132(1–3):1–27, 2005.
- [103] T. G. Mason, J. Bibette, and D. A. Weitz. Yielding and Flow of Monodisperse Emulsions. *J. Colloid Interface Sci.*, 179(2):439–448, 1996.
- [104] L. Jørgensen, M. L. Merrer, H. Delanoë-Ayari, and C. Barentin. Yield stress and elasticity influence on surface tension measurements. *Soft Matter*, 11(25):5111–5121, June 2015.
- [105] A. J. Franck. Understanding Instrument Inertia Corrections in Oscillation. Technical report, TA Instruments, 2005.
- [106] R. Brown. `fitcircle.m`, 2007.
- [107] A. F. Stalder, G. Kulik, D. Sage, L. Barbieri, and P. Hoffmann. A snake-based approach to accurate determination of both contact points and contact angles. *Colloids and Surfaces A: Physicochemical and Engineering Aspects*, 286(1–3):92–103, September 2006.

- [108] R. N. Wenzel. Resistance of solid surfaces to wetting by water. *Ind. Eng. Chem.*, 28(8):988–994, 1936.
- [109] S. Das, A. Marchand, B. Andreotti, and J. H. Snoeijer. Elastic deformation due to tangential capillary forces. *Physics of Fluids*, 23(7):072006, 2011.
- [110] F. Restagno, C. Poulard, C. Cohen, L. Vagharchakian, and L. Léger. Contact Angle and Contact Angle Hysteresis Measurements Using the Capillary Bridge Technique. *Langmuir*, 25(18):11188–11196, September 2009.

# Figure Credits

1.8	Partial wetting. . . . .	33
	(b) Photo by Deglr6328 on Wikipedia ( <a href="https://en.wikipedia.org/wiki/File:Video_contact_angle.gif">https://en.wikipedia.org/wiki/File:Video_contact_angle.gif</a> ) Licence CC BY-SA . . .	33
1.9	Photo by Rather Anonymous on Flickr ( <a href="https://www.flickr.com/photos/79262083@N00/34743746">https://www.flickr.com/photos/79262083@N00/34743746</a> ) Licence CC BY-NC . . . . .	33
1.10	Photo by Jimmy Roussel on FEMTO - Cours de mécanique des fluides ( <a href="http://femto-physique.fr/mecanique_des_fluides/mecaflu_C4.php">http://femto-physique.fr/mecanique_des_fluides/mecaflu_C4.php</a> ) Licence CC BY-NC . . . . .	34
1.11	Photo of an experiment by Baudouin Géraud . . . . .	34
1.12	Photo by Omagatron on Wikimedia Commons ( <a href="https://commons.wikimedia.org/wiki/File:Water_splashes_001.jpg">https://commons.wikimedia.org/wiki/File:Water_splashes_001.jpg</a> ) Licence CC BY-SA . . .	36
1.13	Figure taken from Luu's PhD thesis ( <a href="http://www.theses.fr/2011AIX10023">http://www.theses.fr/2011AIX10023</a> ), with permission from the author. ©L.H. Luu . . . . .	37
1.14	Photo by Anders Sandberg on Flickr ( <a href="https://www.flickr.com/photos/arenamontanus/1358639911">https://www.flickr.com/photos/arenamontanus/1358639911</a> ) Licence CC BY (modification: cropped) . .	38
1.15	Photo by Ivicabrlc on Wikimedia Commons ( <a href="https://commons.wikimedia.org/wiki/File:Spider_web_with_morning_dew.jpg">https://commons.wikimedia.org/wiki/File:Spider_web_with_morning_dew.jpg</a> ) Licence CC BY-SA . . . . .	39
2.5	Figure from Manglik <i>et al.</i> , Dynamic and equilibrium surface tension of aqueous surfactant and polymeric solutions, Exp. Thermal Fluid Science, 2001. ©Elsevier	50